

**NOVEL LOW-COST, HIGH-PERFORMANCE RESISTIVE
SENSOR INTERFACE TECHNOLOGIES FOR PPB-LEVEL
CHEMICAL DETECTION IN SMART-CITIES**

by

Matthieu Couriol

A dissertation submitted to the faculty of
The University of Utah
in partial fulfillment of the requirements for the degree of

Doctor of Philosophy

Department of Electrical and Computer Engineering

The University of Utah

December 2023

Copyright © Matthieu Couriol 2023

All Rights Reserved

The University of Utah Graduate School

STATEMENT OF DISSERTATION APPROVAL

The dissertation of

Mathieu Couriol

has been approved by the following supervisory committee members:

<u>Pierre-Emmanuel Julien Marc Gaillardon</u> ,	Chair(s)	<u>10/09/2023</u>	
			Date Approved
<u>Remy Cellier</u> ,	Member	<u> </u>	
			Date Approved
<u>Seyed Armin Tajalli</u> ,	Member	<u>10/07/2023</u>	
			Date Approved
<u>Ross M. Walker</u> ,	Member	<u> </u>	
			Date Approved
<u>Darrin J. Young</u> ,	Member	<u>10/09/2023</u>	
			Date Approved

by Florian Solzbacher , Chair/Dean of

the Department/College/School of Electrical and Computer Engineering

and by Darryl P. Butt , Dean of The Graduate School.

ABSTRACT

According to the World Health Organization (WHO), almost all of the global population (99%) is exposed to poor air quality with high levels of pollution that exceed WHO standards. Air pollution is defined as "a contamination of the indoor or outdoor environment by any chemical, physical or biological agent that modifies the natural characteristics of the atmosphere." It is therefore mandatory to quantify air quality based on its complex chemical composition. However, monitoring the chemical composition of ambient air in urban environments is challenging. Urban air is subject to fast temperature and humidity variations, quick exposures of chemicals, background noise, and block-by-block pollution sources. Therefore, some cities are now increasing the density and capabilities of their air quality monitoring stations with larger chemical portfolios, better selectivity, and lower detection levels to better estimate and address chemical exposures.

Emerging technologies such as state-of-the-art chemiresistive organic sensors and more particularly nanofiber-based technologies are now able to detect chemical traces in the air down to low Part Per Billion (*ppb*) levels with high selectivity. These low Size, Weight and Power (SWaP) sensors are suitable for high density environmental sensor networks in urban environments.

In this context, this Ph.D. dissertation aims to enhance smart cities (a technologically modern urban area that uses different types of electronic methods and sensors to collect specific data) capabilities with a novel integrated circuit capable of interfacing nanofiber-based sensors to any smart cities monitoring station. More specifically, I designed and validated a wide range resistive sensor interface to monitor highly resistive ($50 + G\Omega$) sensors such as nanofibers. First, I introduce a fully-integrated resistance-to-digital interface with on-board autonomous calibration and range selection to improve dynamic range and measurement error. I then introduce a low-power design to interface a high number of channels on a small die area of 5 mm^2 . Furthermore, I demonstrate that the sampling frequency of relaxation oscillators is limited by parasitics from the sensors, and

I propose a parasitic mitigation circuitry to significantly improve the sampling frequency and also eliminate spurious commutations due to noise. In all, the novel contribution of this dissertation is a small form factor and low-cost system that can monitor 12 chemicals in parallel thanks to our new resistance to digital interface and emerging nanofiber sensors.

La vérité de demain se nourrit de l'erreur d'hier.

Antoine de Saint-Exupéry - *Pilote de guerre*

CONTENTS

ABSTRACT	iii
LIST OF TABLES	viii
LIST OF ABBREVIATIONS	ix
ACKNOWLEDGEMENTS	xiv
CHAPTERS	
1. INTRODUCTION	1
1.1 Motivation for Air Quality Monitoring	3
1.2 Current Electronic Nose and Smart Cities Limitations	6
1.3 Improving AirU Nodes to ChemAirU with Emerging Sensor Technologies and In-House Sensor Interface	7
1.4 Dissertation Contributions	8
1.5 Organization of the Dissertation	11
2. IMPROVING ENVIRONMENTAL SENSOR NETWORK FOR AIR QUALITY MONITORING	20
2.1 Pollution Monitoring Networks Background	20
2.2 Nanofiber-Based Sensors: An Emerging Organic Sensor Technology for Smart- Cities Applications	25
2.3 Chapter Summary	32
3. A LOW-POWER AND LOW-COST WIDE-RANGE RESISTANCE TO DIGITAL INTERFACE FOR NANOFIBER SENSORS	42
3.1 Sensor Interfaces Background	42
3.2 A Fully-Integrated Wide Range Resistance to Digital Interface	45
3.3 A Nanofiber-Optimized Resistance to Digital Interface	57
3.4 Novel Techniques for Improved Sampling Frequency	63
3.5 Chapter Summary	69
4. CHEMAIRU: A LOW LEVEL OF DETECTION CHEMICAL MONITORING NODE	106
4.1 Background on ChemAirU's Building Blocks	106
4.2 A Low SWaP, Low-Cost, Multi-Chemical Monitoring System	108
4.3 Proof of Concept: A Low Level of Detection Platform for Monitoring Acetic Acid in Gases	117
4.4 Chapter Summary	123
5. CONCLUSION	140

5.1 Summary of Contributions	142
5.2 Future Work	144
APPENDICES	
A. FABRICATED DEVICES	146
B. CHEMAIRU RECORDING DATASETS	160
REFERENCES	169

LIST OF TABLES

1.1	Recommendation AQG levels and interim targets.	14
1.2	Composition of dry unpolluted air by volume.	15
1.3	Air quality guidelines for nitrogen dioxide (NO_2), sulfur dioxide and carbon monoxide (for short averaging times) that remain valid.	16
2.1	Comparision of large-scale (40+ nodes deployed) and long-term (several months of data) ESNs.	34
3.1	Comparison of state-of-the-art high-dynamic range resistance interfaces.	71
3.2	Required performances of the ASIC.	72
3.3	Operational amplifier's transistor sizing.	73
3.4	Main characteristics of the OA.	74
3.5	Configurable ranges of the ASIC.	75
3.6	Comparison to state of the art resistance to frequency interfaces.	76
3.7	Transistor size of the power-consumption optimized OA.	77
3.8	Main characteristics of the power-consumption optimized OA.	78
4.1	Sensor configuration of the fabricated device.	125
4.2	Percentage identification results when exposing the sensor suite to chemicals pairs (row versus columns).	126

LIST OF ABBREVIATIONS

10 μm or smaller Particulate Matter	PM_{10}
1 μm or smaller Particulate Matter	PM_1
2.5 μm or smaller Particulate Matter	$PM_{2.5}$
Acetic Acid	AA
Advanced RISC Machines	ARM
Air Pollution	AP
Air Quality Guidelines	AQG
Air Quality Index	AQI
Air Quality Monitoring	AQM
Air Quality Systems	AQS
Air Quality and You [University of Utah]	<i>AQ&U</i>
Alternating Current	AC
Analog-to-Digital Converter	ADC
Application Specific Integrated Circuit	ASIC
Array of Things	AoT
Berkeley Environmental Air-quality & CO_2 Network	BEACO ₂ N
Capacitance	C
Capacitive Micromachined Ultrasonic Transducers	CMUT
Carbon Dioxide	CO_2
Carbon Monoxide	CO
Carbon-NanoTube	CNT
Center for Disease Control and Prevention	CDC
Central Processing Unit	CPU

ChloroFluoroCarbons	CFC
Complementary Metal-Oxide-Semiconductor	CMOS
Defense Advanced Research Projects Agency	DARPA
Defence Science and Technology Laboratory	DSTL
Design Rule Check	DRC
DiMethylTryptamine	DMT
Digital Controller	DC
Doctor of Philosophy	Ph.D.
Environmental Protection Agency	EPA
Environmental Sensing Network	ESN
Federal Equivalent Method	FEM
Federal Reference Method	FRM
Field Programmable Gate Array	FPGA
Figure of Merit	FoM
Frequency to Digital	F2D
Gain	G
Gain BandWidth product	GBW
Global Positioning System	GPS
Global Warming	GW
GreenHouse Gases	GHG
Ground	GND
HyperText Transfer Protocol	HTTP
Input/Output	I/O
Inter-IC Sound	I2S
Inter-Integrated Circuit	I2C
Internet of Things	IoT
Layout Versus Schematic	LVS

Light-Emitting Diode	LED
Limit Of Detection	LOD
London Air Quality Network	LAQN
Low Drop-Out	LDO
Machine Learning	ML
Massachusetts Institute of Technology Lincoln Laboratory	MIT LL
Mass Flow Controller	MFC
Message Queue Telemetry Transport	MQTT
Metal Oxide Semiconductor	MOS
Micro-ElectroMechanical Systems	MEMS
MicroController Unit	MCU
Multi-Project Wafer	MPW
National Ambient Air Quality Standards	NAAQS
Nitrogen Oxide	NO
Nitrogen Oxides	NO_x
Nitrogen Dioxide	NO_2
Nitrous Oxide	N_2O
Operational Amplifier	OA
Optical Partical Counter	OPC
Over The Air	OTA
Ozone	O_3
Parasitics EXtraction	PEX
Part-per-billion	ppb
Part-per-million	ppm
Part-per-trillion	ppt
Particulate Matters	PMs
Phosgene	CG

Photonic Crystal	PhC
PolyTetraFluoroEthylene	PTFE
Power Rail	VDD
Printed Circuit Board	PCB
Programmable Capacitor Integrator	PCI
Programmable Gain Amplifier	PGA
Programmable Logic Device	PLD
Pulse Width Modulation	PWM
Quad Flat No-lead	QFN
Quartz Crystal Micro-balance	QCM
Real-Time Clock	RTC
Real-time Affordable Multi-Pollutant	RAMP
Relative Humidity	RH
Resistance	R
Resitance to Frequency	R2F
Sample Per Minute	SPM
Sarin	GB
Secure Digital	SD
Serial Peripheral Interface	SPI
Signal over Noise Ratio	SNR
Size Weight and Power	SWaP
Source Measurement Unit	SMU
Sulfur Dioxide	SO_2
Sulfur Mustard	HD
Surface Acoustic Wave	SAW
Sustainable Development Goals	SDG
TriNitroToluene	TNT

Triple Quadrupole Mass Spectrometer	TQMS
U.S. Army Combat Capabilities Development Command Chemical Biological Center	DEVCOM CBC
United Stated (of America)	US
United Stated of America	USA
Universal Asynchronous Reciever Transmitter	UART
Volatile Organic Compound	VOC
Water Vapors	WV
World Health Organization	WHO

ACKNOWLEDGEMENTS

I would like to express my sincere gratitude to my PI Pierre-Emmanuel Gaillardon for his invaluable guidance, encouragement, and support throughout this journey. His expertise and mentorship have been instrumental in shaping the direction of this research and helping me navigate the various challenges along the way. PE, I think we made a really good team, I'm proud of the work done.

I would also like to thank my committee members, Pr. R. Cellier, Pr. A. Tajalli, Pr. R. Walker and Pr. D. Young. for their insightful feedback and constructive criticism that greatly improved the quality of this manuscript. Their input and suggestions were invaluable in helping me develop my ideas and arguments.

I would like to acknowledge the support of my family who have also provided invaluable support and encouragement. Their love and support have been critical in helping me achieve my goals. Maman, Papa, Clément, Alexis, merci beaucoup, j'aurai pas survécu sans vous. Je vous aime fort. Et Cookie, à jamais à mes côtés.

I will also mention all my friends who have always picked up the phone when needed. It is true being isolated across the ocean during a world pandemic is tough, very tough, and you've all participated in making this possible. I cannot thank you enough. (I will also never forget that I had to go through this because you all encouraged me to! Please, never again.)

I want to extend a special thank you to my girlfriend Erin for her unwavering love, support, and encouragement throughout this (endless) academic journey. Her understanding, patience, and belief in me have been an infinite source of motivation and inspiration. I think we can now think about visiting Paris when they are not on strike.

Lastly, I would like to thank all the individuals who have contributed to this project in various ways, including research participants, collaborators, and colleagues. Their contributions have been critical in making this project a success. Dr. R. Reitstetter, I think you have been one of the most important collaborator in this project, I truely learnt a lot

from you, I think we did great together, thank you. Bob, Omar, you can finally take a break from all my purchase requests. Corinne, thank you so much for all the support and feedbacks. Thanks to the amazing people at Blackrock, soccer games really helped me stay sane. Thanks to all my friends at Apple, I'm really glad we're still in contact. Wish you the best Big D, Big S. Patsy, Ed, Tom, Orel, Primo, Ganesh, Allen, Henry (my capt.), Marjo, Owen and so many more!

Thank you all for your invaluable contributions, and for making this journey both challenging and rewarding.

PS: PE, I hope I'll get a graduation sword with a "MATTHIEUUUU," cheers Marcus.

CHAPTER 1

INTRODUCTION

The World Health Organization (WHO) designated climate change as the greatest challenge of the 21st century [1]. Climate change endangers human health and development by threatening access to clean air, safe water, food, and shelter. The effects of global warming are immediate and already causing damage in the form of extreme weather events (more frequent and powerful tsunamis, tornados, droughts, monsoons) and increased health conditions due to pollution, poor water, and poor food quality. According to WHO, 24% of global deaths are linked to the environment and more than 4 million humans die from exposure to particulate matter each year [2]. Experts anticipate more climate-related deaths in the near future, postulating that at least 250,000 additional people will die annually between 2030-2050 as a result of climate change.

Many nations are beginning to take action to combat the climate crisis, for instance, by participating in the Paris climate agreement [3]. The measures outlined in the Paris climate agreement have the potential to reduce air pollution enough to save millions of lives. These steps would not only save lives, but also promote economic growth by supporting a healthier population. Altogether, the reduction of pollutants in air is a challenge that can save millions of lives, billions of dollars, and thousands of animal species worldwide [4]. A WHO report [5] laid out important first steps to responding to climate change: understand the health risks from current and future climate hazards; evaluate which populations are most vulnerable to the health impacts of climate change; identify gaps in current policies and programs aimed at reducing the risks; and identify and prioritize effective adaptation interventions to respond. For this reason, WHO has developed tools and Air Quality Indexes (AQI) and Air Quality Guidelines (AQG) [6] to serve as quantitative health-based recommendations for air quality. Air quality exceeding guideline levels causes serious risk to public health.

WHO AQG use a very small subset of chemicals to define their air quality thresholds including Particulate Matter ($PM_{2.5}$ and PM_{10}), nitrogen dioxide (NO_2), sulfur dioxide (SO_2), ozone (O_3), carbon monoxide (CO). However, these previously defined pollutants are only a subset of the chemicals present in the environment. To date, scientists have identified almost 3,000 distinct anthropogenic air pollutants, primarily organic compounds (including organometals). Combustion sources, particularly motor vehicles, release around 500 different compounds. However, only about 200 of these pollutants have undergone comprehensive impact investigations [7]. Ignoring other chemicals can result in incomplete and at times inaccurate estimations of health risks [8].

Over the past decade, the escalating concern over air quality has led to a heightened focus on air quality monitoring [9–13]. Applications ranging from safeguarding human health indoors and outdoors [9, 10, 14, 15] to addressing industrial emissions [16–19], gas leaks, and safety concerns, demonstrate the need for accurate and comprehensive air quality assessments. To address these applications there has been an effort to develop sophisticated and cost-effective monitoring solutions [12, 20].

Major cities play a decisive role in reducing air pollution and are now deploying large and dense networks of sensors [21, 22] to monitor air quality in urban environments. These Environmental Sensor Networks (ESN) [12] are used to assess air quality and compare to WHO AQG. However, they lack the necessary hardware to monitor chemicals comprehensively and report the intricate chemical composition of the air, which significantly contributes to air pollution.

This Ph.D. dissertation explores the requirements for monitoring a large portfolio of chemicals at a large scale and discusses the current limitations in state of the art ESNs. We present and discuss the emerging technology of organic chemiresistive sensors such as nanofiber sensors and discuss their applications for air composition monitoring. This Ph.D. dissertation presents a novel low-cost, low-power, nanofiber-optimized resistance-to-digital Application Specific Integrated Circuit (ASIC) for interfacing a large array of sensors. Finally, the dissertation puts forth a small form-factor, ESN-compatible system for monitoring 12 different chemicals in real time using the fabricated ASIC. This system serves as a proof of concept for smart cities applications to enhance ESN with chemical monitoring capabilities.

1.1 Motivation for Air Quality Monitoring

Air Quality Monitoring (AQM) is necessary to understand Air Pollution (AP) [9–12]. AP has direct short-term and long-term impact on global warming and human health. AQM helps authorities and populations understand the source of pollution and is the first crucial step in the process of reducing the human carbon footprint.

1.1.1 Effects of Air Pollution on Human Society

The main contributors of AP are GreenHouse Gases (GHGs) such as carbon dioxide (CO_2), nitrous oxide (N_2O), and chlorofluorocarbons (CFCs). CHGs are the main contributors of Global Warming (GW) and change Earth's climate by increasing the opacity of air, thus absorbing more longwave radiation emitted by the Earth's surface and ultimately increasing Earth's temperature [23]. The increased average earth temperature induced by GW is responsible for rising sea levels, water restrictions, and heat waves. GW is also amplified by the water vapour positive feedback effect [24]. The effect of Water Vapor (WV) on GW is usually bounded since WP has a short residence time of a few weeks in the atmosphere, then depleted rapidly through condensation and precipitation. The upper bound is the absolute humidity of air of 100% which increases as temperature rises per Clausius–Clapeyron equation [24]. As the temperature rises, the absolute humidity of the air tends to increase, amplifying the greenhouse effect of the atmosphere.

Recent work [25] has reported the economical burden of climate change to not only be defined by long-term temperature increase but also short-term health and economical impact. Currently, WHO states that more than 99% of the world's population is exposed to poor air quality and that AP is responsible for 6.7 million premature deaths each year [2]. By meeting the Paris climate agreement, 74,000 lives could be saved across the European region by 2030, and 250,000 lives could be saved worldwide. Reduction of short-lived pollutants (black carbon, methane) could save nearly 2.5 million lives yearly [26]. For this reason, AQI, AQG (shown in Table 1.1, [6]) and Sustainable Development Goals (SDG) have been defined to reduce the impact of air pollution on human society. In particular, the Paris climate agreement aims at limiting fossil fuel use and GHG to limit temperature increase to $1.5^{\circ}C$.

Additionally, recent work [3] established that the health benefits greatly exceed the

policy cost of achieving the 1.5°C temperature increase target. Improving air quality is therefore a win-win action as it would reduce immediate exposures to pollutants, reduce illness, and prevent GW on the short and long run which would also economically benefit society.

1.1.2 Urban Centers: Empowering Change

A significant portion of the essential measures aimed at lowering carbon emissions, enhancing health, and building resilience take place at the subnational level. Local authorities hold full or partial responsibility for services like energy supply, transportation, water, sanitation, and healthcare. Cities, in particular, play a vital role in spearheading efforts related to climate and health initiatives [1]. Public authorities are aware of their impact on air pollution and are equipping cities with ESN to monitor AQ at different locations. London, for example, is financing the [London Air Quality Network \(LAQN\)](#) hosted on the LondonAir website, a city scale network of hundreds of nodes used to monitor air quality in London, with data made available to the public [27]. The network constantly monitors levels of *PMs*, *NO₂*, and *O₃* across the city and allows for great advances in research to:

1. Test new equipment to measure pollution, for example, new ways to measure particle pollution
2. Examine the effects of changes in pollution sources to see if policies to clean air are efficient
3. Study differences in exposure to air pollution and health, for example, study the differences between the pollution that citizens breathe on their bikes versus on the bus.

LAQN has reported that they now have much more information about the health effect of air pollution and now estimate that the quality of air in London reduces life expectancy by about a year. In the United States of America (USA), the Environmental Protection Agency (EPA) provides a nation-wide map for monitoring air quality, also available to the public [28]. The EPA provides a national Air Quality System (AQS) data repository for public access to assess the extent of air pollution, evaluate the effectiveness of emissions control strategies, and provide information on air quality trends.

1.1.3 Monitoring Air Quality in Urban Environments: Addressing the Challenges

Although public authorities are making efforts to understand the sources of pollution and how to reduce emissions, monitoring pollution in urban environments is still subject to multiple challenges:

1. **Multiple sources of pollution:** Ambient air is a complex composition of chemicals. Unpolluted air contains 11 major chemicals reported in Table 1.2, [29]. Polluted air contains six major pollutants, and other extra pollutants not included in the AQI and AQG. This, in itself, introduces limitations on the ability of authorities to accurately judge the pollution level of ambient air. Since cities host a very wide range of industries, there is a need for monitoring the chemical composition of the air in order to estimate where the sources of different types of pollution come from.
2. **Complex meteorology:** Pollution and ambient air are subject to local weather conditions, and sensor placement is crucial for proper monitoring of local AQ. Plus, environmental changes due to human activity (airflows, exhausts, temperature difference created by cars for example) create background noise that needs to be accounted for during acquisition and data processing.
3. **Variability over small distances:** Microscale environmental variations, such as wind direction, temperature/humidity inversions, and local airflow influence the dispersion of pollutants. These environmental conditions occur on small spatial scales and create pockets of stagnant air which trap pollutants in specific areas, causing variations in air quality.
4. **Cost and logistical challenges:** ESNs are usually composed of hundreds of nodes in order to properly map air quality and increase spatiotemporal resolution, but this comes at a cost. Each node requires access to a power source and data access points (WiFi, BlueTooth, Radio, LoRaWAN, etc.) to stream data which increases the complexity of the network.
5. **Data analysis and interpretation:** With the aforementioned complex chemical behavior of ambient air and the number of ESN nodes in urban environment, interpreting data is challenging.

Currently deployed ESN address most of these challenges using calibration techniques, machine learning, and reference units. These post-processing algorithms allow for envi-

ronmental variations removal, network-wide node to node recalibration, and real-time AQ mapping. However, ESN still lack the modularity of chemical monitoring to be adopted world-wide.

1.2 Current Electronic Nose and Smart Cities Limitations

1.2.1 Chemical of Interest Limitations

The Center for Disease Control and Prevention (CDC) reports six pollutants listed as criteria air pollutants by EPA [30]. These six pollutants are regulated with scientifically-determined guidelines and thresholds: carbon monoxide (CO), lead, nitrogen oxides (NO_x), ground-level ozone (O_3), particle pollution (PM), and sulfur oxides (SO_x). Nine other air pollutants are reported but do not appear in CDC criteria, these pollutants are: acrolein, asbestos, benzene, carbon disulfide, creosote, fuel oils/kerosene, Polycyclic Aromatic Hydrocarbons, Synthetic Vitreous Fibers, and Total Petroleum Hydrocarbons.

Most of these aformentioned pollutants are not even monitored in most ESN. For example, LAQN can only monitor and model four chemicals that are known to have an effect on health. SO_2 is not of interest because of modeling limitations. Moreover, some of the pollution created by cars reacts with O_3 and causes it to change into other chemicals [31], incorrectly suggesting that O_3 is lower in the middle of London and close to busy roads.

There is a critical gap in data availability and in the ability to properly monitor chemicals. Indeed, as we discussed, due to chemical cross-reactivity, the limited amount of monitored chemicals, and the lack of better models, current air quality monitoring is limited to a small number of criteria chemicals. The lack of data including a larger portfolio of chemicals makes it challenging to develop newer models and deploy better guidelines to monitor pollution levels, thus limiting the capacity of authorities to employ efficient measures against air pollution.

1.2.2 Throughput Data Limitations

The recent deployment of large-scale ESNs has greatly improved the spatiotemporal resolution of measured signals. Indeed, previously used chemical monitoring air quality equipments such as TQMS [32] suffered from poor sampling rate (1 Sample Per Minute (SPM)), low network density (< 5 pieces of equipment per city), and high power con-

sumption (kiloWatts). Even in the process of cutting power consumption and chemical portfolio, recent ESN limit their data acquisition to a couple SPM, and report averaged data to the public every 15 min. As reported by the WHO AQG, the health risks of chemical exposures are related to the exposure length in time and concentration in part-per-million (*ppm*) (Table 1.3, [33]). Therefore, it is necessary to enhance ESN capabilities to include short exposures of high concentrations of chemicals into account before estimating the AQI.

Secondly, as reported by LAQN, ESNs tend to report smaller values of ozone in the city center. Some of the pollution created by cars reacts with ozone (O_3) and causes it to change into other chemicals resulting in an underestimation of the amount of pollution in the air and a need to increase the complexity of data calibration.

To properly accomodate for chemical spikes and quick variations, we propose to use an array of chemical sensors, interfaced at a high data sampling rate (> 100 Hz) for estimating the presence of chemicals in the air. Coupled with an on-board machine learning algorithm trained to estimate chemical populations based on the individual responses of each sensor, and equipped with humidity, temperature sensing and background removal, we believe our current ESN could greatly improve the quality of AQ measurements [34]. The increase in data sampling will allow measurements of short exposures of high concentrations of chemicals, and the large array of chemical sensors can help estimate a broader chemical portfolio, which is crucial for defining new Figure Of Merits (FOMs) and designing new models for air quality.

1.3 Improving AirU Nodes to ChemAirU with Emerging Sensor Technologies and In-House Sensor Interface

1.3.1 Current Status of the AirU Network

The current AirU, shown in Figure 1.1, is the second generation of the AirU pollution monitor and measures $PM_{2.5}$, PM_{10} , CO , NO_x and environmental variations (temperature and humidity). Each node features a GPS module for localisation and a WiFi-enabled MCU based on the Espressif System ESP32 MCU. Each sensor is interfaced to the MCU using Universal Asynchronous Reciever Transmpter (UART) or Inter-Integrated Circuit (I2C) industrial serial communication buses. The MCU gathers data from the sensors and

transfers via the **Message Queue Telemetry Transport** (MQTT) protocol to a server hosted by the CADE lab at the University of Utah (air.eng.utah.edu), within the Department of Computer Science. The average power consumption of AirU nodes for a 60-second sampling period (1 SPM) is about 187 milli-Watts (mW). Figure 1.2 shows the current deployment of AirU in the valley of Salt Lake City [35]. Currently, 85 AirU nodes are deployed in the valley of Salt Lake City and 275 are deployed internationally as shown in Figure 1.3.

1.3.2 Network and Nodes Requirements

The AQ&U (Air Quality and You [University of Utah]) team provides the following guidances for the AirU network and nodes:

- AirU must at least report the major polutants listed by EPA: PM, CO, NO_x , O_3 .
- The power consumption of AirU must be kept as low as possible for battery-powered applications and remote sensing. The baseline power consumption of AirU is 187mW.
- AirU must be able to report at least one datapoint per 10 seconds, or 6 SPM. Current maximum speed is 30 SPM.
- AirU must be kept as small as possible for easy integration within other systems, for example, deployment in vehicles, indoor laboratories, or environmental chambers. The current AirU system is about 4 in \times 4 in \times 2 in.
- AirU must be kept low cost, allowing the scalability of the network. The current version of AirU costs less than \$200.

In that regard, we propose to use AirU as our test-bed platform. We will leverage the AirU network and propose a system that can easily be interfaced with AirU to extend its capabilities. The next section will discuss the **contributions** of this Ph.D. dissertation to achieve this goal.

1.4 Dissertation Contributions

This dissertation work explores the feasibility of monitoring the complex chemical composition of ambient air in an urban environment with high spatiotemporal resolution and designs a proof-of-concept system showcasing preliminary results for such a task. In this work, we design a novel ASIC to interface state-of-the-art chemical sensors based on emerging nanofiber technologies.

The resulting system is composed of the emerging nanofiber sensor technology and the novel ASIC that interfaces the sensors. This dissertation discusses different circuitries to improve the performance of wide-range resistance-to-digital (R2D) interfaces. The design and performance of the novel ASIC is shown as is the integration of the ASIC with the sensors in a chemical monitoring system, which serves as a proof of concept for smart cities applications.

In particular, we highlight the main contributions of this work in the following list:

- **Three novel wide-range resistance to digital interfaces:** The nanofiber sensor technology employed in this work requires the use of high-performance interfaces that can be integrated seamlessly in already deployed ESN nodes. We designed three wide-range resistance-to-digital interfaces optimized for improved **dynamic range, noise and measurement error (1)**, reduced **power and cost (2)** and finally higher **sampling frequency (3)**. The novel circuitries involved for each interface contribute to improving wide-range resistance performance and their integration within commercially available systems. Each of the three novel circuitries address the aforementioned limitations and validate the improvements as shown through device manufacturing and testing. The three interface designs have respectively shown the following improvements compared to state of the art:

1. **Dynamic range and measurement error (Section 3.2):** The interface is based on a relaxation oscillator that features an analog front-end with two input ports for directly interfacing the resistive sensor and an integrated digital controller. The analog front end converts the resistivity of the sensor to a frequency, and the digital controller handles the frequency measurement, autonomous calibration, range adjustment, and data transmission. With the implementation of a Programmable Gain Amplifier (PGA) and a Programmable Capacitor Integrator (PCI), the system shows a $5\times$ improvement in sampling frequency compared to state of the art. The circuit also has a calibration mode to improve measurement error by $3\times$ against state of the art interfaces. Dynamic range is also increased by 20 dB against state of the art wide range resistor interfaces.
2. **Power and cost (Section 3.3):** This resistance to frequency converter is based on the same topology as the first design but at reduced bandwidth, and therefore,

reduced power and area. We used lower power operational amplifiers to reduce the overall area and power consumption of the oscillator. Comparing this new version to the previous oscillator, we have observed a significant 4x improvement in area and a substantial 3.4x reduction in power consumption. Additionally, we have incorporated drivers for shielding the high-impedance sensor lines, resulting in a 20% reduction in noise compared to the unshielded configuration. Finally, the ASIC now supports 12 resistance to frequency channels, enabling simultaneous recording of 12 nanofibers.

- 3. **Sampling frequency (Section 3.4):** We demonstrate that the sampling frequency of relaxation oscillators with highly resistive sensors is limited by the parasitics of the interfaced sensors. We designed a novel low trade-off parasitics mitigation circuitry to improve sampling frequency when interfacing highly resistive sensors using resistance-to-frequency converters. This nanofiber-optimized version of the ASIC features 12-channels to interface up to 12 nanofibers on a single 5 mm^2 die with a power consumption as low as 2.65 mW per channel, including on-board voltage references, a digital controller, and shielding driving I/Os to avoid external charge injections. This novel architecture decorrelates the limitations in sampling frequency from the sensor's characteristics; instead, sampling rate is limited by the ASIC itself (power, area). The proposed analog front-end offers better sampling frequency ($+30\times$) and area/cost (-13%) compared to regular relaxation oscillators. The power consumption trade-off is minimal ($+60\mu\text{A}$ per analog front-end or $+14\%$). The maximum sampling frequency is 100 Hz at $50\text{ G}\Omega$. The circuit has been validated at post-pex and the layout featuring 12 interfaces on a minimal 5 mm^2 die is shown with a total power consumption of 2.65 mW or 0.94 mA per sensor.

- **A low SWaP 12 chemical proof-of-concept wearable ESN node for smart cities (Section 4.2):** We present ChemAirU, a proof-of-concept system based on AirU that co-integrates our system with 12 chemical sensors to AirU. This proposed miniature chemical monitoring system interfaces with AirU's ESP32 MCU via UART. The fabricated ChemAirU enables real-time monitoring of 12 chemicals, achieving low Size, Weight, and Power (SWaP) due to optimized Light-Emitting Diodes (LED)

biasing and sensor interfaces. Each chemical channel draws about 4.3 mW without the MCU, making it a suitable reference for future ESN node additions. With a compact equivalent size of approximately 2 in² and a height of 0.5 in, the system weighs around 15 grams, including the two PCBs for sensors and LEDs. The total cost, including sensors, is roughly \$25 per channel. ChemAirU showcases seamless integration of chemical monitoring into existing ESNs through UART, enabling easy and cost-effective data reporting. This innovative system offers efficient and affordable real-time chemical monitoring for smart cities, enriching environmental insights.

- **A low level of detection platform for monitoring acetic acid in gases (Section 4.3):**

We demonstrate the nanofiber-based system as a proof of concept with the detection of acetic acid. Early detection of cystic fibrosis in humans and wine faults during fermentation both require very sensitive and portable electronic noses. We propose a 2 in² wireless chemical monitoring electronic system based on the nanofiber sensors and our interface to detect acetic acid in gases. We perform PCA analysis on the sensors' responses and train a classifier algorithm which demonstrates accurate cystic fibrosis detection in human breath. Our work demonstrates a limit of detection using nanofiber sensors down to 40 ppb. We also include sensor responses for different humidities to accommodate for the presence of water vapor in human breath and wine. Additionally, this work has successfully shown the detection of acetic acid within 1 s of a 5 s exposure at 40 ppb.

1.5 Organization of the Dissertation

This dissertation investigates the possibility of monitoring a wide variety of chemicals in real time in an urban environment. It is organized in four main chapters, not including the introduction. The manuscript is organized as follows:

- In **Chapter 2**, we discuss the roles of pollutants monitoring networks. First, we provide a brief review of state-of-the-art monitoring networks and their limitations. We then discuss the current state of the AirU network, which serves as a platform for establishing the capability of our system to monitor chemicals in the air. We discuss the hardware implementations of AirU nodes and network and its role in a smart city application. We also discuss the new emerging nanofiber-based sensors

with a review of existing sensor technologies. We identify the pros and cons of each individual sensor technology and determine which technology is best suited for improving smart cities chemical monitoring, based on the aforementioned performance requirements. **This chapter defines the design specifications for seamless integration of the chemical monitoring platform onto exisiting ESN nodes.**

- In **Chapter 3**, we discuss the designs of the ASICs that were fabricated during this dissertation to interface nanofiber sensors. We first review state-of-the-art high resistance interfaces, identify their limitations for smart cities applications, and discuss their capabilities in interfacing nanofiber sensors. Secondly, three different resistance-to-digital interfaces were designed to be optimized for dynamic range, power and cost, and sampling frequency. **The first circuit explores how to improve state of the art in terms of measurement error and dynamic range. The second circuit explores the cost and power optimization for highly resistive sensors. The final study explores new ways of improving sampling frequency.** We use a wide range resistance-to-digital interface based on a relaxation oscillator topology for each design. We discuss the design of the top-level system which includes the analog front-end and the digital controller. This system explores the use of programmable gain amplifier (PGA) and programmable integration capacitors (PIC) for increasing dynamic range of the oscillator at a reduced power consumption. We discuss the post-silicon results and capabilities of the ASIC to interface nanofibers as well as the use of calibration mode using external reference resistance to improve measurement error across the whole range. Finally, we study the limitations in sampling frequency and explore solutions to improve the sampling frequency of relaxation oscillators when the sensor technology limits sampling frequency. We discuss post-pex results and provide comparision to the previous ASIC and prior state-of-the-art work.
- In **Chapter 4**, we introduce the miniaturized version of ChemAirU, **the evolution of initial AirU nodes with chemical detection capabilities in a low SWaP package.** We first discuss the design and mechanical assembly of the system. We showcase the performance of the fabricated device and provide chemical identification capabilities results. We finally conclude this chapter with a **proof of concept for quantitative detection of acetic acid in human breath** using classifier algorithm that succesfully

shows low false positive rate using the combination of our electronics and sensors.

- **Chapter 5** concludes this dissertation and summarizes the contributions of this work, and also discusses future directions.

Air Quality Guidelines

Table 1.1: Recommendation AQG levels and interim targets.

Pollutants	Averaging Time	Interim target				AQG levels
		1	2	3	4	
<i>PM</i> _{2.5} ($\mu\text{g}/\text{m}^3$)	Annual	35	25	15	10	5
<i>PM</i> ₁₀ ($\mu\text{g}/\text{m}^3$)	Annual	70	50	30	20	15
<i>O</i> ₃ ($\mu\text{g}/\text{m}^3$)	Peak Season	100	70	-	-	60
<i>NO</i> ₂ ($\mu\text{g}/\text{m}^3$)	Annual	40	30	20	-	10
<i>SO</i> ₂ ($\mu\text{g}/\text{m}^3$)	24 hours	125	50	-	-	40
<i>CO</i> ₂ (mg/m^3)	24 hours	7	-	-	-	4

Table 1.2: Composition of dry unpolluted air by volume.

Gas	Part
Nitrogen	78.084 %
Oxygen	20.946 %
Argon	0.934 %
Carbon Dioxide	360 <i>ppm</i>
Neon	18.18 <i>ppm</i>
Helium	5.24 <i>ppm</i>
Methane	1.6 <i>ppm</i>
Krypton	1.14 <i>ppm</i>
Hydrogen	0.5 <i>ppm</i>
Nitrous Oxide	0.3 <i>ppm</i>
Xenon	0.087 <i>ppm</i>

Table 1.3: Air quality guidelines for nitrogen dioxide (NO_2), sulfur dioxide and carbon monoxide (for short averaging times) that remain valid.

Pollutant	Averaging time	Part
NO_2 ($\mu\text{g}/\text{m}^3$)	1 hour	200
SO_2 ($\mu\text{g}/\text{m}^3$)	10 minute	500
CO_2 (mg/m^3)	8 hours	10
	1 hour	35
	15 minutes	100

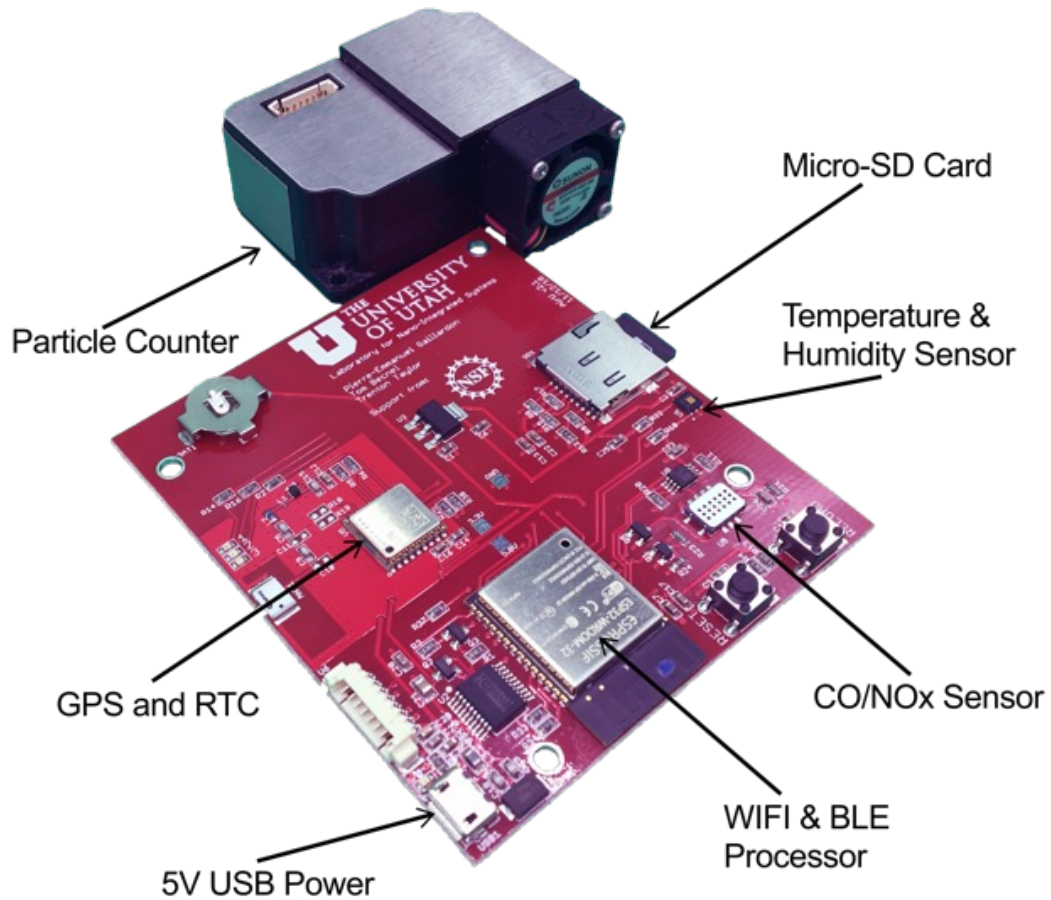


Figure 1.1: Picture of the electronics of the current AirU node, with annotations.

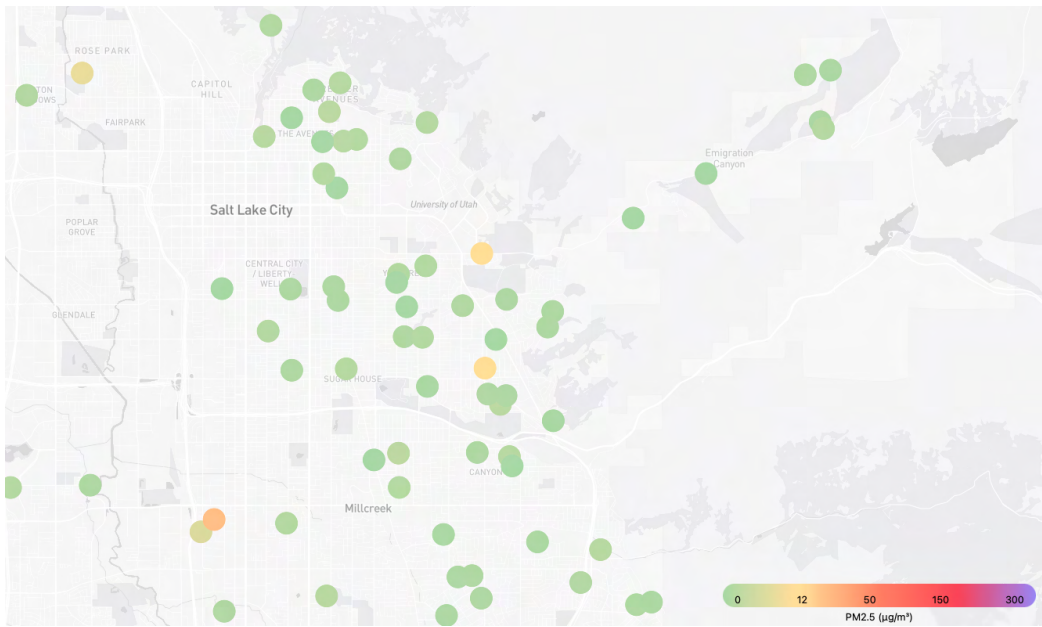


Figure 1.2: Current deployment status of the AirU ESN as of Monday June 12th 2023 across the valley of Salt Lake City. Each dot represents an AirU node from Figure 1.1.

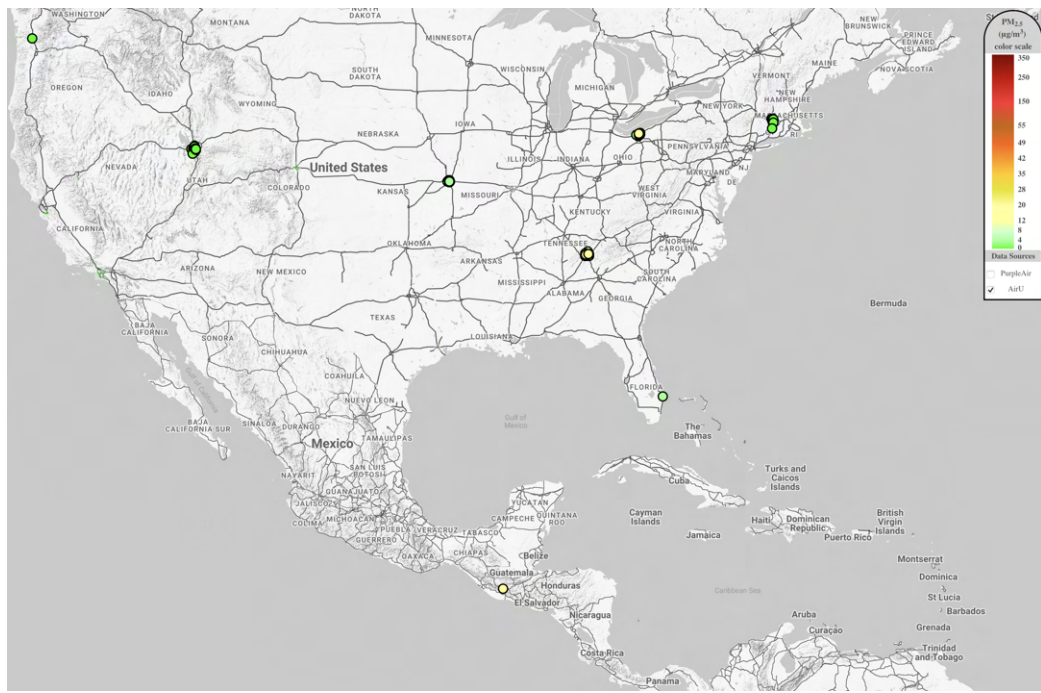


Figure 1.3: Current deployment status of the AirU ESN as of Monday June 12th 2023 across North America. Each dot represents an AirU node from Figure 1.1.

CHAPTER 2

IMPROVING ENVIRONMENTAL SENSOR NETWORK FOR AIR QUALITY MONITORING

Since the goal of this dissertation is to improve ESN with chemical monitoring capabilities, this chapter discusses the challenges involved in upgrading current ESNs to detect a wider range of chemicals. We discuss the design and limitations of currently deployed low-cost ESN and identify the requirements to improve their chemical sensing capabilities. A key consideration is the ease of integration; additional circuitry required for chemical monitoring should seamlessly integrate with any already deployed systems. Additionally, we provide a quick review of sensor technology and focus on emerging nanofiber technology, which is of particular interest as part of our Defense Advanced Research Projects Agency (DARPA) SIGMA+ program, which aims at expanding the SIGMA program capability to radioactive, chemical, biological, and explosive threats. We propose a set of performance specifications to design the sensor interface which, combined with the system integration specifications, set the requirements for a chemiresistive sensor interface for ppb-level chemical detection in smart-city applications.

2.1 Pollution Monitoring Networks Background

Air pollution monitoring is the measurement of the amount and types of certain pollutants in the outdoor or indoor air. Different monitoring approaches are used to monitor air quality based on the application needs and the monitoring devices need to match the performance criteria (accuracy, reliability, etc). Several measurement methods exist with the most common ones being [36]:

- **Reference systems** are used to ensure compliance with the National Ambient Air Quality Standards (NAAQS [37]) and are designated as either Federal Reference Method (FRM) or Federal Equivalent Method (FEM) monitors [38,39]. These monitors must adhere to strict operating and performance criteria specified in the U.S.

Code of Federal Regulations [38]. They yield precise and reliable data of exceptional quality that can be used to calibrate ESNs. However, they lack the spatio-temporal resolution of ESNs [40, 41] and cannot create a detailed map of air quality as shown in Figure 2.1.

- **Remote sensing** is a stand-off method for measuring pollutants from a distance. It can be used for detecting PM, gases, and some VOCs and can be deployed with aircrafts, satellite-based platforms, or at ground-based sites.
- **ESN** are a class of monitoring systems that offer the best cost, portability, and ease of use. They can measure the main air pollutants including PM and gases. They offer a cloud-based platform for data streaming but lack the accuracy, lifetime, and reliability of reference systems due to the use of low-cost sensors, local environmental variations, and limitations in calibration techniques.

Since the scope of this Ph.D. work is to improve ESNs with chemical detection capabilities, we review the existing ESNs to highlight the general lack of chemical detection capabilities, and we also review the AirU nodes hardware to determine the design requirements needed to add chemical monitoring to the platform.

2.1.1 Current Approaches and Networks for Affordable Pollution Monitoring

Several large-scale (40+ nodes) and long-term (several months of data collection) ESNs have been recently deployed to provide fine spatial and temporal resolutions for $PM_{2.5}$, O_3 , NO_2 , SO_2 , and CO. These networks monitor the main pollutants of interests reported by WHO and EPA at low cost and low power with smart interpolation between individual measurements and data calibration at the network level against FEMs. This Ph.D. research introduces a solution to improve the functionality of existing ESN nodes through chemical monitoring. To achieve this, we conduct a thorough comparison of the technology employed in currently deployed large-scale and long-term ESN nodes. This analysis enables us to establish the specific requirements for our system, ensuring seamless integration with any ESN without necessitating a complete redesign or the addition of extra electronics (e.g., stronger power supply, larger battery, more powerful MCU, or added FPGAs).

Zimmerman et al. introduce the Real-time Affordable Multi-Pollutant (RAMP) [42, 43] monitors co-developed by the Center for Atmospheric Particle Studies at Carnegie Mellon

University and SenSevere, a private company in Pittsburgh, PA [44]. This system is capable of interfacing up to five gas sensors (SO_2/NO , CO , CO_2 , O_3/VOC , NO_2) with temperature and RH. The data are monitored using custom electronics and streamed every 15 s through cellular. RAMP monitors feature B4 sensors from Alphasens that are interfaced with Alphasens ISB resistance to voltage converters. The main board features ADCs to digitize the voltages from the sensors and connect to the MCU for cellular streaming using industry standard serial communication links. The whole system draws about 100 mW on average for a total package volume of about 100 in^3 .

Shusterman *et al.* describe the Berkeley Environmental Air-quality & CO₂ Network (BEACO₂N) ESN node, a shoe-sized device containing CO_2 , CO , NO_2 , NO , O_3 , and aerosol sensors [45, 46]. Additionally, each node can monitor temperature, RH, and atmospheric pressure. Data are collected every five seconds to the on-board Raspberry Pi featuring the MCU and on-board SD card storage. Data are stored locally on the SD card and streamed out through ethernet or WiFi to the Berkeley servers when available. The device draws about a watt of power and has built-in UART/SPI/I2C/I2S communication links.

Catlett *et al.* present the Array of Things (AoT) project which provides several approaches to hosting sensors. AoT can either interface very simple sensors through direct serial links such as UART or more sophisticated ones that need signal conditionning using an internal module called MetSense [47]. The size limitation of new sensors that need shielding is limited to three inches in diameter and one inch in height. The AoT is based on the open-source Waggle project [48] with multiple MCUs and a node controller featuring a simple Amlogic quad-core ARM Cortex A5 single-board computer (ODROID C1+). The payload processor uses a Linux-based single-board computer (ODROID XU4) based on the Samsung Exynos5422 CPU; the waggle manager uses the Atmel ATMEGA32U4-MU; and the total system is powered with a single 50 watt power supply.

Chen *et al.* partnered with Edimax Inc. and Realtek Inc. to develop Airbox, a monitoring device based on the Realtek Ameba development board [49]. Airbox contains a PMS5003 particulate sensor coupled with am HTS221 temperature and humidity sensor. The device allows for very low cost monitoring of particulate matter and the cortex M3 features all the industrial serial connection for communicating with external sensors.

Daepp *et al.* introduce an end-to-end platform for environmental sensing in cities

with CO , NO_2 , SO_2 , O_3 , $PM_{2.5}$ and temperature/humidity monitoring [50]. The ultra-low power NRF9160 micro-controller interfaces digital and analog sensors. Just like previous work, the micro-controller includes industrial serial links for directly interfacing a suite of sensors. The maximum power consumption during sampling and data transmission is limited by the PM sensor pulling 250mW of power during **sampling with wireless transfer** also in that range.

Table 2.1 summarizes **the comparision** of ESN networks and showcases the technical limitations about enhancing these ESN with an external chemical monitoring system. While BEACO₂N and AoT systems can draw watts of power, most systems are limited to the hundreds of milliwatts. In order to provide a chemical monitoring system that easily integrates within all existing ESN, its power requirements must be non-significant compared to the most power efficient ESN. This allows for seamless integration of the chemical monitoring system with the existing power rails and does not impact battery life/solar power modules. Additionally, the limitation in size comes from the AoT system, which sets a maximum size of the chemical monitoring system of three inches in diameter. Finally, we have identified that large-scale ESNs feature a central MCU for software integration of the sensors and wireless data transmission. The MCUs used in ESN have industrial standard serial capabilities for interfacing commercial off-the-shelf sensors such as some Alphasens sensors which communicate through I2C. For this reason, we will design our chemical sensor interface with UART serial links for simple and seamless integration of the chemical interface within an existing ESN.

2.1.2 AirU: A Pollutant Monitoring Network of Environmental Sensors

We have briefly discussed the hardware implementation of the different largely deployed ESN in the previous sub-section. We identified design requirements for seamless integration of chemical monitoring capabilities within currently deployed ESN. In this sub-section, we discuss the hardware implementation of AirU, a largely deployed ESN in the valley of Salt Lake City. Figure 2.2 shows the current deployment status of AirU in the valley of Salt Lake City, where more than 80 nodes currently record air quality in Salt Lake City area with 270 more nodes worldwide.

The AirU pollution monitor was originally designed and fabricated in 2018. It has been

upgraded multiple times with newer hardware and software and the latest characteristics of the AirU nodes, shown in Figure 1.1 and listed below:

- **Hardware Considerations:**
 - A particulate matter (PM) sensor measures the concentration and quantity of dust particles in the air**
 - 1. PM Sensor: AirU uses a Plantower PMS3003 optical particle counter (OPC) to measure airborne particulate matter concentrations (PM_1 , $PM_{2.5}$, and PM_{10}).
 - 2. NO_2 and CO: SGX SensorTech MiCS-4514, which contains two fully independent MOS sensing elements for oxidizing and reducing gasses.
 - 3. Temperature and Humidity Sensor: The device employs a Texas Instruments HDC1080 sensor, which communicates via an I2C interface and is calibrated to correct manufacturer variability.
 - 4. GPS Module: A Quectel L70 GPS Module is incorporated into the AirU to enable mobile data acquisition and provide elevation data for atmospheric inversion climate evaluation.
 - 5. Micro-SD Card: The AirU includes a 4 GB micro-SD card that can store roughly one year of data. Data packets are also stored on the micro-SD card in case of disconnection from the host WiFi network.
 - 6. Onboard USB-UART Bridge: AirU includes an onboard USB-to-UART bridge for flashing and debugging without requiring external circuitry. This improvement is aimed at enhancing debug and deployment times and providing an all-inclusive platform for citizen scientists to write their own firmware and re-program the AirU to suit their specific needs. This feature empowers users to customize the device according to their needs.
- Network Considerations:
 - 1. Data Transfer: Locally gathered data is transferred from the AirU device to a server at the University of Utah via the **MQTT protocol**.
 - 2. Data Storage: The data is stored in an InfluxDB database, and users can easily retrieve data using the InfluxDB tool or web interfaces.
 - 3. OTA Firmware Updates: The platform supports over-the-air (OTA) firmware updates, enabling new features and sensor corrections to be applied to the system without direct user interaction.
- Offline Data Upload Procedure:

1. GPS and RTC Enable Offline Data Collection: The GPS module, real-time clock (RTC), and micro-SD card allow the AirU to collect pollution data while offline and upload data when an internet connection is re-established.
 2. Data Uploading: Data packets are uploaded via HTTP to the server, and the server handles duplicate data points, maintaining a data point for every minute the AirU is powered on.
- Power, Cost, and Storage Characteristics:
 1. Power Consumption: The AirU draws 540 mW when fully active and 10 mW in a light-sleep state. The average power consumption for a 60-second period is 187 mW.
 2. Cost: The AirU costs less than \$200, including hardware, fabrication, assembly, and housing.
 3. Data Storage: With a 4 GB micro-SD card and data packets less than 250 bytes, the AirU can potentially store over 30 years of data at a standard 60-second sampling period.

Using AirU as a testbed for the proposed chemical monitoring system is a strategic approach to validate and demonstrate its capabilities. Integrating chemical monitoring into AirU will first expand the network's ability to provide valuable data on pollutants and chemical gases, enhancing its environmental monitoring capabilities. Second, the seamless integration of the proposed chemical monitoring system into the AirU network is critical for ensuring its effectiveness and compatibility with other ESNs. Demonstrating smooth integration with AirU will serve as evidence of its adaptability to similar ESNs, showcasing its potential for broader deployment and adoption. The next section 2.2 discusses the sensor technologies and supports the choice of sensor for enhancing ESN with chemical monitoring capabilities.

2.2 Nanofiber-Based Sensors: An Emerging Organic Sensor Technology for Smart-Cities Applications

This section explores existing and promising gas sensor technologies for ESN. We provide a review of state-of-the-art sensor technologies and explore the capabilities of nanofiber sensors to monitor chemicals in the air. After discussing the technology behind nanofiber

sensors, we propose a list of design specifications to properly interface nanofiber-based sensors.

2.2.1 Chemical Sensors Background

Current ESN nodes use a combination of MOS (Metal Oxide Semiconductor) sensors and optical sensors to detect volatile organic compounds (VOCs) and PM. These sensors are widely commercialized and used but suffer from poor selectivity and power consumption. For this reason, we provide a short review of sensor technologies [15, 51–54] to compare state-of-the-art sensing technologies to nanofiber-based sensors.

1. CNT gas sensors

- These sensors are based on the use of the Carbon Nanotubes (CNT) as a sensing material with properties depending on their shape. They come with enhanced sensitivity, low detection limit and fast response but can be expensive to manufacture [55].

2. Acoustic gas sensors

- Quartz Crystal Micro-balance (QCM) [56] gas sensors are still being researched and leverage the physics of piezoelectric crystal to measure mechanical deformation due to the deposition of chemical on the surface of the sensor. QCM appear to lack sensitivity and have a high limit of detection (both in the *ppm* range) compared to other types of sensors.
- Surface Acoustic Wave (SAW) gas sensors [57] were introduced decades ago. They detect environmental changes based on the properties of the surface wave and amplitude. They have low limits of detection, down to picograms, with high sensitivity and a short response time. They, however, operate at high temperatures and high frequency which can make them power hungry.
- Capacitive Micromachined Ultrasonic Transducers (CMUT) are an alternative to piezoelectric sensors. They provide a wide range of applications with a large catalog of detectable chemicals. They report high sensitivity and a low limit of detection [58] but can be challenging to interface, sometimes requiring biasing voltages up to 30 V [59]. Such high biasing voltages either require specific high-voltage process for the integrated circuit to interface them, or an external circuitry, at the expense of power consumption.

3. Optical gas sensors

- Fiber optic sensors [60] are great candidates for environmental monitoring since they can be used in an array with different sensing devices to differentiate various analytes. The sensing membrane is excited with light and corresponding changes in refracted light beams are measured to quantify the amount of vapors. They show high selectivity, sensitivity, and stability but suffer from their form factor, which is hard to scale down.
- Photonic Crystal (PhC) sensors are manufactured with an arrangement of dielectric materials with different refractive indexes. Using light exposure, the compounds are estimated by measuring the variation in the refractive indexes of the materials. PhC have a reported limit of detection in the *ppm* range [61].

4. Electrochemical gas sensors

- The MOS gas sensing mechanism is probably one of the most common gas sensors, and it was introduced decades ago when the intrinsic resistance of Cu_2O was found to be affected by the absorption of WV [62, 63]. MOS sensors are based on a combination of a sensing layer, electrodes, and a microheater and are great candidates for detecting VOC at *ppm* levels. They benefit from a low cost manufacturing process, precise measurement capabilities, high durability, and ease of use. However, their temperature operating range of 150 °C to 400 °C leads to high power consumption.
- Organic sensors, and more particularly nanofiber-based sensors, have proven high sensitivity to chemicals in the air with detection levels in the ppb range [64]. Their behavior is similar to a variable resistor whose value depends on the concentration of chemical traces. The nanofibers are self-assembled one-dimensional (line) *n*-type or *p*-type semiconductors [64]. The conductivity of the nanofiber depends on charge density. The chemicals influence the conductivity of the nanofiber by changing the electron density. In other words, the resistivity of the nanofibers is a function of the chemical population in the air. Nanofiber-based sensors come in a 2 mm² wire-bondable package and are a perfect solution for a low-cost and low-power chemical monitoring station. They benefit from high sensitivity, high selectivity, and short response time at

room temperature [65], but suffer from baseline drift when biased at a constant voltage.

Smart cities require a low-power, low-LOD, and low-cost sensing system for monitoring chemicals in an urban environment. For this reason, we propose to use nanofiber-based sensors for this application. Their low cost ($< \$10$), low LOD ($< ppb$), low power (estimated at few milliwatt per sensors), and small footprint ($< 1 \text{ mm}^2$) make them the perfect candidate for monitoring a suite of chemicals in real time.

2.2.2 Nanofiber-Based Sensor Technology

Chemical vapor sensing using nanofibers involves surface absorption of gas analyte. Indeed, nanofibers are dropped on a surface to create a self-assembled organic layer. Prior work demonstrates the surface-supported self-assembly using glass, SiO_2 , or carbon film [66]. The block molecules used for self-assembly allow for very high selectivity and can be designed for sensing very specific gases of interest [66], such as explosives (DNT/TNT) [67], alkanes [68], or methamphetamine [69] down to the low part-per-trillions (ppt) levels [67]. Vaporsens, owned by Gentex, manufactures such sensors with a portfolio of up to 100+ chemicals of interest [70].

Figure 2.3 is a macrophotography of the nanofiber sensor. The sensor is composed of two gold pads, located on the left and right side of the image that are deposited on a base block of quartz. The gold pads are interdigitated and serve as connections for the sensor. In the remainder of this dissertation, these connection pads will be referred as *Sensor-* and *Sensor+* for the electrical schematics. The self-assembled layer of nanofiber compound is the circular shape that can be seen in Figure 2.4 and is deposited on top of the interdigitated gold fingers. The nanofiber fills the gaps between the interdigitated fingers and acts as a conductive material between *Sensor-* and *Sensor+* as shown on the cross-section diagram of the sensor in Figure 2.5. When chemical vapors come in contact with the nanofiber, the molecules change the behavior of the nanofiber by accepting or donating an electron, thus changing the conductive behavior of the material. The change of conductivity can be measured across *Sensor-* and *Sensor+*, and the behavior of the sensor is chemiresistive [66, 71–73]. The mobility of the charge carriers of the organic material can be increased with photonic energy in order to increase the conductivity of the sensor. LEDs

can be used to illuminate the sensors to reduce their intrinsic impedance. Thanks to the aforementioned self-assembly of block molecules, only the molecules capable of bonding with the molecular chain of the nanofiber can interact with the material, thus showcasing great sensitivity at very low level of detection (*ppb*) within seconds [67]. Sub-*ppb* level of detection with a variation in conductivity of the sensor of 0.3% has been successfully demonstrated at room temperature, thus eliminating the need for external heater [67]. Nanofibers outperform other sensing mechanisms concerning factors such as response and recovery time, power, selectivity, and sensitivity [71–73].

Nanofiber sensors are affordable (< \$10) and come in a small footprint of roughly 1 mm² that can be wirebonded onto a PCB, as shown in Figure 2.4. Thanks to the large portfolio of nanofibers available, the low cost, and small foot-print, it is possible to deploy a large array of distinct nanofibers. The different response of each individual sensor to chemicals creates a complex unique array signature response to each environmental exposure that can be analyzed to fully characterize the chemical composition of ambient air. Although the current state of research is limited to a simple understanding of the response of these sensors, deploying a large network of arrays of sensors is necessary for building a database of complex datasets, which is required for training machine learning algorithms capable of analyzing the array's response [74].

Although the main focus of this Ph.D. dissertation is to design a chemiresistive sensor interface, the following sections provide valuable information about the behavior of the sensors which sets the required monitoring parameters of the ASIC.

2.2.3 Model of the Nanofiber Sensors

2.2.3.1 The Ideal Nanofiber's Resistive Model

The sensor behaves like a variable resistor [66, 71–73, 75] as shown in Figure 2.5. Chemical vapors land on the porous surface of the fibers through molecular diffusion and surface absorption, resulting in a change in charge carrier density between *Sensor-* and *Sensor+* [67, 75]. The population of chemicals in the air can thus be estimated based on the sensor's resistance variations $\frac{\Delta R}{R_0}$ (in %), with R_0 being the baseline resistance of the sensor and $\Delta R = R - R_0$, the resistance variation from baseline. Therefore, the electrical equivalent model of the ideal sensor is a variable resistor R_{sen} with:

1. A baseline resistance value R_0 that varies with temperature, lighting conditions, and

voltage biasing.

2. A sensor response ΔR due to chemical exposure. ΔR depends on the absorption and diffusion of chemicals within the organic material.

This Ph.D. dissertation designs and fabricates a resistance-to-digital interface to monitor the sensor's intrinsic resistance for chemical detection. The interface's requirements are set by: the baseline resistance range of the sensors (R_{0-min} and R_{0-max}), the minimum ΔR response, the sensor's noise level, and the response time.

Our study of the baseline variations over a set of nanofibers under different biasing and environmental conditions has shown that the baseline of the sensors is very wide and variable. Some sensors have exhibited extremely large baseline values, as high as tens of gigaohms, while others have shown baseline resistance within the mega-ohm range. Additionally, the light conditions of the sensors and temperature highly impact the conductivity of the organic material and thus the baseline resistance of the sensor: we have seen a $40\times$ increase in baseline resistance of the sensor when reducing the photonic power (for battery life reasons), further supporting the need for a very wide range resistance interface for measuring the sensor's resistance. Although we have not experienced any baseline resistance of the sensors below $1\text{ M}\Omega$, the resistance-to-digital interface must be capable of interfacing sensors down to $100\text{ k}\Omega$ to account for process and temperature variation impacting the performance of the interface, and to provide headroom for further conductivity improvements in the sensor's manufacturing process.

The sensor's noise level was measured in an environmental chamber, at room temperature of 25°C in a zero-air (pure air gas) flow of 1 L min^{-1} using a B1500A silicon analyzer. Although noise performance has not been conducted on a large number and a wide selection of sensors, and measurements do not reflect a statistically optimized value, we have estimated the noise of the sensors to be below $100\text{ ppm}_{\text{RMS}}$ at 1 Hz , which corresponds to a standard variation of 0.01% from baseline. Additionally, the minimum sensor response measured under the same conditions was a $\frac{\Delta R}{R_0} = 0.7\%$ response. This value is the smallest experienced response from the sensors and can be used to derive the noise floor of the interface for precise signal detection.

The nanofiber sensors showed an impressive response time to low level of chemicals, consistently detecting chemicals within 1 second of exposure. Although the response time

is on the order of seconds, it is important to sample the sensor's response at a higher sampling rate, especially when monitoring a large array of sensors where the complex unique signature response of the array feeds a sorting algorithm to characterize ambient air. We propose to sample nanofibers at 100 Hz, which is 2 orders of magnitude higher than the response time, to generate a high temporal-resolution signature for each sensor.

2.2.3.2 The Impact of Parasitics on the Sensor's Interface

The inter-digitated gold fingers arrangement of the sensors allows for larger surface area which increases the chemical absorption of the sensor. The design also allows for reduced baseline resistance but increases the parasitic capacitance between the *Sensor-* and *Sensor+* pads. The parasitic capacitance C_{para} appears across the two pads and in parallel with the sensing resistance as shown in Figure 2.6. Figure 2.5 shows the main contributors in the parasitic capacitance. The two main contributors are the organic material deposited on top and in-between the gold fingers with the capacitance C_{fiber} , and the base material with the capacitance C_{quartz} . Both capacitances contribute to the parasitic capacitance $C_{para} = C_{fiber} + C_{quartz}$.

The parasitic capacitance C_{para} adds a frequency-dependant impedance in the sensor model which leads to the sensor's impedance $Z_{sen} = \frac{R_{sen}}{1+jR_{sen}C_{para}\cdot\omega}$. The sensor impedance is the expected R_{sen} at DC but rapidly drops as the sensor's voltage biasing varies in frequency. With typical values of $R_{sen} = 10\text{ G}\Omega$ and $C_{para} = 5\text{ pF}$, the impedance of the sensor varies by more than 4% of R_{sen} at 1 Hz. The parasitic impedance therefore greatly limits the ability of the measurement system to accurately capture the value of R_{sen} at high sampling rate. Commercial high-impedance measurement units often refer to C_{para} as a stray capacitor which increases the response time required to converge to the final resistance value [76].

The manufacturing process of the nanofiber imposes a value on C_{para} which makes the nanofibers challenging to interface at a combined high sampling rate and low measurement error. For this reason, we propose different sensor interfaces that target each of the following challenges. In the next chapter, Sections 3.2 and 3.3 study the performance of relaxation oscillators when interfacing ideal resistance at high measurement accuracy, low cost, and low power. We then present a novel parasitic capacitance mitigation circuit in

Section 3.4 that boosts the sampling rate of relaxation oscillators when interfacing high value resistances with parallel parasitic capacitance with low area and power trade-off.

2.3 Chapter Summary

In this chapter, we investigated the technology currently employed in largely-deployed ESNs. We have identified a set of specifications and requirements for enhancing these ESNs with chemical monitoring capabilities:

- Size constraint: The chemical monitoring system needs to be small in order to fit within the already existing ESN node's enclosure.
- Power constraint: The chemical monitoring system must have minimal additional power consumption compared to the baseline power usage of the ESN node. This allows for direct connections to the already existing power lines without impacting battery life.
- Number of channels: Urban air is composed of a multitude of chemicals and therefore, ESN must be able to monitor a large amount of chemicals to properly monitor the complex chemical composition.
- Serial line: The MCU used in ESN are compatible with serial lines, we propose to use UART for the chemical monitoring system for seamless integration with the MCU.

We also reviewed existing chemical sensor technologies, with deeper discussions about the emerging nanofiber-based sensors technology. We identified that low-cost nanofiber sensors allow for high-quality data acquisition but require a very wide-range resistance-to-digital interface. This novel resistance sensor's interface must be low-power for the aforementioned power constraint and must output the data through UART to be easily interfaced with already deployed ESN. Additionally, the integrated circuit we propose to design must carefully address the trade-off involved with accommodating a large number (12+) of sensors and with keeping the area small for low-cost ESNs.

For this reason, we propose to design and fabricate an ASIC to interface nanofiber-based sensors at low-power and low-cost. Figure 2.7 shows the top-level proposed system, the resistance of the sensor is monitored in real time by our interface and streamed to an MCU for signal processing. Chapter 3 discusses the ASIC design, we first review of state-of-the-art wide range resistance interfaces and identify prior work limitations. We propose

to improve wide-resistance interfaces with novel circuitries to interface nanofiber-sensors, with design specifications ruled by low-cost ESNs.

Table 2.1: Comparision of large-scale (40+ nodes deployed) and long-term (several months of data) ESNs.

Network	<i>No. of sensors</i>	<i>Sampling Rate</i>	<i>Peak Power Usage</i>	<i>Serial Links</i>	<i>Size</i>
RAMP [42–44]	7	15s	100mW	Unknown	> 100 ch ³
BEACO ₂ N [45, 46]	9	10s	Watts	UART/SPI/I2C	> 30 in ³
Array of Things [47]	20	30s	< 50Watts	UART/SPI/I2C/I2S	> 100 in ³
Airbox [49]	3	1min	500mW	UART/SPI/I2C	> 10 in ³
Eclipse [50]	8	5min	400mW	UART/SPI/I2C/I2S	> 20 in ³
AirU [77]	8	1min	500mW	UART/SPI/I2C	< 20 in ³

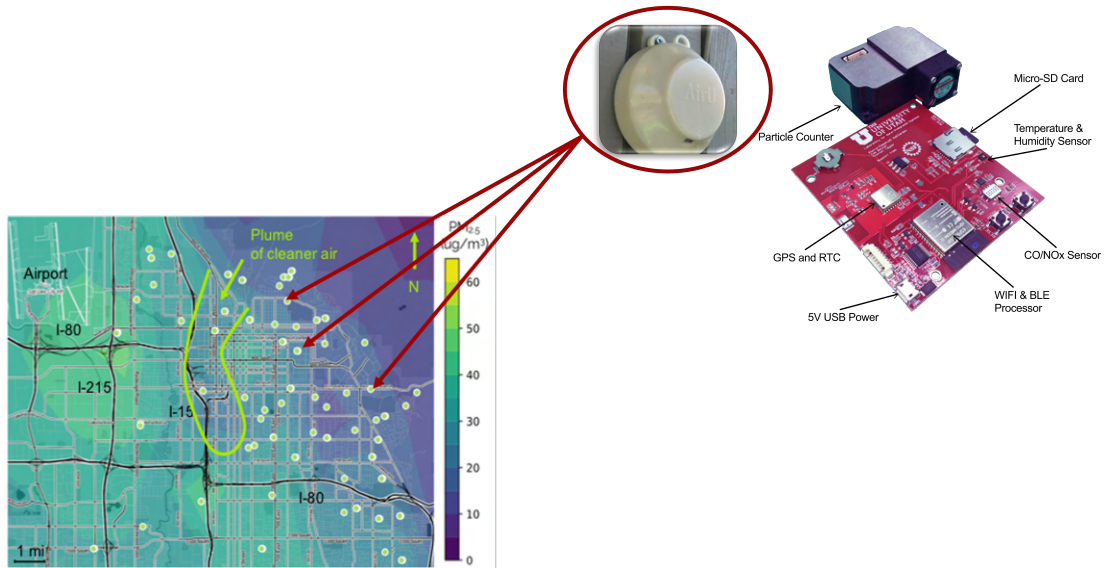


Figure 2.1: Picture of the annotated electronics of the AirU node in its case (circled in red), deployed in the valley of Salt Lake City.

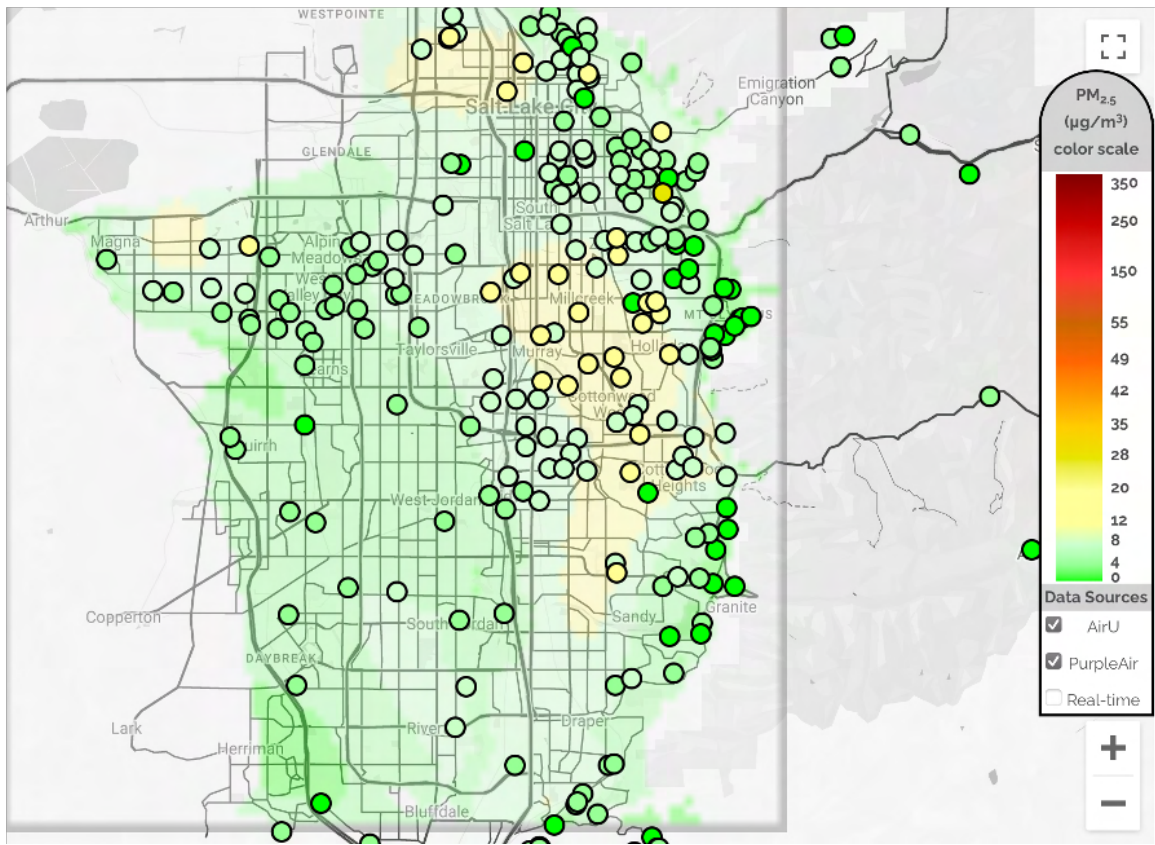


Figure 2.2: Detailed map of the $PM_{2.5}$ concentration in the area of Salt Lake City from Tellus Networked Sensor Solutions.

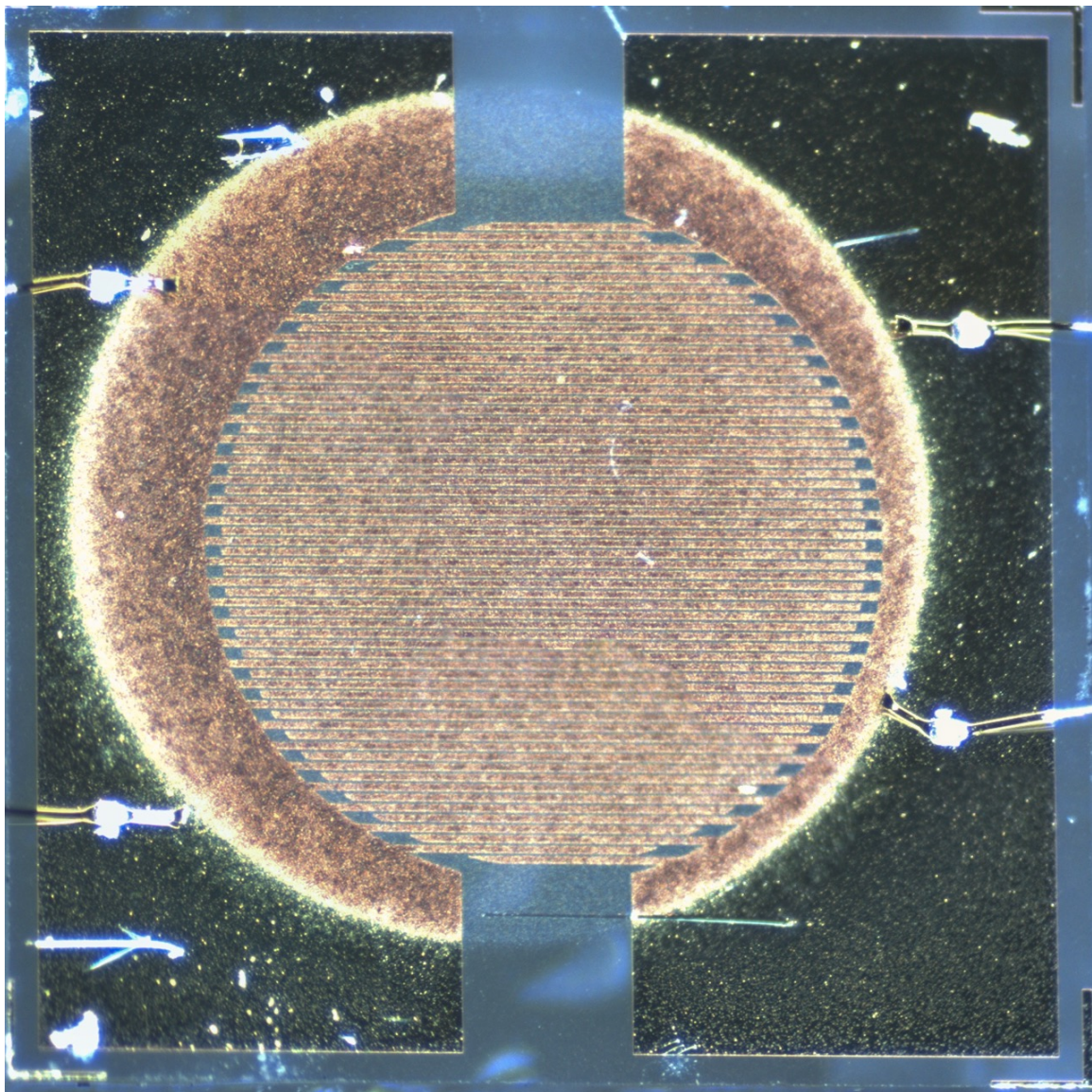


Figure 2.3: A macrophotography of the nanofiber-based sensor. Left and right side correspond to the *Sensor-* and *Sensor+* gold PADs for wirebonding. The self-assembled nanofiber is displayed in the middle circular shape.

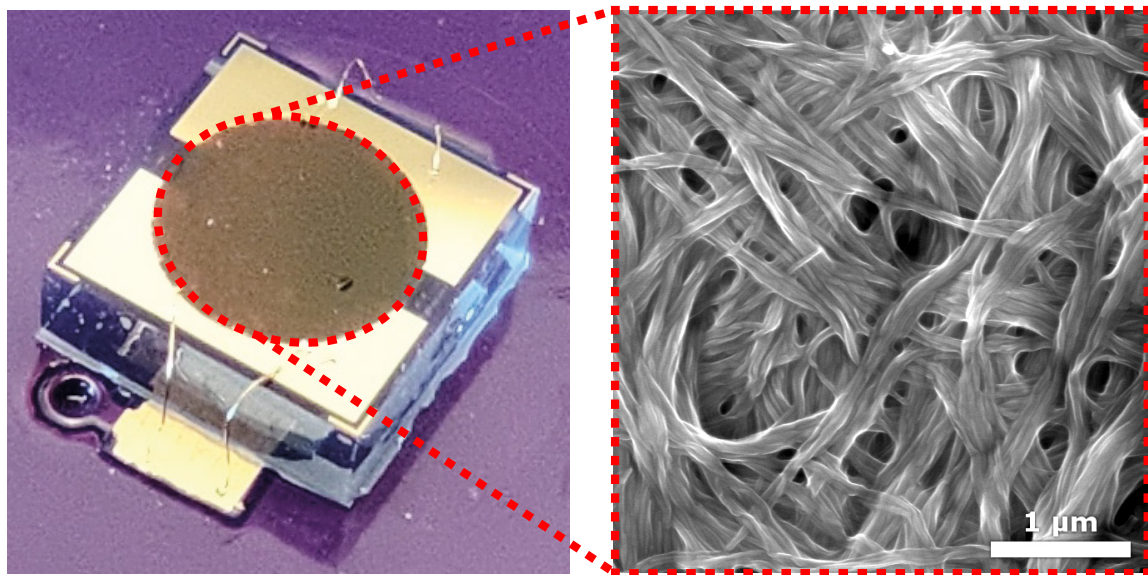


Figure 2.4: Picture of the nanofiber sensor package. Left: The wire-bonded sensor on a PCB, with the annotated top-layer of nanofibers; Right: A scanning electron microscope (SEM) image of the nanofibers.

Figure 2.5: Cross-section diagram of the nanofiber based sensor. In orange: the quartz base block; In green and blue: the gold PADs representing *Sensor+* and *Sensor-* respectively; In purple: the deposited top-layer self-assembled chemiresistive sensor.

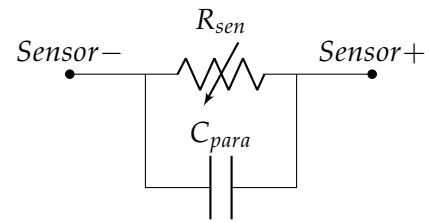


Figure 2.6: Equivalent electrical model of the nanofiber sensor.

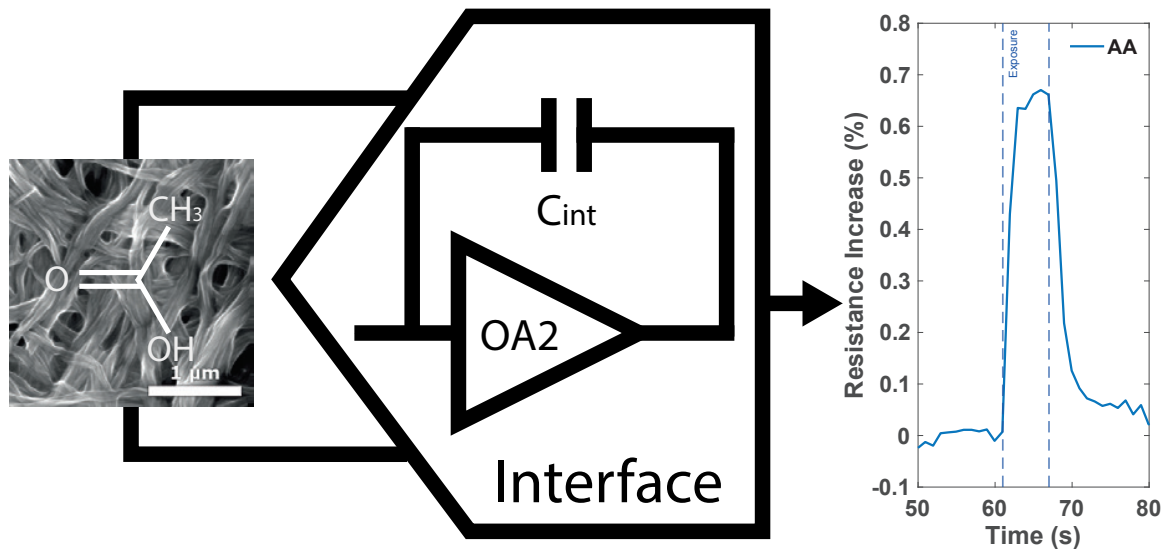


Figure 2.7: Top-level system implementation of the proposed chemical monitoring system. The interface directly connects to the nanofiber and record variations in resistance in real time. Data are transmitted through UART to an MCU for post-processing.

CHAPTER 3

A LOW-POWER AND LOW-COST WIDE-RANGE RESISTANCE TO DIGITAL INTERFACE FOR NANOFIBER SENSORS

While Chapter 2 focused on introducing ESN limitations and nanofiber technology, this chapter discusses the first set of contributions about sensor interfaces of this dissertation. We review state-of-the-art wide range resistance interfaces and propose to improve prior work with additional circuitry to interface nanofiber-based sensors. Section 3.2 describes a fully integrated wide range resistance to digital interface which provides a low-cost and high-performance solution for nanofiber sensors. The nanofiber-optimized ASIC presented in Section 3.3 revises the performance of the original interface to improve area and power. Our final contribution regarding sensor interfaces is presented in Section 3.4 and offers a low trade-off circuit variation for significantly improving sampling frequency and noise rejection. Section 3.5 provides a summary of sensor interfaces contributions.

3.1 Sensor Interfaces Background

3.1.1 State of the Art

The challenge in interfacing nanofibers comes from their intrinsic resistance value. This value can vary from as low as $500\text{ k}\Omega$ to up to tens of $\text{G}\Omega$ depending on the analyte of interest of the nanofiber and its concentration at a given time. This characteristic requires an ADC capable of handling this large resistor range and specifically, a low-cost, low-power analog front-end capable of interfacing $50\text{ G}\Omega +$ resistances. A comparison of state-of-the-art capabilities is shown in Table 3.1.

All the sensor interfaces [78–83] we are comparing our work to are based on a resistance to frequency converter, mostly due to the simplicity of the circuits to accomodate high dynamic range applications. They consist of a continuous *RC* integrator that oscillates with a frequency depending on the chemical population in the air. Some work, such as

[80] features a biasing circuitry and a set of current mirrors to keep a constant biasing voltage across the sensor, which is not necessary for nanofiber-based sensors. However, none of these prior works feature a variable integration time constant and variable gain to improve sampling rate at higher sensor resistance, which is discussed in Section 3.2.

Most state-of-the-art high dynamic range resistance interfaces are capped at $1\text{ G}\Omega$, primarily because it was not necessarily relevant to measure higher resistances before. These interfaces lack dynamic range to be compatible with nanofiber-based sensors and therefore, new types of low-power interfaces are required in order to upgrade AirU. While [83] can interface 100 G sensors, its lower dynamic range is too high (470k) to interface a wide variety of sensors. Another main problem with state-of-the-art interfaces is their output sampling rate. Having samples in the tens of seconds limits the signal of interest's bandwidth to low frequency signals of interest and any spikes in the chemical population (for instance, a group of molecules carried by wind) will not be detected. Studies about the response of the nanofiber-based sensors to a large step of chemicals show that the signal of interest remains in the lower 10 Hz which requires an output sampling rate near 100 ms to properly follow the output response of the nanofibers.

This section provides background on different technologies for gas sensing. This section shows the benefits of using nanofiber-based sensors in terms of performance and also showcases the challenges in interfacing those sensors. As none of the prior work can interface nanofiber-based sensors with high-sampling rate, we propose a high-performance and low-cost ASIC for interfacing nanofiber-based sensors for smart cities applications.

3.1.2 Interface Requirements for Nanofiber-Based Sensors

In the previous section, we identified a gap in state-of-the-art wide range interface regarding cost, sampling frequency, and range. Indeed, deploying a wide network of sensors across a city requires low-cost hardware for improving the spatiotemporal resolution of air quality data. Since prior wide range resistance interfaces do not include an on-board frequency-to-digital (F2D) converter, they require an external Programmable Logic Device (PLD) or Field Programmable Gate Array (FPGA) which increases cost, development time, and power. The minimum retail price for an FPGA is \$2.17 [84] as of the day of writing this manuscript which is the minimum cost increase for using state-of-the-art interfaces.

We propose to integrate the frequency-to-digital converter and UART controller within the ASIC for reduced cost, power, and complexity. We propose to increase sampling rate of state-of-the-art work to 100 Hz to be able to detect short burst of chemicals induced by nearby environmental or human influence.

Additionally, the characterization of the sensors in Section 2.2 is used to determine the required performance of the ASIC. Due to the large variations in baseline resistivity of the sensors, the ASIC must be able to interface resistances from at least 100 k Ω to 50 G Ω . The noise from the circuit must be kept low due to the small step responses of the sensors to chemical exposures ($> 0.7\%$) and the required signal-over-noise ratio (SNR) of 25 dB. The SNR is defined as the worst case sensor's response to noise level ratio as follows:

$$SNR = 20 \cdot \log_{10} \frac{\text{Smallest sensor response}}{\text{Noise floor}} \quad (3.1)$$

An SNR of 25 dB allows for a clear sensor response, linearly seventeen times higher than the noise level. Using Equation 3.1, we can derive the noise floor (jitter in *ppm*) of the system:

$$\begin{aligned} SNR &= 20 \cdot \log_{10} \frac{0.7\%}{\text{Noise floor}} \\ \iff &\frac{0.7\%}{\text{Noise floor}} = 10^{\frac{25}{20}} \\ \iff &\text{Noise floor} = 390 \text{ ppm} \end{aligned} \quad (3.2)$$

The power consumption of the chemical monitoring system must be kept low and non-significant compared to the baseline power consumption of the AirU node. The AirU node draws 540 mW of power during sampling. A power increase of 10 % is considered non-significant for AirU and allows for roughly 50 mW of power for the proposed chemical monitoring system. The nanofibers require a resistance to digital interface and LED biasing. The optimized power consumption point for the LED biasing (discussed in Chapter 4) is 1.65 mW per sensor which sets the maximum power consumption for the ASIC at 30 mW for all the resistance-to-frequency interfaces and the frequency-to-digital circuitry. Finally, the system must be low-cost and 12 sensors interfaces must fit into the smallest die area available for a shared MPW tapeout of 5 mm², leaving about 0.2 mm² per resistance to frequency circuit. Table 3.2 summarizes the targeted performances of the ASIC.

3.2 A Fully-Integrated Wide Range Resistance to Digital Interface

3.2.1 Improving Dynamic Range of Resistance to Digital Interfaces

This contribution discusses a novel wide-range resistor measurement circuit for interfacing highly resistive gas sensors at low measurement error. The circuit has been fabricated in a regular 180 nm CMOS process. Each sensor is connected to one analog front-end (based on a relaxation oscillator topology) which converts the resistance of the sensor to a frequency. The integrated digital controller computes the resistance value based on the aforementioned frequency, transmits the value through UART, handles autonomous calibration and range adjustment. With the implementation of a programmable gain amplifier (PGA) and a programmable capacitor integrator (PCI), the system improves sampling frequency by 5× compared to [83]. The circuit also has a calibration mode to improve measurement error by 3×, and dynamic range is also increased by 20 dB against state-of-the-art resistor interfaces [78–83, 85, 86].

3.2.2 The Proposed Integrated Interface for Sampling Highly Resistive Sensors at Low Measurement Error

This section discusses the proposed system architecture and its differences compared to state of the art.

3.2.2.1 Top-Level Architecture

Research has shown that resistance-to-frequency converters (R2F) are great choices for interfacing a wide range of resistances for the following reasons: First, their complexity is pretty low, and they require low area and reasonable power consumption. Secondly, prior work [87, 88] has shown the potential of using different integration constant τ and gain G to enhance the operating range of the analog front-end for low resistivity sensors. Finally, digitizing a frequency is a relatively simple task for an integrated digital controller [89]. This contribution proposes to improve current resistance to frequency converters through three main enhancements:

- The R2F features an integrated bandgap generator, biasing the sensor with two distinct temperature invariant voltage references.
- The R2F features a PGA in its forward path for better noise immunity.

- The application-specific integrated circuit (ASIC) includes a digital controller (DC) to enhance measurement accuracy through autonomous calibration and range selection. It reduces power consumption and cost compared to state-of-the-art that use an external device to compute the output frequency of the R2F.

3.2.2.1.1 System and ASIC presentation. The system block diagram, composed of the sensors, the ASIC, and an external MCU is shown in Figure 3.1. The proposed ASIC seamlessly interfaces resistive sensors to an MCU. The sensor is directly connected to the resistance-to-frequency circuit that provides biasing voltages to the sensor. It generates a frequency F defined by the value of the sensor's resistance value. The DC computes the value of the resistance based on the measured frequency F . Once computed, the resistance value is sent over an Universal Asynchronous Receiver Transmitter (UART) to the microcontroller unit (MCU). The DC can also configure the R2F through the PGA and PCI to keep the relaxation oscillator around its optimal operating frequency. The DC also controls the calibration mode and can swap the measured resistance to an external reference resistor to re-calibrate internal registers and improve measurement error. Finally, the MCU can configure the DC with pre-defined UART commands to trigger a re-calibration or force a specific gain on the PGA. Compared to state-of-the-art, our propose ASIC does not require external programmable logic devices (PLD) of field-programmable gate array (FPGA) to connect to an MCU.

3.2.2.1.2 Resistance-to-frequency converter presentation. Figure 3.2 presents the schematic of the R2F. The architecture is fairly common and shares similarities with previous work. The R2F is based on an inverting integration stage and a threshold comparator as in [78–83]. The integration stage defines the oscillation frequency of the oscillator and the comparator controls the phase of the system and keeps the loop in an oscillating mode. The oscillation frequency of the loop is defined by the time constant of the oscillator $\tau = R_{sen} \cdot C_{int}$.

Our analog circuit differs from previous work in two aspects:

- The R2F generates two biasing voltages for the sensor. Previous work either biased the sensors at a constant voltage [82, 86] or biased the sensor using power rails [83]. Our previous sets of nanofiber sensor's characterization have shown a constant baseline drift in the sensor response when biased at a constant voltage using a source

measurement unit (SMU). We believe this is due to the constant injection of energy into the sensor. Further investigations showed improvement in baseline drift when biasing the sensors with pulse width modulation (PWM) at opposite voltage levels. For this reason, we propose to use an on-board voltage reference generator to bias the sensors. This comes at the expense of area and power consumption but dramatically improves the ASIC flexibility. Our sensor's characterizations have shown reliable chemical responses when biased at around 1V. For this reason, the on-board temperature invariant voltage generator generates two voltages $V_a = 2.65$ and $-V_a = 0.65V$, to bias the sensor at either 1V or -1V. However, thanks to a rail-to-rail input buffer, the circuit can bias the sensors from 0V to 1.65V using external reference voltages or different on-board voltage levels.

- The circuit has an amplifying stage around the operational amplifier OA3 in series with the integrator. Previous work [83] placed the gain stage in parallel to control the comparator's threshold levels. Such a design choice comes at the cost of power consumption. OA3 is placed in a gain stage with a gain > 1 compared to a gain < 1 if placed in parallel. This extra closed-loop gain requires a faster operational amplifier to operate at the same loop oscillation frequency as prior work but provides greater benefit in terms of noise immunity. This issue can be observed in [83]. When interfacing highly resistive sensors, the comparator's input signal from the integrator is quasi-constant, resulting in spurious commutations and higher jitter. As discussed in Section 3.2.2.2.2 and [90], the output jitter of a comparator is inversely proportional to the input slope of the triangle waveform.

$$\begin{aligned}
 V_{in} &= \begin{cases} V_a & \text{if } V_c \text{ is high} \\ -V_a & \text{if } V_c \text{ is low} \end{cases} \\
 V_{int} &= \frac{-1}{R_{sen} \cdot C_{int}} \int \left(\frac{V_{DD}}{2} - V_{in} \right) dt \\
 V_{amp} &= -G \cdot V_{int} \\
 V_c &= \begin{cases} \text{high} & \text{if } V_{amp} < V_{in} \\ \text{low} & \text{if } V_{amp} > V_{in} \end{cases}
 \end{aligned} \tag{3.3}$$

3.2.2.1.3 Resistance-to-frequency circuit analysis. The four voltages, V_{in} , V_{int} , V_{amp} , and V_c characterize the behavior of the R2F and are defined in Equation 3.3 and plotted in Figure 3.3.

The integration capacitor C_{int} is charged or discharged based on the input voltage V_{in} at a constant current $|I_{int}| = \frac{|V_{in} - V_{DD}/2|}{R_{sen}}$. The integration stage output voltage is V_{int} . The operational amplifier OA3 amplifies V_{int} at a controllable gain G such that $V_{amp} = -G \cdot V_{int}$. The amplified voltage V_{amp} is then compared to V_{in} by the output comparator. The comparator's output V_c controls the input signal V_{in} .

At T_1 (in Figure 3.3), the oscillator starts a new phase of oscillation, C_{int} is discharged, $V_{amp} = V_a$. Between T_1 and T_2 , $V_{in} = -V_a$, and the capacitor charges because of the inverting nature of the integrator. V_{amp} also has an added phase of 180° because of the inverting nature of the gain stage, and its value discharges down at a slope rate of $\frac{G}{R_{sen} \cdot C_{int}}$. At T_2 , C_{int} is charged, $V_{amp} = -V_a$, the comparator triggers and the capacitor charges back up. The phase between V_{in} and V_{amp} is $0^\circ + / - 360^\circ$, required for oscillations when $-V_a < V_{int} < V_a$. However, during start-up, V_{int} is unknown and is set to a random value between the power rails depending on the ramps of the different biasing voltages. This is because of the lack of DC biasing within the integrator stage. For this reason, it is necessary to discuss the power-up sequence to ensure the circuit converges to an oscillation state in a bounded amount of time. We identify three different start-up scenarios, $V_{int} < -V_a$, $V_{int} > V_a$, or $-V_a < V_{int} < V_a$. The latter causes no issue because V_{int} is already within the range of oscillations. The circuit will either start to charge or discharge to one of the reference voltages. When $V_{int} < -V_a$, the worst condition is for $V_{int} = GND$, which implies $V_{amp} = V_{DD}$, which also implies $V_{amp} > V_{in}$, and therefore $V_{in} = -V_a$ based on Equation (3.3). In that configuration, the circuit automatically charges the capacitor up to V_a , and oscillation starts. The initial period will have an added time $\Delta t = |V_a| \cdot R_{sen} \cdot C_{int}$.

The oscillation frequency of this relaxation oscillator is defined by Equation 3.4 where T_{comp} refers to the time difference between two front-edges of V_c , τ is the time constant of the integrator, and G the gain of the amplifying stage.

$$F = \frac{1}{T_{comp}} = \frac{G}{4 \cdot \tau} \quad (3.4)$$

The integrator is placed before the amplifying stage and toggles at $V_{int} = \frac{V_a}{G}$. Increasing the gain of the amplifying stage makes the integrator oscillate faster as its output amplitude decreases. This effect is similar to reducing the size of the integration capacitor because a smaller capacitor charges faster.

3.2.2.1.4 Effects of non-idealities on the output frequency. The non-idealities of the different elements impact the ideal behavior of the circuit and lead to deviations from Equations 3.3 and especially 3.4. The primary sources of error are considered to be:

- Offset voltage V_s and leakage input current I_n of the OA
- Finite DC gain of the amplifying stage voltage creating an output error α defined as

$$V_{amp} = G \cdot V_{int} + \alpha$$

- Errors in the buffers creating an output error β defined as: $V_{in} = V_a + \beta$
- Non-symmetric voltage references with a voltage error δ defined as: $V_1 = +V_a$ and $V_2 = -V_a + \delta$
- Loop delay T_d due to the comparator, switches, and buffers.

Prior work[78] has derived the effect of the previous non-idealities on the oscillation period. The authors have shown that all these non-idealities (besides T_d) can be included in a γ term defined in Equation 3.5.

$$\begin{aligned} \gamma &= \frac{V_a(V_a - \delta) + \frac{\delta^2}{4}}{V_a(V_a - \delta) - (I_n R_{sen} + V_s - \beta)(I_n R_{sen} + V_s - \beta - \delta)} \\ T_{comp} &= 4\left(\frac{R_{sen} C_{int}}{G} + T_d\right)\gamma \end{aligned} \quad (3.5)$$

According to [78], the error introduced by γ is less than 0.0001 with typical values and $R_{sen} = 10G\Omega$. In our case, with $R_{sen} = 50G\Omega$, $V_a = 1V$, $\delta = 50mV$, $\beta = 0.5mV$, $I_n = 0.1pA$, $V_s = 0.5mV$, and the coefficient γ results in an error of about 0.0004. Gamma is estimated to be 1. The loop delay T_d is less than 100ns. The oscillation of the loop needs to be more than 30 μs to keep the error introduced by T_d below 0.35%.

The circuit is stable as long as the choice of the programmable gain and integration capacitance mitigates the effect of the sensor's parasitic capacitance C_{para} that is in parallel with R_{sen} . The circuit remain stable as long as G and C_{int} follow: $\frac{C_{int}}{G} > C_{para}$.

3.2.2.2 The Integrated Analog Front-End

The R2F circuit is based on a relaxation oscillator topology. The following paragraphs discusses the amplifier' used in the oscillator as well as noise performance of the oscillator.

3.2.2.2.1 Amplifiers specifications. The R2F circuit shown in Figure 3.2 is built around three main OAs. The primary sources of error of this architecture discussed in [78] come from:

- The voltage offset of OA2 and the comparator

- The input current of OA2
- The delay of the comparator and OA1.

The different active blocks in the system have been designed based on the previous assumptions. Although the best trade-off between the R2F's area, power, and performance is achieved when optimizing each individual OA, the design and layout effort is greatly reduced when using a single OA architecture for all three OAs. The transistor-level architecture of the OA we used for this oscillator is shown in Figure 3.4, and the sizing of the transistors in Table 3.3. This architecture was introduced and extensively explained in [91]. The OAs are based on a two-stages rail-to-rail input and output architecture. The OAs are biased by V_{bias} , generated by the bandgap reference voltage generator. Rail-to-rail input and output are necessary when the sensor is externally biased with voltages up to power rails. The input stage composed of $M_8 - M_{11}$ forms an N-channel and P-channel input differential pair in parallel and can reach the positive and negative power rails. The output class-AB stage is formed by $M_{31} - M_{32}$ and is driven by a floating class-AB control stage with $M_{21} - M_{22}$. The other transistors serve as biasing circuitry for the different stages and form floating current sources with $M_{15} - M_{16}$ to reduce the amplifier's input noise and offset voltage. In such a configuration, most noise performance and offset voltage depend on the amplifier's input stage. C_{comp} is a compensating capacitor using the Miller technique. It splits apart the poles of the two stages, and stabilizes the OA. Figure 3.5 shows the bode diagram of the OA and its performance is summarized in Table 3.4. The comparator is based on this architecture, without C_{comp} compensation, and its delay T_d is below 20ns.

3.2.2.2 Noise analysis. Previous literature [90, 92] has established equations to determine the noise level of different comparator-based architectures. These equations help design the operational amplifiers to meet the expected level of noise and jitter in the system. For this work, we have based our analysis on Equation 3.6 from [90]. α is a constant coefficient of normalization between 0.5 and 1 and depends on whether the noise has low or high frequency components compared to the triangle waveform. Its value can be derived from [90], with the worst case scenario of $\alpha = 1$ for all resistor values. The slope is defined as $Slope = \frac{G}{R_{sen}C_{int}}$, and $V_n(RMS)$ is the input equivalent noise of the circuitry at the input of the comparator. $V_n(RMS)$ depends on the noise at V_{amp} and the noise level of

the V_{in} buffer (which is a fixed voltage that toggles between $+V_a$ and $-V_a$ and its noise level must be traded-off between speed, noise level and area). The noise level at V_{amp} depends on the noise bandwidth of the integrator defined as $Noise_{BW} = \frac{1}{4 \cdot R_{sen} C_{int}}$, which makes the noise contribution of V_{amp} negligible if the noise from the power supply is low or properly rejected. Substituting these equations in Equation 3.6, the required output noise level of the system can be derived and is shown in Equation 3.7. The noise performances of the circuit can then be determined based on the required level of output jitter, it must be noted that the system will suffer from noise at higher resistance values. The choice of integration capacitance and gain can be picked to meet noise requirements.

$$\sigma(\delta T) = \alpha \sqrt{(6)} \frac{V_n(RMS)}{Slope} \quad (3.6)$$

$$V_n(RMS) = \frac{\sigma(\delta T) \cdot G}{\alpha \cdot \sqrt{6} \cdot R_{sen} C_{int}} \quad (3.7)$$

The amplifiers' thermal and flicker noise performance can be determined from Equations 3.6 and 3.7 using a simple circuit model. Our amplifiers' noise performance reported in Table 3.4 are for a R2F output jitter of 200 *ppm*.

3.2.2.3 The Integrated Digital Block

Compared to prior work where the oscillation frequency of the relaxation is processed externally using an FPGA, a PLD, or benchtop frequency measurement units, we propose to implement the circuit within the ASIC itself, as shown in Figure 3.6.

3.2.2.3.1 R2F's output frequency conversion. The system is clocked using a 40MHz reference clock. The digital controller outputs a packet on the UART at a sampling period $T_s = 200ms$, generated by the reference clock. The R2F oscillation period T_{comp} is estimated every sampling period T_s by incrementing two different counters, shown in Figure 3.6 and Equation 3.8. The counters' outputs are N_{ck} and N_{comp} . N_{ck} is defined as the number of reference clock front-edges between the first and last front-edge of the oscillator, over one sampling period. N_{comp} represents the number of periods of the oscillator over one sampling period. The measurement of T_{comp} has an error of at most two clock periods T_{ck} , with $error = \frac{2}{T_{ck}} = \frac{2}{40MHz} = 50ns$. The value of the sensor's resistance is computed based on the gain and integration capacitance configuration following Equation 3.8.

$$R_{sen} = \frac{G \cdot T_{comp}}{4 \cdot C} = \frac{G}{4 \cdot C} \cdot \frac{N_{ck} \cdot T_{ck}}{N_{comp}} \quad (3.8)$$

3.2.2.3.2 Dynamic calibration. One of the purposes of the digital controller is to handle the automatic calibration. The primary source of error in the system when estimating resistance value comes from the value of the capacitor C_{int} , used in Equation 3.8. An integrated circuit can match different components very well, which is also why the gain in Equation 3.8 is not a source of error. Because its value relies on a resistance ratio, a typical error below 1 % is easily achievable with a thorough layout [93]. However, it is difficult to estimate the raw value of components such as the capacitor C_{int} , whose capacitance value can vary over a large range (up to 20 % mismatch is common [94]). Thus, an external precision resistor R_{ref} is used.

The circuit toggles to calibration mode every few measurements and switches the input resistance from the sensor to the precision resistance, as shown in Figure 3.6. Based on the measured τ , the circuit calibrates the integration capacitor value.

By substituting Equation 3.9 for the capacitor value calculated during calibration mode into Equation 3.8 for the resistor during sensing mode, Equation 3.8 can be simplified. With a constant measurement period and reference clock frequency, the equation for the sensor's resistor is a proportional relation with the reference resistor using the gain and counts of the calibration and sensing. The sensing calculation is, therefore, independent of the reference clock frequency, measurement period, and capacitor value. The computed resistance value is now defined by Equation 3.10. G_{cal} and G_{sen} correspond to the gain during calibration and the gain during sensing, respectively. $N_{comp-cal}$ and $N_{comp-sen}$ are the N_{comp} counts during calibration and during sensing, respectively, and R_{ref} is the reference resistor value in ohms.

$$C = \frac{N_{ck}}{4 \cdot G_{cal} \cdot R_{ref} \cdot N_{comp-cal}} \cdot T_{ck} \quad (3.9)$$

$$R_{sen} = \frac{G_{cal} \cdot N_{comp-cal} \cdot R_{ref}}{G_{sen} \cdot N_{comp-sen}} \quad (3.10)$$

3.2.2.3.3 Operating modes. The system uses a finite state machine to control switching between the calibration, calculation, measurement, and transmit states, as shown in Figure 3.6.

Periodically (around once a minute), the device will connect the reference resistor in place of the resistor under measurement using transmission gates controlled by the digital

controller. The gain during calibration and the reference count of the capacitor measurement are stored in a calibration register.

The gain value varies between 1, 10, and 100; and is controlled by the digital controller. While the system is running, the counter output is checked for an underflow or overflow condition and adjusted. This prevents instability or loss of resolution if the integrator is charging too quickly or too slowly. The autonomous range selector uses the following two conditions to configure the ranges shown in Table 3.5:

- The range is increased by one when: $N_{comp} < 2$. This condition ensures that the R2F has at least one period of oscillation per sampling period ($T_{comp} < T_s$).
- The range is decreased by one when: $\frac{N_{ck}}{N_{comp}} < 800$. This condition ensures that there are at least 800 counts per oscillation period. It ensures that the measurement error is not limited by the 40MHz clock and the 50ns resolution of the counters, and that the loop delay T_d is negligible.

3.2.2.3.4 Arithmetic optimization. Calculating the resistance in Equation 3.10 requires a large arithmetic logic circuit. Area was of particular concern due to the need to share die space with the analog circuitry. Any delays during calculation are acceptable because the sample period is measured in hundreds of milliseconds. The arithmetic is implemented using pipeline multiplier and dividers done in fixed point binary. The pipeline multiplier/divider consists of a series of shift and addition/subtraction operations, analogous to grade school multiplication or long division. This strategy provides a compact circuit, at the expense of runtime. Each shift and add operation requires one clock cycle, for a total number of cycles equal to the number of bits. The implementation only requires a single addition operation per cycle, which reduces the size of the circuit. The output word length for the resistance is 40 bits.

The device communicates via a serial UART, enabling data transmission and the ability to receive configuration commands. The measured resistance is broadcasted over the UART periodically after each measurement. The parameters that can be configured via the UART include T_s and the reference resistor's value R_{ref} .

3.2.3 Circuit Performance and State of the Art

This section discusses the post-silicon results and compares the chip's performance to state-of-the-art resistance to digital interfaces. We show a proof of concept using this type

of architecture for nanofiber-based sensors.

3.2.3.1 Post-Silicon Results Against State of the Art

Although many resistance to digital exist, our application not-only targets wide range resistance interface but also very high resistance interfaces. Our comparison only includes prior work capable of interfacing $1\text{ G}\Omega+$ resistances.

3.2.3.1.1 State of the art limitations. A comparison of state-of-the-art capabilities is shown in Table 3.6. Most of the state-of-the-art high dynamic range resistance interfaces are capped at $1\text{ G}\Omega$, primarily because it was not necessarily relevant to measure higher resistances before. These interfaces lack the dynamic range to be compatible with highly resistive sensors. Nanofiber-based sensors and their counterparts cannot be interfaced, and therefore, new types of low-power interfaces are required to improve smart cities' detection capabilities. While [83] can interface $100\text{ G}\Omega$ sensors, its lower range limitation is too high ($470\text{ k}\Omega$) to interface various sensors. Another main problem with state-of-the-art interfaces is their output sampling rate. Having samples in the tens of seconds limits the signal of interest's bandwidth to DC measurement, and any spikes in the chemical population (for instance, a group of molecules carried by the wind) will be filtered out in the process. Studies about the response of the nanofiber-based sensors to a large step of chemicals [64] show that the signal of interest remains in the 1 Hz range, which requires an output sampling rate near 200 ms to properly follow the output response of highly resistive sensors.

3.2.3.1.2 Post-silicon results. The circuit has been fabricated in a 180 nm process node, and a die photography with annotations is shown in Figure 3.7, and area distribution is summarized in Figure 3.8. The ASIC has been packaged in a DIP-28 package. Post-silicon results are shown in Figure 3.9. We show that this work can interface chemi-resistive sensors with intrinsic resistance from $5\text{ k}\Omega$ to $50\text{ G}\Omega$ which is wider than any of the state-of-the-art resistance to digital interfaces that we have seen so far. The interface power consumption and area are kept as low as 5.3 mW and $< 1\text{ mm}^2$, respectively, to easily scale the number of channels. Measurement error was established by calibrating laboratory resistors using a silicon analyzer and then comparing the output of the ASIC to this calibrated value.

Corner analysis and PEX simulations were passed for commercial and industrial temperature standards from -10°C to 80°C across all corners. Due to the limited number of fabricated ASICs, we could not test the chip across all corners. However, the chip has been tested across temperatures, as shown in Figure 3.10. For this test, the chip was interfacing a 0.05%, $0.2\text{ppm}/\text{C}$ reference resistance of $100\text{k}\Omega$. The chip maintained a relative measurement error below 1%, or equivalently 6.5 effective number of bits across the whole temperature range from -40°C to 105°C . We have picked the value of *6.5bits* of *Effective Number of Bits* (ENOB) to be on par with state-of-the-art interfaces. This temperature range is compatible with commercial and industrial standards. Figure 3.11 provides a screenshot of the oscilloscope when interfacing the $100\text{k}\Omega$ resistor at room temperature. The measured frequency of $f_{\text{meas}} = 5.084\text{kHz}$ corresponds to a 0.29% measurement error compared to the expected and calibrated frequency $f_{\text{ideal}} = 5.099\text{kHz}$. The relative standard deviation is below 300 *ppm* for an SNR above 70dB .

Post-silicon results have also shown some limitations during testing. Range 4 from Table 3.5 was simply not usable at higher resistance values because of stability issues. We believe the capacitance value of 0.35pF is too small for the integrator to charge properly. On our test interface, the lowest capacitance we could use (with $> 1\text{G}\Omega$ resistances) was in the order of 20pF . This limitation reduced the sampling frequency to 5Hz but still remained on par or better than [78, 80, 81, 83].

These values are on par with our comparison table's best value [83]. The combination of the high dynamic range, the 0.35% error, and the high sampling rate makes this chip a better choice for gas sensing applications. [83] suffers from a slower sampling frequency and higher measurement error for detecting fast gas variations. Peaks will not be very precise or, worst, completely filtered out and aliased. The other works [78–82] are limited by their dynamic range and simply cannot interface highly resistive sensors.

3.2.3.2 Circuit Performance with Chemical Sensors

After characterizing the ASIC performance and comparing the system to state-of-the-art chemi-resistive sensor interfaces, we demonstrated this architecture's capability to interface nanofiber-based sensors. In this experiment, we interface an acetic acid nanofiber and study the system's response when exposed to acetic acid vapors. We used acetic

acid due to its simplicity. Acetic acid comes in a calibrated permeation tube used in a permeation oven to generate a controlled and quick exposure of low concentrations of vapors in an environmental chamber. The sensor is first exposed to zero air (pure inert gases) at room temperature and regular humidity for 60 s. Our system features multiple *Mass Flow Controllers* (MFC) to dilute the output of the permeation oven (generating acetic acid at a calibrated concentration) with zero air down to 40 *ppb* of acetic acid. We then use a combination of electronically controlled valves to precisely expose the sensor to 5 s of diluted analyte. The gas lines are controlled in temperature using a water bath, and a humidity generator sets the humidity of the vapors. The system successfully detects acetic acid, as shown in Figure 3.12. When exposed to 40 *ppb* of acetic acid, the sensor responds with a 0.66 % increase in its intrinsic resistance relative to the baseline. The sensor's response to 40 *ppb* of acetic acid has been repeated over 60 times. The average resistance increase relative to baseline is 0.64 %, with a standard deviation of 0.04 %. The system reaches 90 % of its peak response within 1 s and returns to 10 % after 10 s. This demonstrates the ability to monitor short exposures of low concentrations of analytes, which is typical for urban environments.

3.2.4 Contribution Summary

In this section, we discussed a low-cost, 6 mW plug&play resistance-to-digital interface in a 180 nm CMOS process node. Our system uses an RC measuring circuitry to directly interface the sensor and convert its intrinsic resistance value to a frequency. The integrated smart digital controller ensures the stability of the resistance-to-frequency circuit while also sending the computed samples over the integrated UART interface. This contribution demonstrated the integration of five interfaces on the smallest die size available while showing a 5× improvement in sampling frequency and 3× improvement in measurement error compared to state of the art. Innovative use of the variable gain and capacitance increases dynamic range by 20 dB against state-of-the-art. Post-silicon testing showed that this ASIC could interface resistances from 5 kΩ to 50 GΩ with less than 0.35% measurement error. The ASIC performance was on par with state-of-the-art across industrial temperature range standards and kept a 1% measurement error from −40 °C to 105 °C at 5 Hz. The system demonstrates promising results, especially when interfacing acetic acid

sensors during short exposures to low concentrations of analyte.

3.3 A Nanofiber-Optimized Resistance to Digital Interface

3.3.1 Limitations of the Previous ASIC and Goals of the Low-Cost and Low-Power Redesign

The ASIC presented in Section 3.2 showed exceptional performance compared to state-of-the-art work. However, its implementation is not scalable enough to be used in an ESN node. First, the design of this ASIC can be scaled to up to five channels on a 5 mm^2 die, which does not meet the required 12 channels. The power consumption of the ASIC also fails to meet the requirements with a single channel requiring 5.5 mW , which meets the maximum allowed power of $30\text{ mW} + / - 10\%$ with only six sensors. In order to meet the required 30 mW for 12 channels, the power consumption must be scaled down by $2\times$, and area by $2.5\times$. The sampling frequency must be improved by $20\times$ to meet the required 100 Hz . Additionally, the previous ASIC's range can be reduced by $20\times$ from $5\text{ k}\Omega$ to $100\text{ k}\Omega$ to meet the required range for interfacing nanofiber sensors. This following section proposes to reuse the basics of the previous ASIC and trade-off performance to improve area and power. Finally, the PCB copper lines going from the ASIC to the sensors are high impedance, which means they are very sensitive to charge injection and cross-coupling. For this reason, the ASIC must feature shielding outputs to drive a shield guard for every nanofiber. The advantage of the AC shielding signal is that the sensor lines can be shielded with a signal in phase with the line signal, thus eliminating any potential between the line and the shield and minimizing parasitic capacitances and noise coupling. This ensures that the minimum amount of noise from external aggressors (clock, serial lines).

3.3.2 Improving the Resistance-to-Frequency Converter

3.3.2.1 Power Consumption Optimizations

The R2F circuit presented in Section 3.2 is capable of interfacing resistances down to $5\text{ k}\Omega$. This lower boundary requires an input buffer capable of sustaining an output current $I_{out} = \frac{1\text{ V}}{5\text{ k}\Omega} = 200\text{ }\mu\text{A}$ and a peak output current during toggling of $I_{out-peak} = 2\text{ mA}$. Increasing the smallest interfacable resistance to $100\text{ k}\Omega$ sets the output current of the buffer to $I_{out} = \frac{1\text{ V}}{100\text{ k}\Omega} = 1\text{ }\mu\text{A}$. Therefore, reducing the size of the output buffer can significantly

improve power consumption. For this reason, the output current of the amplifier must be about $I_{out} = 60 \mu\text{A}$ and $I_{out-peak} = 1 \text{ mA}$, which allows for fast switching and mitigating the parasitics of the layouts. The extra I_{out} allows for using the OA as central buffers for $+V_a$, $-V_a$, V_{bias} , and $\frac{V_{DD}}{2}$. This allows for having one central voltage reference generator circuitry that generates the different biasing voltages for every channels and reduces area of the R2F significantly; Figure 3.8 shows that 23 % of the previous R2F was for the voltage generator.

The integration capacitance is now fixed for smaller area and reduced I/O's. The value of the integration capacitor is set at 36 pF for a total area of $18.000 \mu\text{m}^2$ giving a regular $2 \text{ fF}/\mu\text{m}^2$ mimcap density. The total mimcap area per R2F can be estimated to be about 15% larger due to routing and DRC rules for an area of $20.700 \mu\text{m}^2$. With the required 12 channels for a 5 mm^2 ASIC, the total mimcap area represents about $0.0207 \times 12 \text{ mm}^2$ or about 5 % of the whole ASIC, including wirebonding pads and IO ring. This value, coupled to a gain of 20 V/V on the gain stage makes this circuit compatible for sensors with a parasitic capacitance $C_{par} < \frac{C_{int}}{20} = 1.8 \text{ pF}$.

The circuit maximum toggling frequency is $F_{max} = 4 \cdot \frac{G}{R_{min}C_{int}} = \frac{20}{100 \text{ k}\Omega \cdot 36 \text{ pF}} = 1.4 \text{ MHz}$ which corresponds to a $T_{comp-min} = 720 \text{ ns}$. The loop delay T_d must be kept below $T_{comp-min}$ under any circumstances for the loop to be stable. The input buffer large step response is the main cause of delay in the loop and the large signal settling time of the OA must be below $\frac{T_{comp-min}}{2} = 360 \text{ ns}$. Moreover, at this maximum frequency F_{max} operating point, the gain stage slope is defined as $S_{max} = \frac{G}{R_{min}C_{int}} = 5.55 \text{ V}/\mu\text{s}$, the OA's slew rate requirements are $SR = 2 \cdot S_{max} = 11 \text{ V}/\mu\text{s}$.

Finally, the OA's noise performance matches the required SNR to analyse the nanofiber's response, for this reason, the noise and bandwidth of the OA do not need to be improved.

3.3.2.2 Operational Amplifier's Physical Implementation

The optimized OA has been designed based on the same topology as the previous OA, thus using the same schematic as in Figure 3.4. The optimized OA transistors' sizing is shown in Table 3.7. The main sizing difference comes from the biasing and output transistors which $\frac{W}{L}$ has been reduced to lower power consumption. The layout have been significantly improved with higher density and integrated decoupling capacitors

for power rails. Figure 3.13 presents the new layout compared to the previous one, the figures are on the same scale. The previous OA's size was $193 \times 100 \mu\text{m}^2 = 19.300 \mu\text{m}^2$ and the new OA is $160 \times 65 \mu\text{m}^2 = 10.400 \mu\text{m}^2$ and corresponds to a 46% decrease in area compared to the previous layout. Post parasitic extraction analysis has been performed across temperature and corners and the typical performances are shown in Table 3.8. These characteristics match the requirements sets in the previous Section 3.3.2.1 and this OA can serve as a general purpose OA for the optimized ASIC. Its area is improved by 46%, power consumption is reduced by 54%.

The comparator, required for closing the loop, does not require a large output buffer, therefore the size of the output buffer has been significantly reduced for lowering the power consumption by an extra 33% down to $P_{comp} = 0.2 \text{ mW}$ compared to the OA's power $P_{OA} = 0.3 \text{ mW}$.

3.3.3 R2F Physical Design

The ASIC is fabricated on a typical commercial 180 nm CMOS technode. The ASIC must fit on a minimum sized shared-block MPW tapeout of $2.5 \text{ mm} \times 2 \text{ mm} = 5 \text{ mm}^2$. The ASIC is using minimum sized wirebonding pads and a mixed-signal I/O ring. The ASIC is packaged in a QFN package and the minimum pads spacing specified by the commercial assemble facility sets the maximum number of pads the ASIC can feature. The spacings required by the sealring, I/O ring, pads, and DRC leave $2.090 \text{ mm} \times 1.580 \text{ mm} = 3.3 \text{ mm}^2$ for the core layout for which, 20% is allocated to the digital controller. The core layout must therefore fit in a 2.6 mm^2 area, or about $0.216 \text{ mm}^2/\text{ch}$. The 36 pF integration capacitor takes about 10% of that area and therefore, the R2F must fit in a 0.2 mm^2 area.

The maximum number of OA we can use in each R2F is set by the area and power limits. Therfore, power constraints are set to be $P_{Analog} = P_{ASIC} - P_{Digital} = 30 \text{ mW} - 7 \text{ mW} = 23 \text{ mW}$ or $P_{ch} = \frac{P_{ASIC}}{12} = 1.9 \text{ mW}$ per channel. Each R2F must also fit in a 0.2 mm^2 area. We can derive the maximum amount of OA that can be used in a single R2F based on the power consumption limits as follows: Each R2F include a single comparator and a set of OA. The OA power limit is determined after subtracting the power from the comparator and we thus can use $\frac{P_{ch} - P_{comp}}{P_{AO}} = \frac{1.7 \text{ mW}}{0.32 \text{ mW}} = 5.3 \text{ OA}$ per R2F. The power budget is met as long as we use less than 5 OA within the R2F, thus allowing for:

- One comparator,
- One OA for the input buffer,
- One OA for the integrator,
- One OA for the gain stage,
- Two OAs for shielding the lines.

We propose to implement the R2F following the schematic in Figure 3.14. The OA1, OA2, and OA3 serve the same purpose as in Figure 3.2. The added OA4 and OA5 serve as buffer for shielding the high-impedance sensor's lines to reduce the effect of external aggressors. The OAs' placement on the schematic in Figure 3.14 follow their physical placement on silicon and allows for a small die area of the 3 by 2 array of OAs. This placement reduces the feedback line length V_c , minimizes the sensors' lines length and parasitics, and allows for basic power and biasing voltages routing which simplifies the top-level arrangement of the 12 R2Fs on the die. Figure 3.15 shows the annotated layout of the optimized R2F. The physical implementation of the R2F takes $550 \text{ mm} \times 315 \text{ mm} = 0.17 \text{ mm}^2$ which is below the required 0.2 mm^2 area. This represents an 83% decrease from the previous design of 1 mm. Post silicon power consumption is about 1.7 mW per channel which is a 69% decrease.

3.3.4 Top-Level Physical Implementation

When meeting all the manufacturing rules and DRC rules, the ASIC can accommodate 18 I/Os on each of the 2.5 mm and 14 on the 2 mm side for a total maximum of 64 I/Os in this configuration. The R2Fs each require two I/Os for each sensor, and one I/O for the shield line for a total of 36 I/Os. The biasing voltages $\frac{V_{DD}}{2}$, V_{bias} , $+V_a$, and $-V_a$ are all routed to an I/O for external monitoring and decoupling for a total of four I/Os. Two I/Os are used for power lines V_{DDA} and GND . That is a total of 42 I/Os for the analog front-ends.

The top-level block diagram is shown in Figure 3.16 and the digital system requires three I/Os for power lines, one for the I/O V_{DDD} , one for the core V_{DDD} and one for GND . The digital controller needs one clock I/O, one reset I/O, an I/O pair for the UART transmission lines, and two I/O for setting the gain of the analog front-end. That is a total of nine I/Os for the digital controller and leaves 13 I/O availables for directly routing the output V_c of each R2F to the outside for external monitoring and noise measurements. The last I/O is left open for orientation during ASIC assembly, see in Figures 3.17 and 3.18.

Figure 3.17 proposes the annotated final layout of the ASIC. The digital I/Os are located on the top side and the digital controller is located north-east, close to the clock and UART lines for signal integrity and noise mitigation. The voltage reference circuit is located in the middle to feed all the R2F circuits. Finally, all the R2F are located on the outer side and facing the I/Os to minimize the sensors' lines length and reduce parasitics.

3.3.5 Post-Silicon Results

The ASIC has been designed and layouted using the Cadence suite. DRC, LVS, and PEX were performed using Calibre. The ASIC has been fabricated with a commercial 180 nm CMOS process node and packaged in a 72 pin QFN 10x10 package. Figure 3.18 is a macrophotography of the fabricated ASIC. Figure 3.19 shows the ASIC within the QFN package, and the test PCB is shown in Figure 3.20. We assembled an array of laboratory resistors on the PCB to test the performances of the ASIC from 10 MΩ to 20 GΩ to estimate the performance of the ASIC.

Post-silicon analog power consumption was measured at 19.7 mW. This represents a 1.64 mW per channel which is 3.5 % close from post-peX expected results and is within the range of power requirements. The voltage references have a noise level of 450 μ V_{RMS}. The ASIC can sample resistor up to 10 GΩ at 10 Hz. The performance of the ASIC has been estimated with a low-noise thin-film, 0.1 % accuracy 10 MΩ resistor on an R2F channel that features an external integration capacitor for calibration. Measurement error is on par with the previous ASIC (< 0.3 %) and the noise was measured on both the raw output of the R2F and the output of the UART over 10 s to capture noise from 0.1 Hz. The histogram of the measured raw frequencies are plotted in Figure 3.21 with an average measurement of 249.42 Hz compared to the expected 250 Hz (0.23 % error). The noise level is measured at 180.7 ppm which corresponds to a SNR of 74.9 dB and very close to post-PEX simulations. The noise has also been estimated on the output of the digital controller, which acts as a low-pass filter and noise level is at 30.1 ppm which corresponds to a SNR of 90.5 dB in Figure 3.22. The effect of shielding the lines has been measured on two lines, populated with a thick-film 1 GΩ resistor. The noise of both lines have been compared following the same noise measurement methodology as previously discussed. Both lines are located in the same PCB area, away from external aggressors such as clock signals, and each line is the

same length of 0.5 inch. The line with shielding shows a 25 % lower noise floor compared to the unshielded line.

The price of the ASIC is calculated based on a full-waffer tapeout. A typical commercial 200 mm wafer costs \$1,800 and can fit up to 5,300 dies resulting in \$0.34 per ASIC.

3.3.6 Contribution Summary

This section presents an area and power optimized R2F to fit more sensor interfaces on the same die surface within power budget. The contributions include the design and performance discussion of the ASIC with post-silicon results. The performance summary of the optimized ASIC is presented and compared to the requirements in Table 3.2:

- **Price:** The top-level layout is 5 mm² and includes the R2F and F2D converters. The cost of fabrication is \$0.34 per ASIC without packaging and external decoupling capacitors. The ASIC requires six decoupling capacitors for power and reference voltages, resulting in a total price of \$1 per ASIC. The ASIC has proven to be an extremely low-cost system for interfacing resistive sensors to an MCU and fits the cost budget for ESN nodes.
- **Power:** Post-silicon results have shown a power-consumption of 19.3 mW on the analog front-end and 6.5 mW on the digital controller for a total power consumption of 25.8 mW. The optimized ASIC is a very-low power system for interfacing resistive sensors to an MCU. Post-silicon power is 14 % smaller than power budget.
- **Noise level:** Post-silicon noise level is below 200 ppm, corresponding to a minimum sensor's SNR of $20 \cdot \log_{10} \frac{0.7\%}{200\text{ppm}} = 30.8$ dB. The measured SNR is 5.8 dB higher than the sensor's response to noise requirements. The optimized ASIC is a very low-noise integrated resistance-to-digital interface for resistive sensors.
- **Range:** The range requirements are met and the ASIC can interface resistive sensors from 100 kΩ to 10 GΩ, and up to 50 GΩ at reduced sampling rate.
- **F2D:** The frequency to digital converter is integrated on the same silicon, allowing for a straightforward integration of the ASIC within an ESN node. The included F2D can daisy chain up to 4 ASIC on the same UART line for up to 72 interfaced sensors.
- **Sampling:** As stated previously, the sampling rate of the ASIC is up to 10 Hz for sensors below 10 GΩ but sampling speed is reduced when the sensor's resistivity is above 10 GΩ.

The manufactured ASIC meets the power requirements, the price budget, the noise level, and wide range. However, this version of the ASIC lacks sampling frequency at higher resistance. Section 3.4 discusses the limitations in sampling frequency and proposes to improve the sampling frequency of the ASIC with additional circuitry within the R2F and novel F2D conversion techniques to improve sampling frequency up to the required 100 Hz.



3.4 Novel Techniques for Improved Sampling Frequency

3.4.1 Mitigating the Sensors' Parasitics Capacitance

Monitoring air quality in an urban environment with a wide variety of pollutants and complex air movements is a demanding task. Recent research has focused on using a combination of machine learning (ML) with an array of different sensors to determine air composition. Nanofiber-based sensors are a promising solution for this application but are challenging to interface at high sampling rate ($> 10 \text{ Hz}$) due to their high intrinsic resistance and parasitic capacitance. In order to maximize data throughput for feeding a ML model and improving the data stream for air quality analysis, we propose a new relaxation oscillator capable of mitigating sensor's parasitic capacitance for improving sampling rate.

This contribution's novel analog front-end offers better sampling frequency ($+30 \times$) and area/cost (-13%) compared to regular relaxation oscillators with minimal power trade-off ($+60 \mu\text{A}$ or $+14\%$). The maximum sampling frequency of 100 Hz at $50 \text{ G}\Omega$ is about $12 \times$ better than previous wide resistance interface capable of interfacing sensors between $100 \text{ k}\Omega$ and $50 \text{ G}\Omega$, with an average measurement error of 0.29 %. The circuit has been validated post-PEX along with a layout featuring 12 interfaces on a minimal 5 mm^2 die shown with a total power consumption of 2.65 mW per channel.

We demonstrate that the sampling frequency of relaxation oscillators with highly resistive sensors is limited by the parasitics of the interfaced sensors. This contribution proposes a low trade-off parasitics mitigation circuitry to improve sampling frequency when interfacing highly resistive sensors using resistance-to-frequency converters.

3.4.2 The Proposed Parasitics Mitigation Circuitry

3.4.2.1 Effect of Parasitics on Sampling Frequency

A typical relaxation oscillator circuit for interfacing a wide range of resistances [78] is shown in black in Figure 3.23. The blue blocks represent the proposed parasitics mitigation circuit further discussed in Section 3.4.2.2. This architecture generates a squared output signal V_c , which period T_c depends on the sensor's resistance R_{sen} as: $T_c = 4 \frac{R_{sen} C_{int}}{G}$. The operational amplifier (OA) OA1 generates V_{in} to bias the sensor at either $V_{sen} = \frac{V_{DD}}{2} + V_a = 1V$ or $V_{sen} = \frac{V_{DD}}{2} - V_a = -1V$. At DC, (when V_{in} has settled at either $+V_a$ or $-V_a$ and $\frac{dV_{in}}{dt} = 0$) all the current I_{int} charging the integration capacitor C_{int} is going through R_{sen} and $|I_{int}| = \frac{|V_{sen}|}{R_{sen}}$. However, during transient and when $\frac{dV_{in}}{dt} \neq 0$, the impedance Z_{c-para} of the parasitic capacitor of the sensor C_{para} is non-negligible and $I_{int} = C_{para} \frac{dV_{in}}{dt}$. The equivalent circuitry between V_{in} and V_{amp} is an inverting amplifier with a transient gain $G_{tran} = \frac{Z_{c-para}}{Z_{c-int}} \cdot \frac{R_2}{R_1}$ during transient. This creates a ΔV error at V_{amp} as shown in Figure 3.24, which impacts the oscillation period T_c of the converter as shown in Equation 3.11.

$$T_c = \frac{4R_{sen}C_{int}}{G} \left(1 - \frac{GC_{para}}{C_{int}}\right) \quad (3.11)$$

$$G = \frac{R_2}{R_1}$$

The oscillation frequency $F = \frac{1}{T_c}$ has an infinite value when $\frac{G \cdot C_{para}}{C_{int}} = 1$ and negative value when $\frac{G \cdot C_{para}}{C_{int}} > 1$ which is not physically possible. In fact, this equation defines the limit of usable G and C_{int} for a given sensor. If C_{int} is picked too low or G picked too high, the ΔV error shown in Figure 3.24 becomes higher than the thresholds of the comparator. As a result, the circuit enters a non-stable state and oscillates at a frequency defined by its loop delay T_{d-loop} dependent on the delay T_d for each OA. The designer must carefully pick the value of C_{int} and G to ensure the loop does not enter this state.

Substituting the value C_{int} into the ideal oscillation period of the loop $T_c = 4 \frac{R_{sen} C_{int}}{G}$, we get the equivalent minimum T_c that this architecture can establish which is defined only by the sensor's resistance and parasitic capacitance. These parasitics limit the sampling frequency of the architecture to the fabrication/technological capabilities of the sensors. For this reason, we propose to mitigate the effect of the parasitic capacitance C_{para} of the sensor to decorrelate the sampling frequency of the sensor's interface, from the sensor's parasitics. The following Section 3.4.2.2 discusses the novel parasitics mitigation circuitry.

Typical values for nanofiber-based sensors are $C_{para} = 3 - 5\text{pF}$; $R_{sen} = 1 - 10\text{G}\Omega$; $C_{int} > 60\text{pF}$; $T_c > 120\text{ms}$. At least one period of T_c is required in order to sample the oscillation period of the loop and subsequently the value of R_{sen} . Results in previous works [83, 95] are limited to a maximum sampling rate of one measurement every 1s with limitations due to noise. Other work improved sampling rate to 10ms [96] with the use of a multitude of comparators at the expense of area, power and required power supplies (10V).

$$C_{int} > C_{para} \cdot G \Leftrightarrow T_c > 4R_{sen}C_{para} \quad (3.12)$$

3.4.2.2 Design of the Proposed Parasitics Mitigation Circuitry

The proposed circuitry to mitigate the effect of the parasitics capacitance C_{para} from the sensor is represented by the blue blocks in Figure 3.23. The circuit detects when a transient is going to occur across the sensor (when $\frac{dV_{sen}}{dt} \neq 0$) and toggles the two switches S1 and S2 right before V_{in} changes. The control of the switches must happen before V_{in} changes voltage and this is ensured by adding a short delay block of a few nanoseconds ($< 5\text{ ns}$) in the feedback loop between V_c and S0 using inverters. The pulse generator detects any edge transition on V_c and triggers a pulse V_{pulse} after 1 ns that lasts 1 μs . When the pulse is high, S1 is open, S2 is closed for 1 μs . All the current $I_{int} = C_{para} \frac{dV_{in}}{dt}$ is now routed through S2 to a buffer generating $\frac{V_{DD}}{2}$. The capacitor C_{para} discharges at a time constant of $C_{para} \cdot R_{ON-S2}$ into the buffer within 1 μs which ensures enough time for discharging across all corners and tested temperatures (-40°C to 120°C). S1 and S2 are built around minimum sized transmission gate to minimize leakage current. This secondary current path during transient defines the new limits of oscillation period shown in Equation 3.13. In theory, T_c is higher than defined in Equation 3.13 and now fully depends on C_{int} and G which can be picked independently from C_{para} . With reasonable values of $C_{int} = 10\text{pF}$ and $G = 100$, the new limit of T_c is improved by $30\times$; $T_c = 4\text{ms}$ at $10\text{G}\Omega$.

Previous work [83] have used a combination of comparators and XOR gate to estimate the value of the parasitics capacitance of the sensor by measuring different timings. However, in our case, we can adapt this circuitry (shown as Comp2 and XOR in Figure 3.23) to generate a new signal V_{out} that oscillates twice as fast as V_c . Thanks to the use of simple circuitry to mitigate the effect of the sensor, we are able to improve the oscillation period by $60\times$ and $T_{out} = 2\text{ms}$ at $10\text{G}\Omega$. Compared with previous works mentioned, where the

oscillation is computed from front-edge to front-edge, we estimate the period on all edges resulting in an additional $2\times$ improvement and therefore improving the sampling rate by $120\times$. Figure 3.25 shows the output of the system V_{out} as well as the control signal V_{pulse} for S1 and S2.

Additionally, this topology allows for the use of level-triggered D-latches shown in red in Figure 3.23 to remove any spurious commutations of the comparators *Comp1* and *Comp2* due to noise. This is especially mandatory for higher resistances, when the slope of the triangle waveform V_{amp} is low. Effectively, this implementation is similar to a variable hysteresis on the comparators, with the hysteresis level automatically set to the noise level of the system.

The digital system depicted in the lower section of Figure 3.23, is intended to accurately measure the duration of the half period on signal V_{out} and then transmit enough information about V_{out} to derive its frequency off-chip. For each channel, the digital controller utilizes a reference clock set to 10 MHz to determine the number of reference clock periods between each falling or rising edge of V_{out} . Special blocks called "period counters" are employed to determine the number of reference clocks, the number of half periods of V_{out} , and the value of V_{out} for each channel on each capture. This information is then converted into a 40-bit package and sent via UART to the host per channel every 5ms. To achieve this, each channel consists of a synchronizer, to align the two clock domains (reference clock and channel in), a debouncer to combat noisy channel input, and a period counter to obtain the necessary frequency information from V_{out} . The digital system uses a multiplexer network in the finite state machine (FSM) to access each period counter output individually, register file to store output data that is ready to be sent off-chip, UART transmission block to handle communication and finally, a FSM to orchestrate the data movement between the analog front end and UART output.

This digital system's fundamental block is the period counter, which consists of registers and counters to obtain the information related to V_{out} frequency. Counter 1, synchronous to the reference clock, captures the number of reference clock periods between each V_{out} edge and is asynchronously reset on each V_{out} event, falling for rising. Two additional counters are sensitive to V_{out} and are used to monitor the number of half periods. Synchronous to the channel input and sensitive to the falling and rising edge

respectively, individual registers hold the intermediate values of reference clock count corresponding to rising and falling edges. These registers are updated with the current register values summed with the number of reference clock periods before a reset from counter 1. The intermediate values corresponding to rising and falling edges are summed and written to the register file, then stored until the next UART transmission. All registers and counters, excluding the reference clock counter, are cleared and reset after each UART transmission.

$$T_c > 2 * T_{pulse} = 2 \mu\text{s} \quad (3.13)$$

3.4.3 Performance of the System

The analog front-end shown in Figure 3.23 has been designed using the Cadence environment in a regular 180 nm CMOS process node across temperature (-40°C to 120°C) and all corners. DRC/LVS/PEX have been passed using the Calibre flow and all the results presented here are post-PEX. The layout of the analog front-end from Figure 3.23 is shown in Figure 3.26a, the area is $540 \mu\text{m} * 270 \mu\text{m} = 0.14 \text{ mm}^2$. The extra circuitry required for mitigating the parasitics is the 0.0036 mm^2 block number two, annotated in Figure 3.26a representing 2.5% of the total area. This circuit allowed for a smaller $C_{int} = 10 \text{ pF}$ compared to 36 pF previously, representing a total area reduction of 13.5% for the analog front-end. Power consumption increased by 14% ($+60 \mu\text{A}$) with the extra comparator Comp2 and sampling time is improved by $120\times$. The integrated digital controller depicted in 3.26b, operating at 10MHz, consumes 6.23 mW of the total power and represents $870 \mu\text{m} * 420 \mu\text{m} = 0.365 \text{ mm}^2$ of the total area.

An experimental setup consisting of ADExl and QuestaSim for analog and digital evaluation was used to estimate the performance of the system for a range of eleven resistances from $100 \text{ k}\Omega$ to $50 \text{ G}\Omega$. Analog waveform outputs from ADExl output were converted into verilog testbench files and then provided to QuestaSim to obtain approximately fifty UART output measurements for each resistance value over one-half second. These values are then post-processed to interpret the encoded 40-bit binary measurement packet. Jitter of the measurement system is obtained by taking the first standard deviation of the frequency and dividing it by the average value of the recorded frequency values, then represented as percentage in Figure 3.27. Similarly, measurement error of the system is obtained by

averaging post-processed frequency values for each resistance, then determining the relative error with respect to the expected resistance as a percentage. To accurately estimate the true measurement error of the system, multiple values of G are used to ascertain its effect on the system. The system measurement error is presented in Figure 3.27 in terms of the relative error adjusted by the Gain effect evaluation post-processing technique. Additionally, the parasitic mitigation circuit can handle parasitics capacitances up to 30 pF using a gain of 100 V/V.

The reference clock has a period of 100 ns, which corresponds to a maximum counts of 100,000 per UART transfer (every 10 ms). The period of oscillation of the loop is determined by the counts of reference clock per UART transfer, the digital controller can differentiate a variation in the period corresponding to 1 count. The resulting smallest amount of variation the system can monitor is therefore $\frac{1}{100,000}$ which corresponds to 10 ppm. If the baseline resistance of the sensor is minimal (100 k Ω), the system can differentiate a 1 Ω variation. If the sensor is around 50 G Ω , the system can differentiate a variation of 500 k Ω .

3.4.4 Contribution Summary

Since air pollution consists of a complex combination of chemicals in the air, it is necessary to interface a large array of chemical sensors and monitor their individual responses as a data stream with ML. The proposed nanofiber sensors are promising technology, but their extremely high intrinsic resistance makes them challenging to monitor at high data sampling. The proposed analog front end offers great benefits in terms of sampling frequency ($+30 \times$) and area/cost (-13%) for minimal trade-off in terms of power consumption ($+60 \mu\text{A}$ or $+14\%$). Moreover, the integrated digital controller enhances sampling frequency by up to $2 \times$ for a maximum sampling frequency of 100 Hz at 50 G Ω . Noise performance of the system has been simulated at 0.39 % on average across the 100 k Ω - 50 G Ω range with an average measurement error of 0.29 %. The novel parasitic mitigation circuitry can mitigate the effects of parasitic capacitance up to 30 pF with a power consumption of 2.65 mW per channel. Finally, the use of the additional comparator's output for loop-stabilization allows for complete immunity to spurious commutations.

3.5 Chapter Summary

In this chapter, we improved state-of-the-art wide range resistance interfaces through the following three major contributions, each representing a novel circuitry.

- The first contribution of this chapter is a **fully-integrated very wide-range resistance to digital interface**. The fabricated device differs from previous work in multiple aspects. First, the R2F features an integrated bandgap generator to bias the sensor with two distinct temperature invariant voltage references. This feature reduces the temperature dependency of the system and allows for biasing voltages up to the power rails. Secondly, the R2F features a PGA in its forward path for better noise immunity. This feature invertly improves the noise performance of the R2F compared to previous work and furthermore, allows for wider range because the higher threshold voltages for the comparator make the system immune to spurious commutations due to noise. Finally, the ASIC includes an integrated DC to enhance measurement accuracy through autonomous calibration and range selection. It reduces power consumption and cost compared to prior state-of-the-art which use an external device to compute the output frequency of the R2F. We have shown a **5 \times** improvement in sampling frequency and **3 \times** in measurement error compared to state of the art. Innovative use of the variable gain and capacitance increases dynamic range by **20 dB** against state-of-the-art. Post-silicon testing showed that this ASIC could interface resistances from **5 k Ω** to **50 G Ω** with less than **0.35%** in measurement error. **Power consumption and area were kept on par with prior work while including the F2D circuitry.**
- The second contribution of this chapter relies on **improving power consumption and area of the previously designed R2D interface for environmental monitoring**. The range was limited to the 100 k Ω to reduce area by **83%** and power consumption by **61%**. Thanks to the improvement in power consumption and area, a **12-channel R2D** was fabricated on a single minimum-sized 5 mm² die for a cost of **\$0.34** per ASIC. The equivalent post-silicon system power consumption per channel is **2.15 mW** with a **2 \times** improvement in sampling frequency. Finally, post-silicon noise is kept below **200 ppm** corresponding to a minimum sensor's SNR of **30 dB**.
- The last chapter's contribution investigated the effect of the parasitics capacitance

on the performance of the R2D. We derived that **the sensor's parasitics limit the sampling frequency of the electronics**. We proposed a low trade-off extra circuitry to mitigate the effect of the sensor's parasitics. The contribution presented a novel analog front end to improve sampling frequency by (**30 ×**) and area (**-13 %**) at low power trade-off (**+14 %** on the R2F). Additionally, the integrated digital controller enhances sampling frequency by up to $2 \times$ for a maximum sampling frequency of 100 Hz at $50\text{ G}\Omega$. Noise performance of the system has been simulated at **0.39 %** on average across the whole range with an average measurement error of **0.29 %**. The novel parasitic mitigation circuitry can mitigate the effects of parasitic capacitance up to **30 pF** with a power consumption of **2.65 mW** per channel. The contributed novel circuitry does not suffer from spurious commutations thanks to the use of stabilizing circuitry, allowed by the extra comparator.

Table 3.1: Comparison of state-of-the-art high-dynamic range resistance interfaces.

	[78]	[79]	[80]	[81]	[82]	[83]
Maximum sensor's resistance (Ω)	1G	3G	1G	100M	500M	100G
Power (mW)	600	Watts	15	11	35	4
ENOB (bits)	8	<8	6.5	8	6.5	6.5
size (mm^2)	2000	?	0.4	?	1	0.9
sampling (s)	10	100m	10m	5	<100m	1

Table 3.2: Required performances of the ASIC.

Parameter	Requirement
Cost (\$)	< 3
Power (mW)	< 30
SNR (dB)	> 25
Jitter (ppm)	< 400
Measurement Error (%)	< 1
Range (Ω)	< 100k to > 50G
Sampling (Hz)	> 100
Channels (nb. of sensor per ASIC)	> 12
F2D	Integrated

Table 3.3: Operational amplifier's transistor sizing.

Instance Name	M1	M2	M3	M4	M5	M6	M7	M8	M9	M10	M11	M12
W/L (μm)	8/8	8/8	8/8	8/8	8/8	4/8	128/8	20/0.5	20/0.5	40/0.5	40/0.5	128/4
Instance Name	M13	M14	M15	M16	M17	M18	M19	M20	M21	M22	M23	M24
W/L (μm)	16/1	8/0.5	8/1	16/1	16/0.5	32/1	16/1	8/0.5	8/1	16/1	16/0.5	32/1
Instance Name	M25	M26	M27	M28	M29	M30	M31	M32	C_{comp}			
W/L (μm)	2/8	4/8	8/8	4/8	7/8	7/8	48/1	96/1	340fF			

Table 3.4: Main characteristics of the OA.

OTA parameted	Post-Pex Values
Voltage Supply	3.3 V
Power Consumption	0.65 mW
GBW	40.1 MHz
Output Dynamic Range	GND to VDD
Input Dynamic Range	GND to VDD
Open Loop DC Gain	101 dB
Slew-Rate	33.5 V/ μ s
Offset Voltage	400 μ V
Input Noise @1 kHz	300 nV/sqrt(Hz)
Input Noise @0.1 Hz	30 μ V/sqrt(Hz)
Unity Gain Phase Margin	53°
Peak Output Current	2 mA
Large Signal Settling Time (1%), $V_{step} = 1V$	80 ns

Table 3.5: Configurable ranges of the ASIC.

Range	R_{sen}	<i>Gain</i>	C_{int}	T_{comp}
1	[5 kΩ; 3 MΩ]	1 V/V	500 pF	[10 μs; 6 ms]
2	[2.5 MΩ; 570 MΩ]	10 V/V	100 pF	[100 μs; 22.8 ms]
3	[170 MΩ; 1.5 GΩ]	100 V/V	100 pF	[680 μs; 6 ms]
4	[750 MΩ; 50 GΩ]	100 V/V	0.35 pF	[10.5 μs; 700 μs]

Table 3.6: Comparison to state of the art resistance to frequency interfaces.

Param	[78]	[80]	[81]	[83]	[85]	[82]	[86]	This work
Range (Ω)	[1k; 1G]	[1k; 1G]	[1; 500M]	[470k; 100G]	[100k; 10G]	[1; 500M]	[1k; 10G]	[5k; 50G]
Power consumption (mW)	600	15	35	4	150	35	25	5.3
Max. relative error (%)	0.38	0.38	1	1	5	1	5	0.35
Area (mm^2)	2000	0.4	1	0.9	2000	1	100	1
Sampling frequency (Hz)	0.1	100	>10	1	14	100	30	>5
Output type	Time period	Time period	Time period	Time period	Time Period	Time period	Time period	Digital (UART)
Validation	PCB	Integrated	Integrated	Integrated	PCB	Integrated	PCB	Integrated
FOM ($\frac{Pow \cdot T_{conv}}{R_{max} \cdot 2^{ENOB}}$)	23.43	0.00059	0.077	0.00044	0.054	0.0077	0.0041	0.000083 (5x)

Table 3.7: Transistor size of the power-consumption optimized OA.

Instance Name	M1	M2	M3	M4	M5	M6	M7	M8	M9	M10	M11	M12
<i>W/L</i> (μm)	6/8	8/8	8/8	8/8	8/8	4/8	128/8	20/0.5	20/0.5	40/0.5	40/0.5	128/4
Instance Name	M13	M14	M15	M16	M17	M18	M19	M20	M21	M22	M23	M24
<i>W/L</i> (μm)	24/1.5	12/0.75	8/1	16/1	16/0.5	32/1	24/1.5	12/0.75	8/1	16/1	16/0.5	32/1
Instance Name	M25	M26	M27	M28	M29	M30	M31	M32	C_{comp}			
<i>W/L</i> (μm)	1.8/8	2/8	8/8	4/8	8/8	4/8	6/0.4	12/0.4	830fF			

Table 3.8: Main characteristics of the power-consumption optimized OA.

OTA parameted	Post-Pex Values
Voltage Supply	3.3 V
Power Consumption	0.32 mW
GBW	54 MHz
Output Dynamic Range	GND to VDD
Input Dynamic Range	GND to VDD
Open Loop DC Gain	100 dB
Slew-Rate	11.75 V/ μ s
Offset Voltage	400 μ V
Input Noise @1 kHz	250 nV/sqrt(Hz)
Input Noise @0.1 Hz	24 μ V/sqrt(Hz)
Unity Gain Phase Margin	61°
Output Current	60 μ A
Peak Output Current	1 mA
Large Signal Settling Time (1%), $V_{step} = 2V$	200 ns

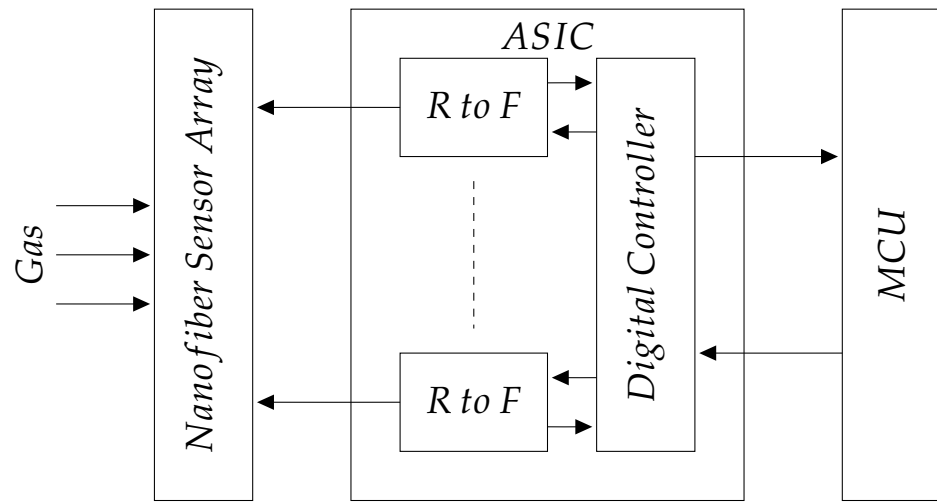


Figure 3.1: System block diagram, annotating the different blocks of the ASIC.

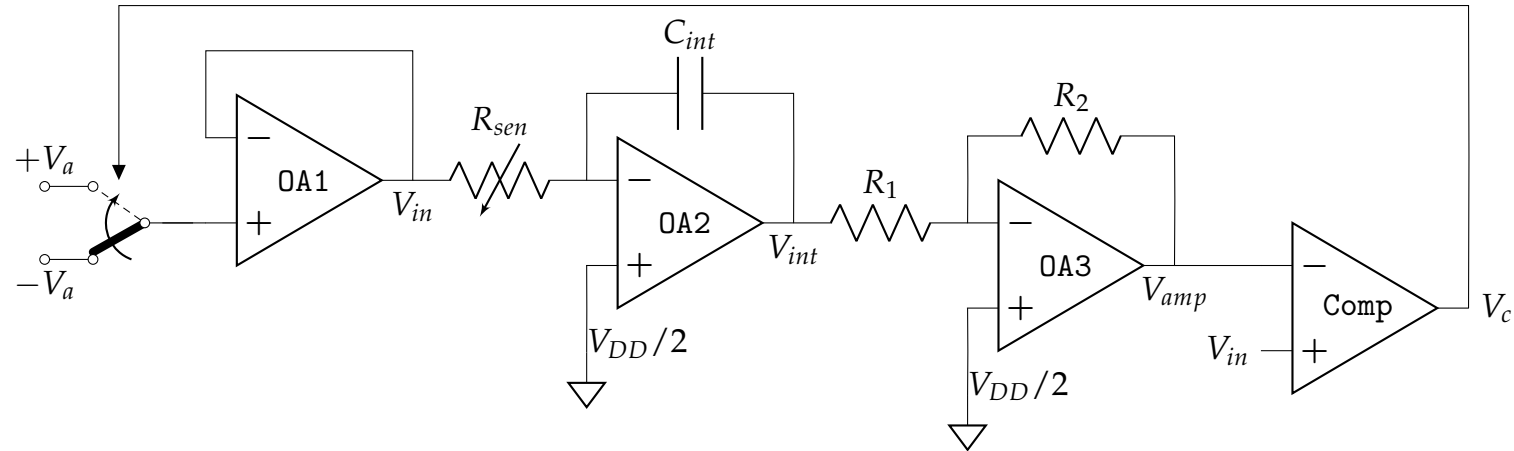


Figure 3.2: Schematic of the resistance-to-frequency circuit.

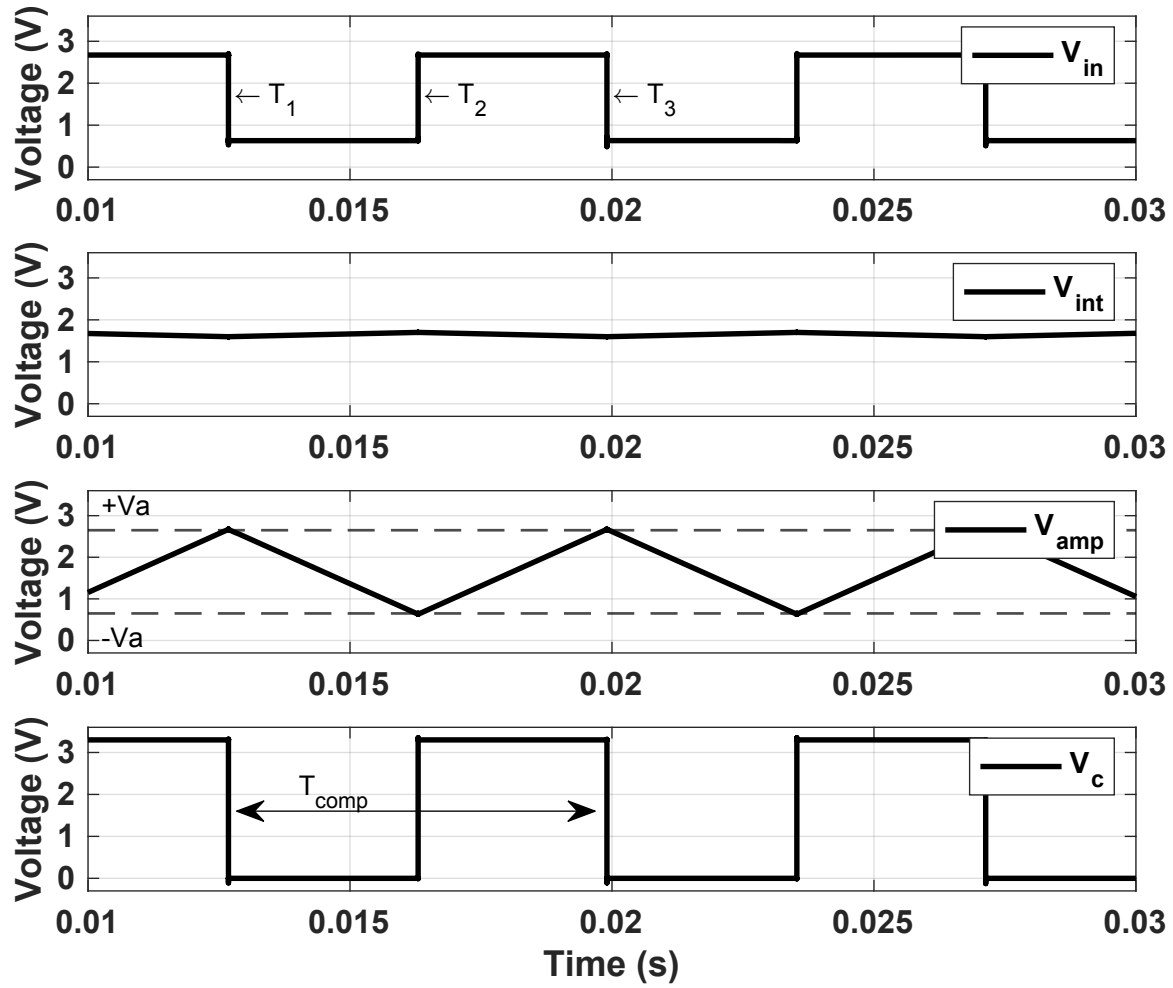


Figure 3.3: Post-pex simulation results of the different voltages using a gain G of 20V/V.

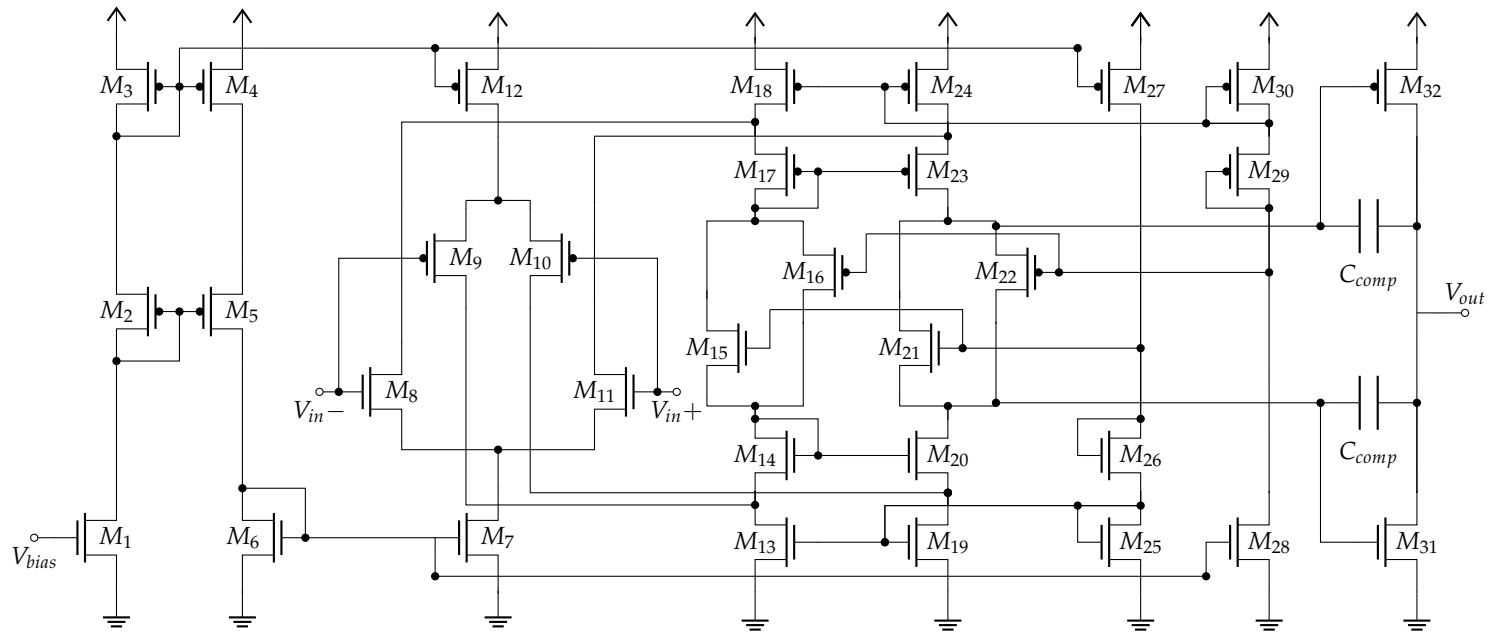


Figure 3.4: Operational amplifier's schematic used for the resistance-to-frequency circuit. The comparator is built around the same schematic, without C_{comp} .

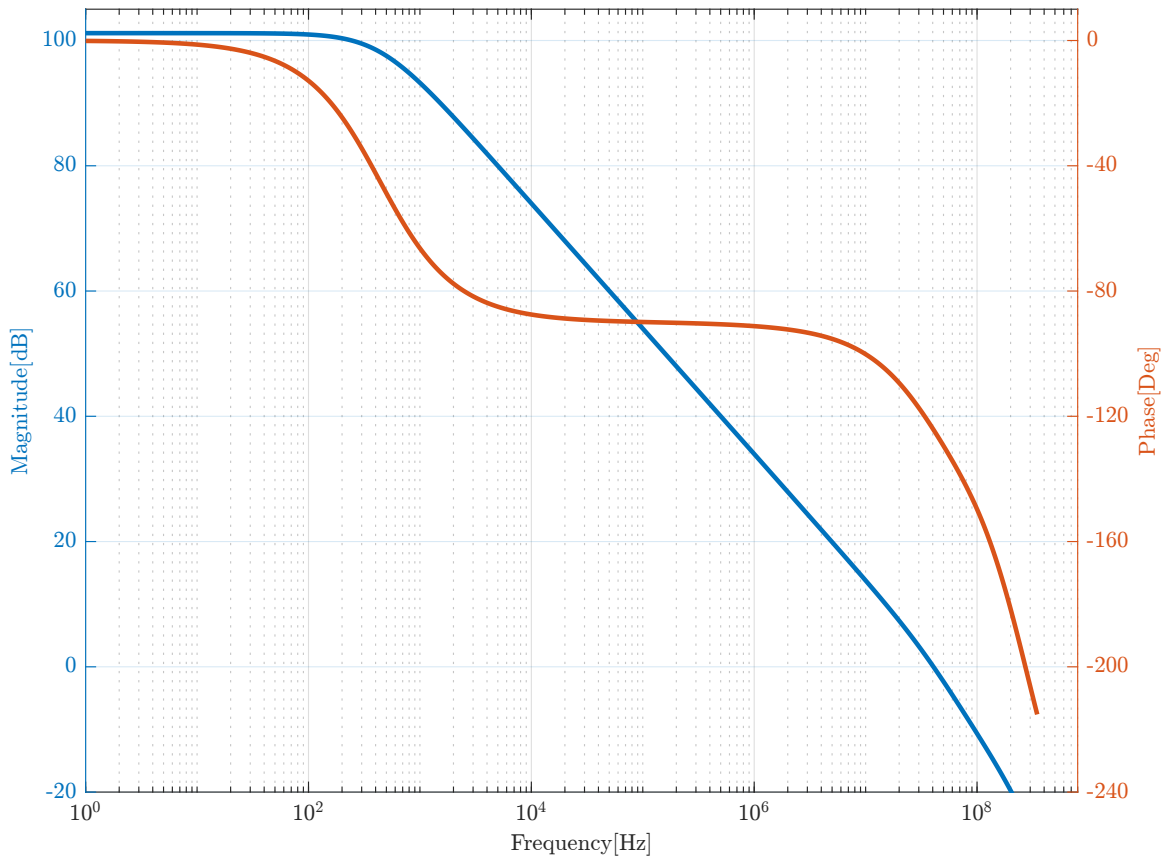


Figure 3.5: Post-pex AC simulation results of the OA.

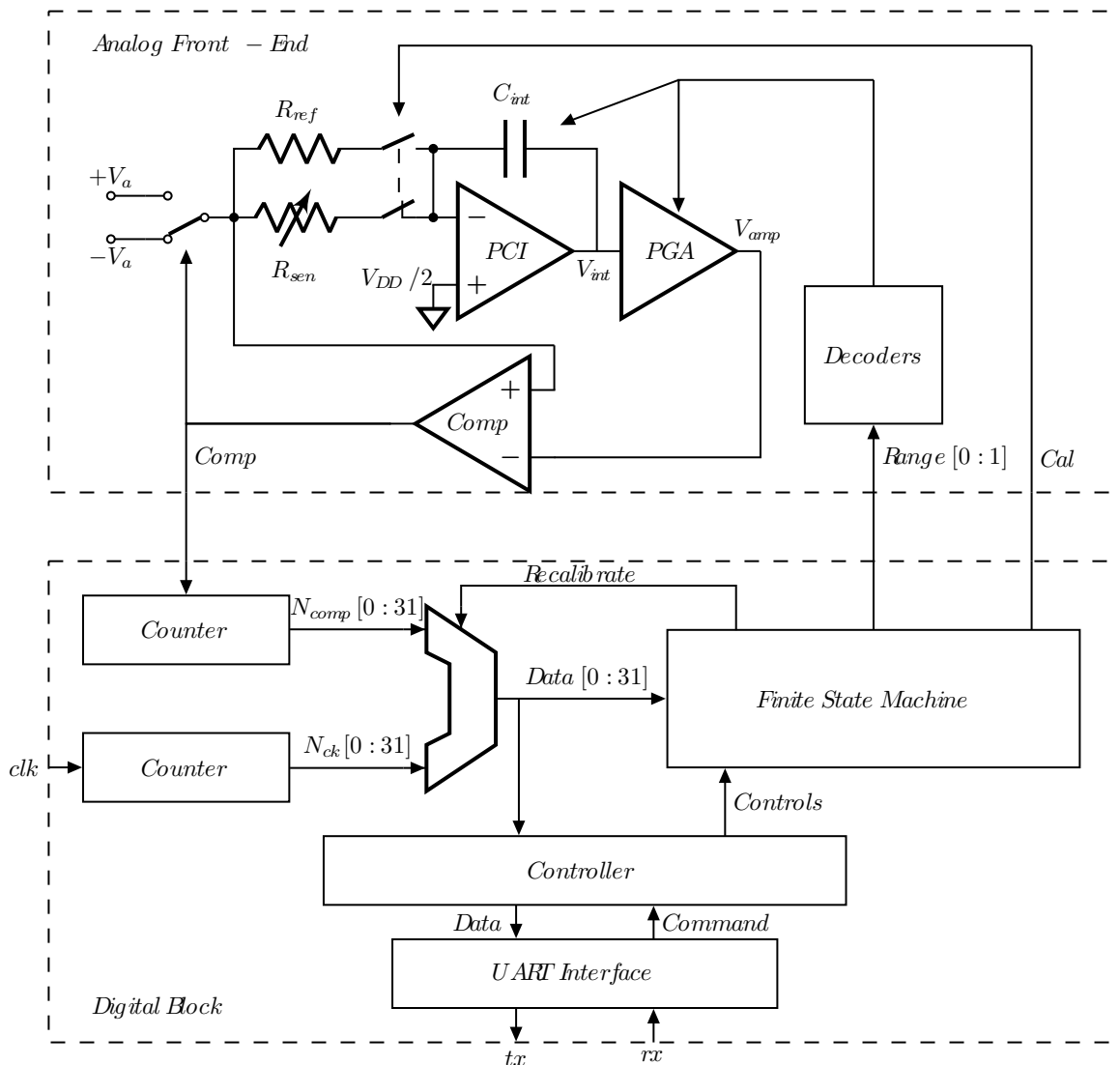


Figure 3.6: Top-level architecture of the mixed-signal ASIC.

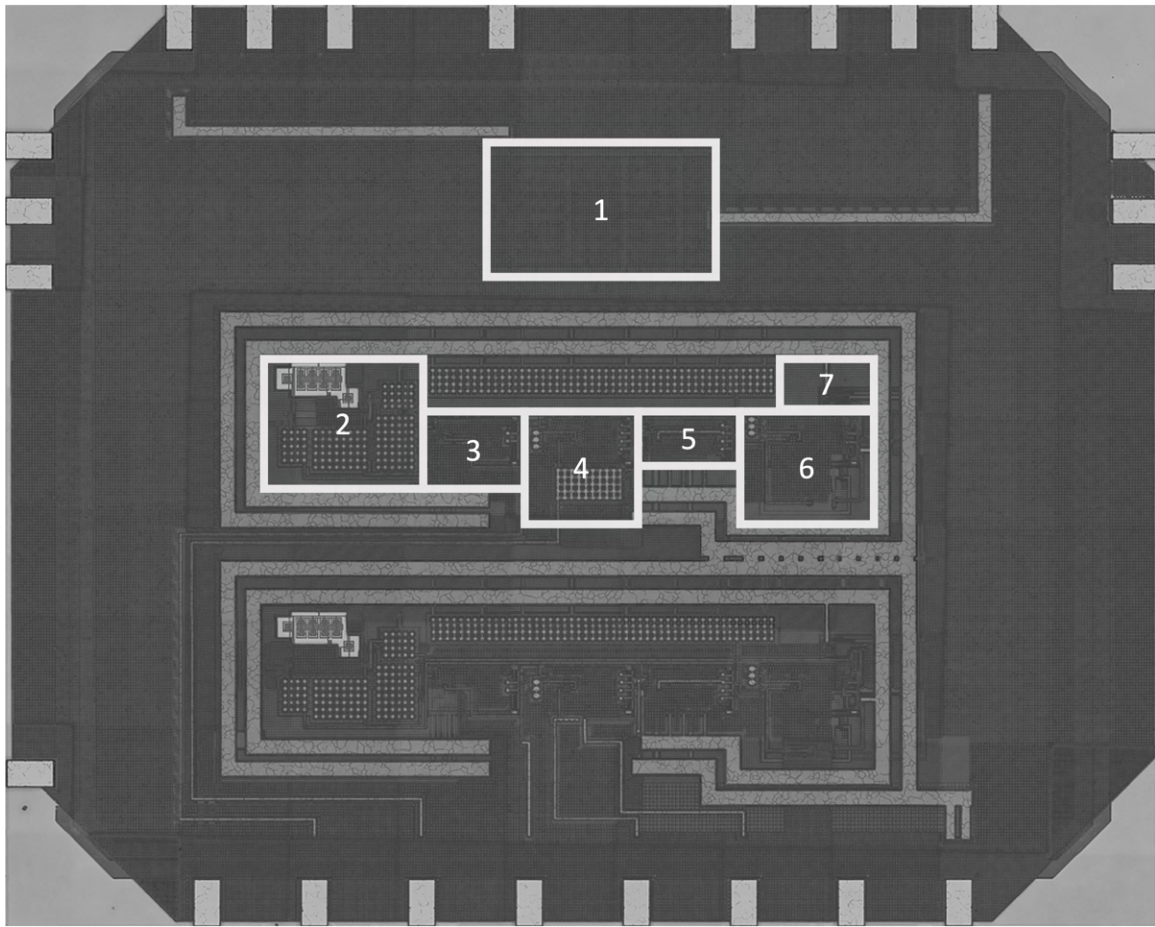


Figure 3.7: Die picture of the fabricated devices with two interfaces. 1: digital controller; 2: reference voltage generator; 3: buffer; 4 and 5: integrator; 6: gain stage; 7: comparator.

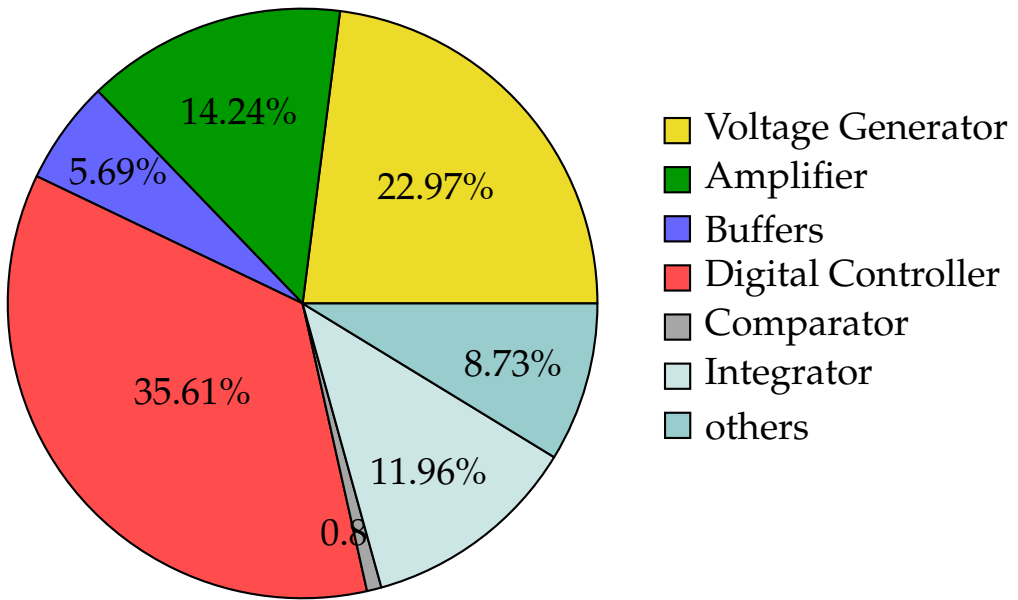


Figure 3.8: Area pie chart of the different ASIC's blocks.

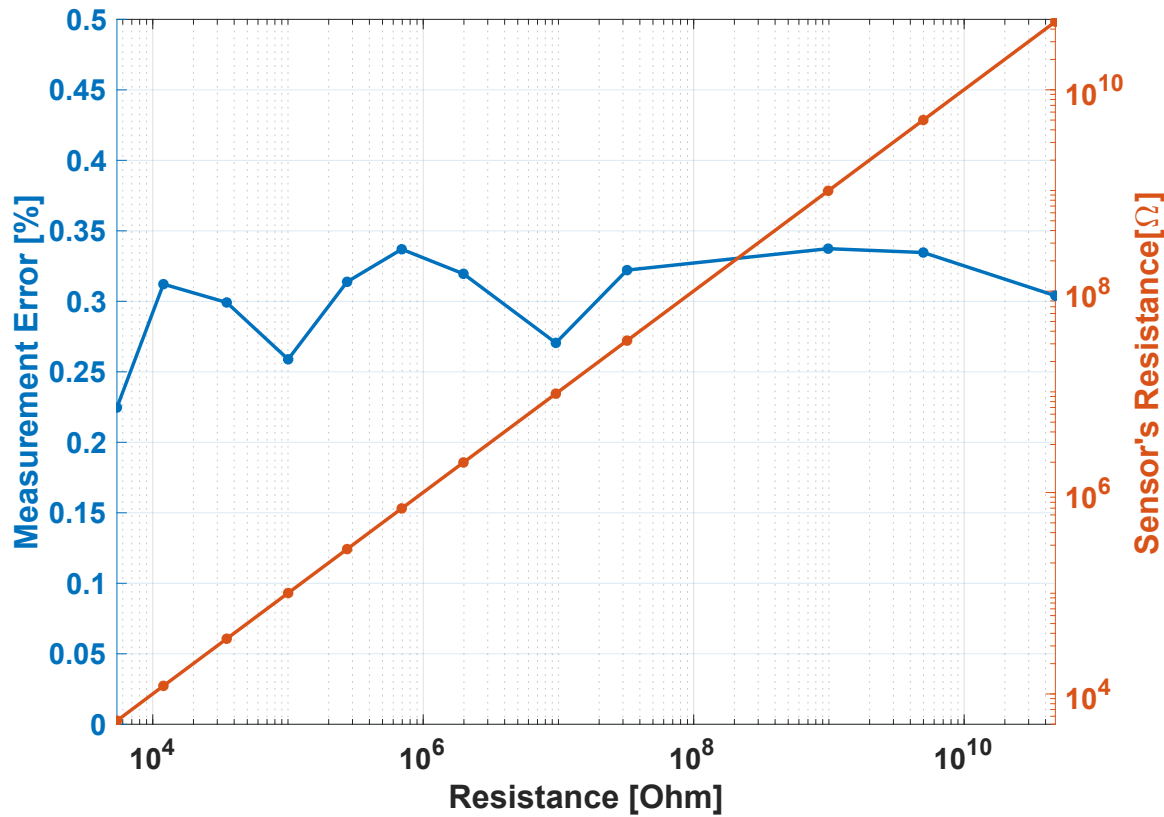


Figure 3.9: Measurement error versus input resistance value.

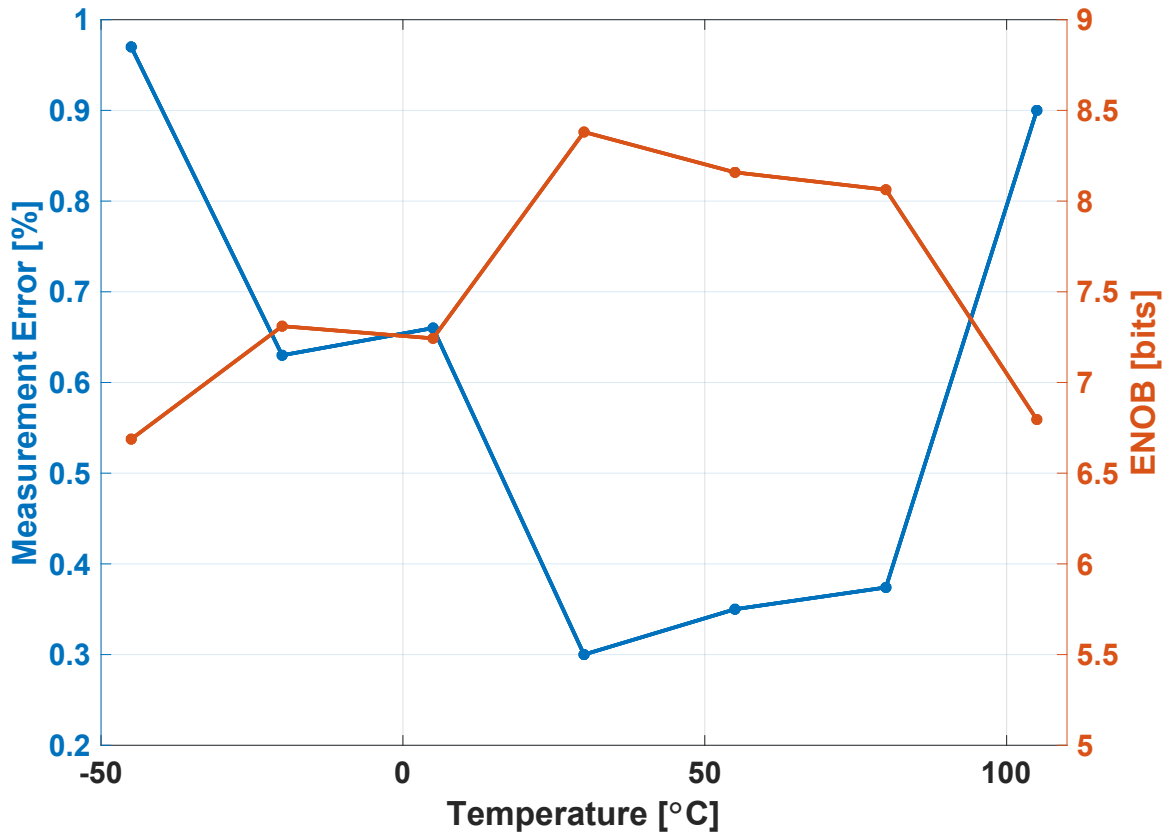


Figure 3.10: Measurement error versus temperature variation for a reference resistor of $100\text{ k}\Omega$.

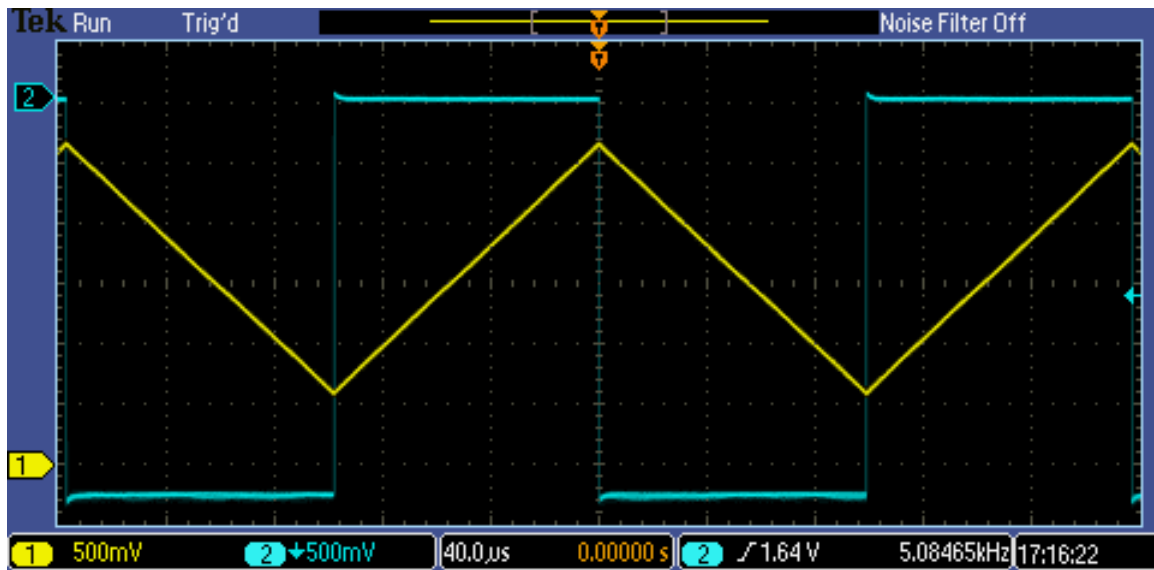


Figure 3.11: Screenshot of the oscilloscope when interfacing a $100\text{ k}\Omega$ resistor at room temperature. Channel 1 (yellow): The gain stage's output voltage V_{amp} . Channel 2 (blue): The comparator's output voltage V_c .

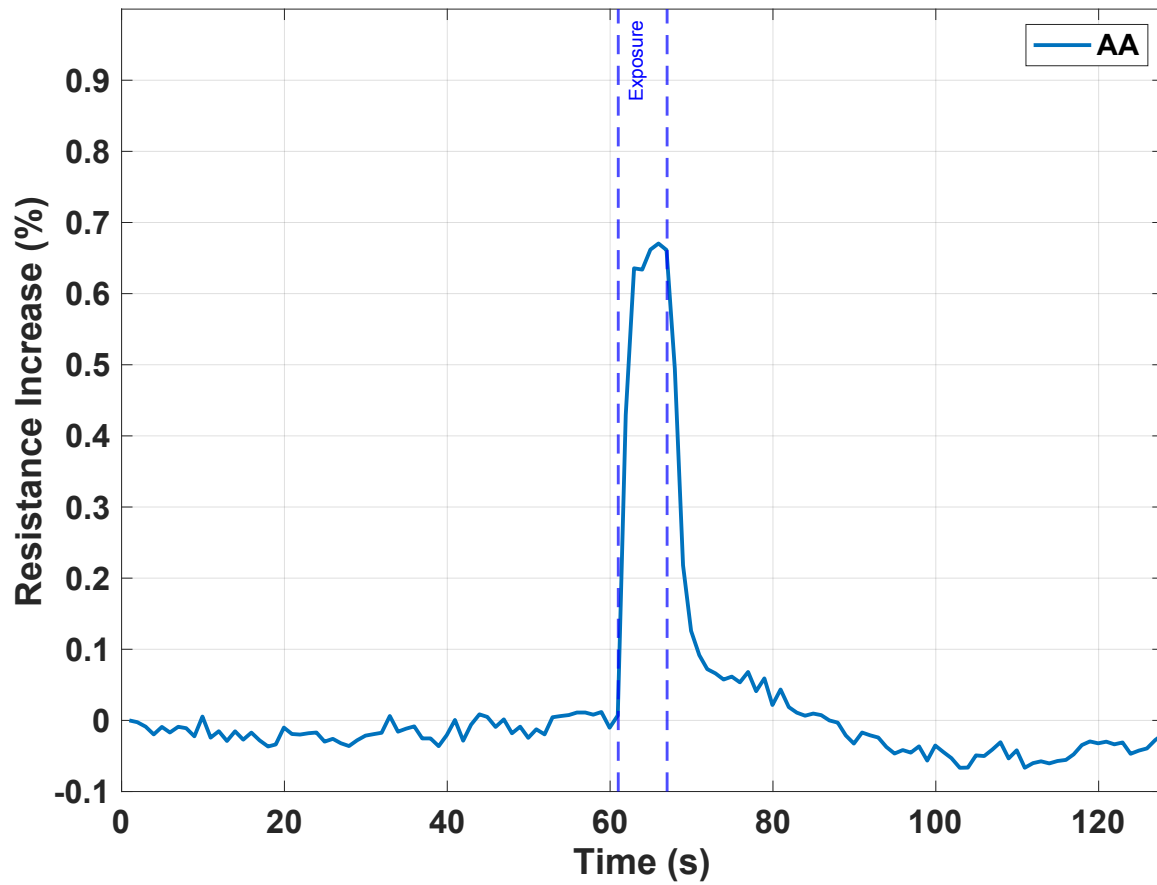


Figure 3.12: Response of an acetic acid nanofiber sensor to a 5 s exposure of acetic acid at 40 ppb.

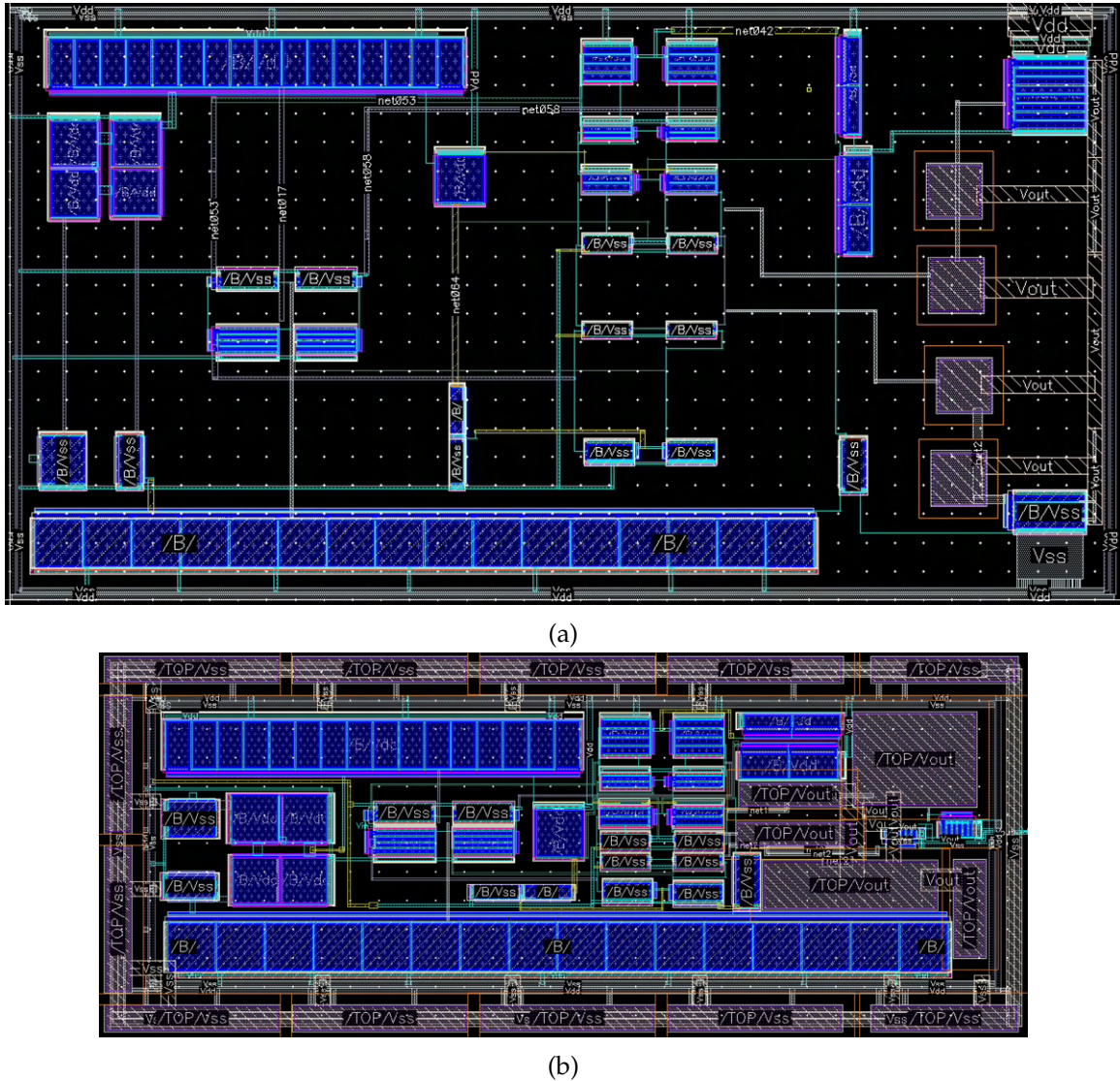


Figure 3.13: Layout comparision of the previous design with the optimized version.
 3.13a: Previous layout of the OA.
 3.13b: Optimized layout of the OA.

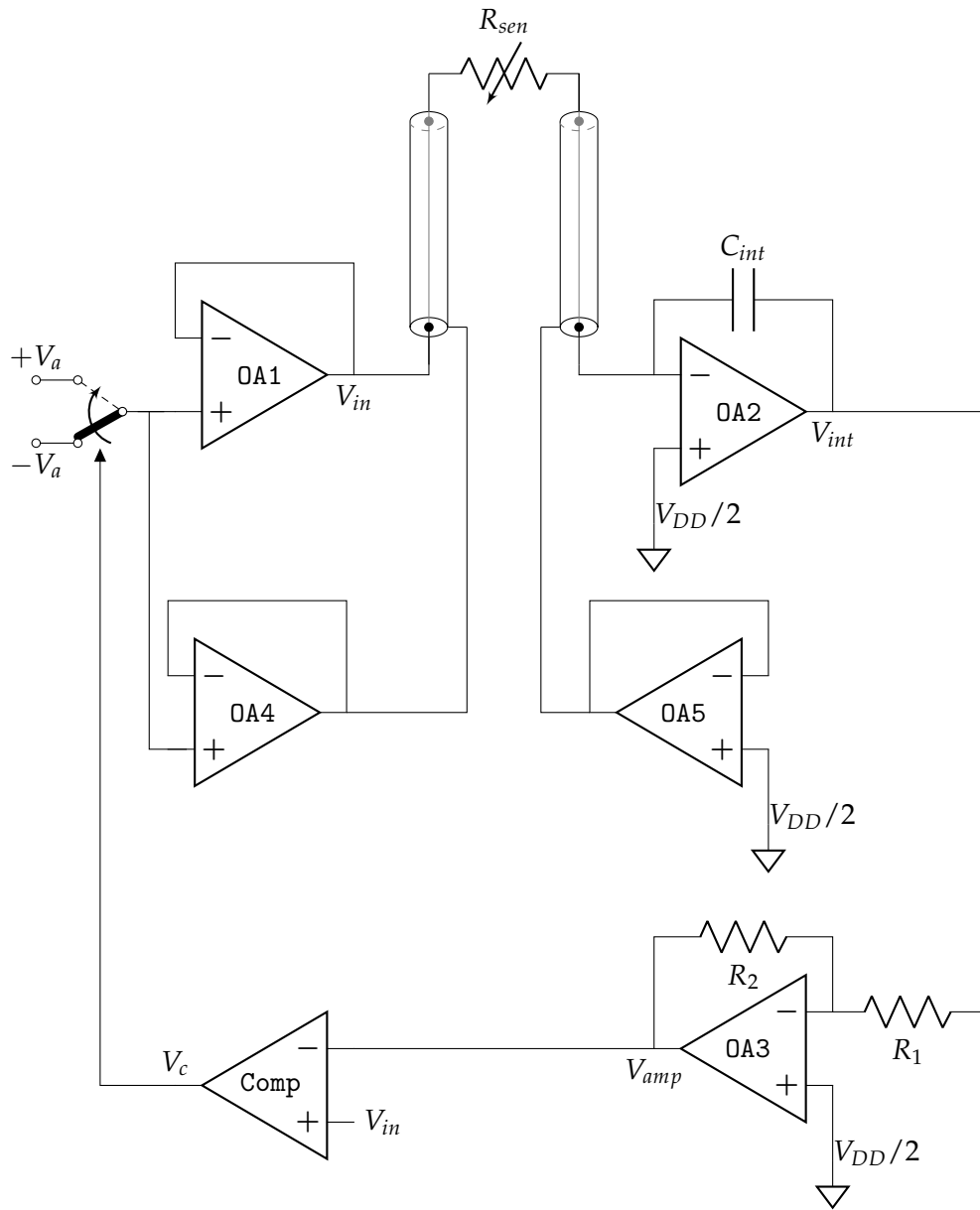


Figure 3.14: Schematic of the optimized resistance-to-frequency circuit.

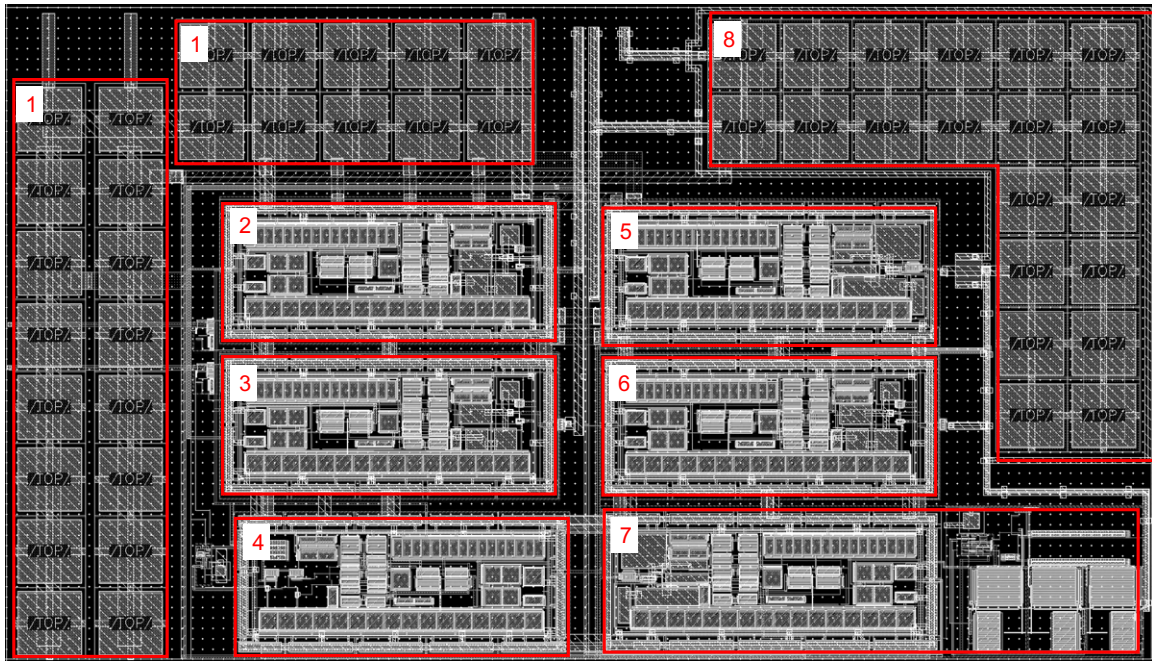


Figure 3.15: R2F's Optimized annotated layout. 1: decoupling capacitors; 2: OA1 input buffer; 3: OA4 shield buffer; 4: comparator; 5: OA2 integrator; 6: OA5 shield buffer; 7: OA3: gain stage

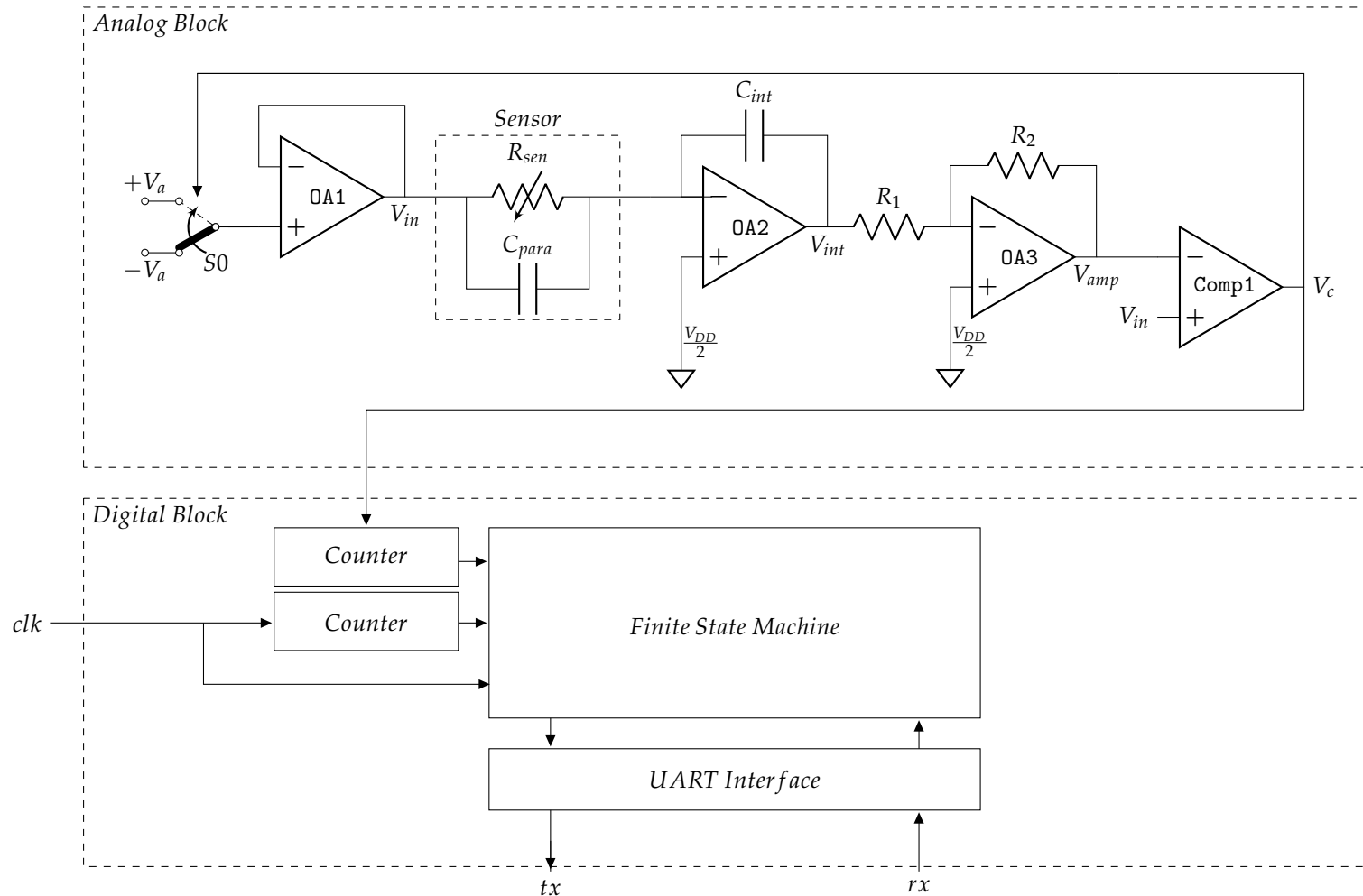


Figure 3.16: Optimized single-channel mixed-signal resistance-to-digital top-level block diagram.

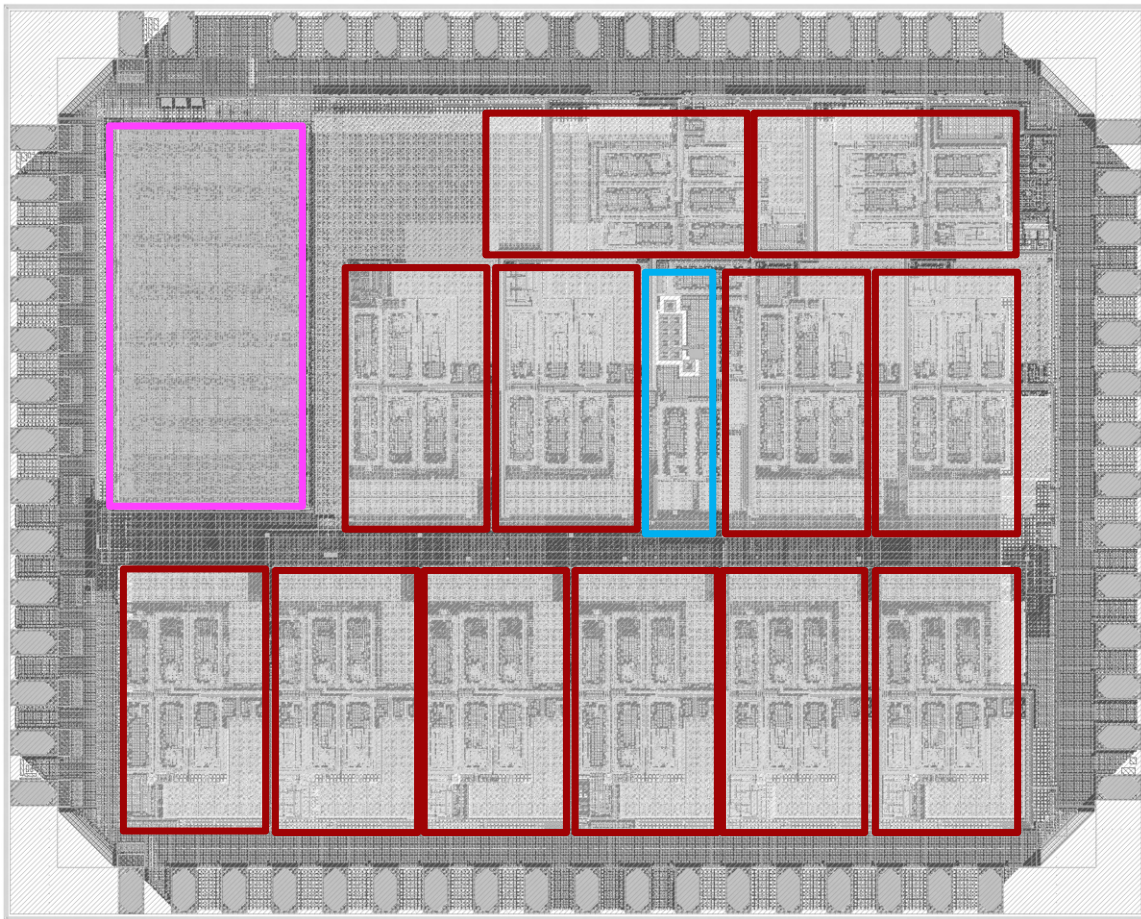


Figure 3.17: Optimized ASIC top-level layout. In red: R2F interfaces; in turquoise: reference voltage generator; in pink: digital controller with the F2D and UART.

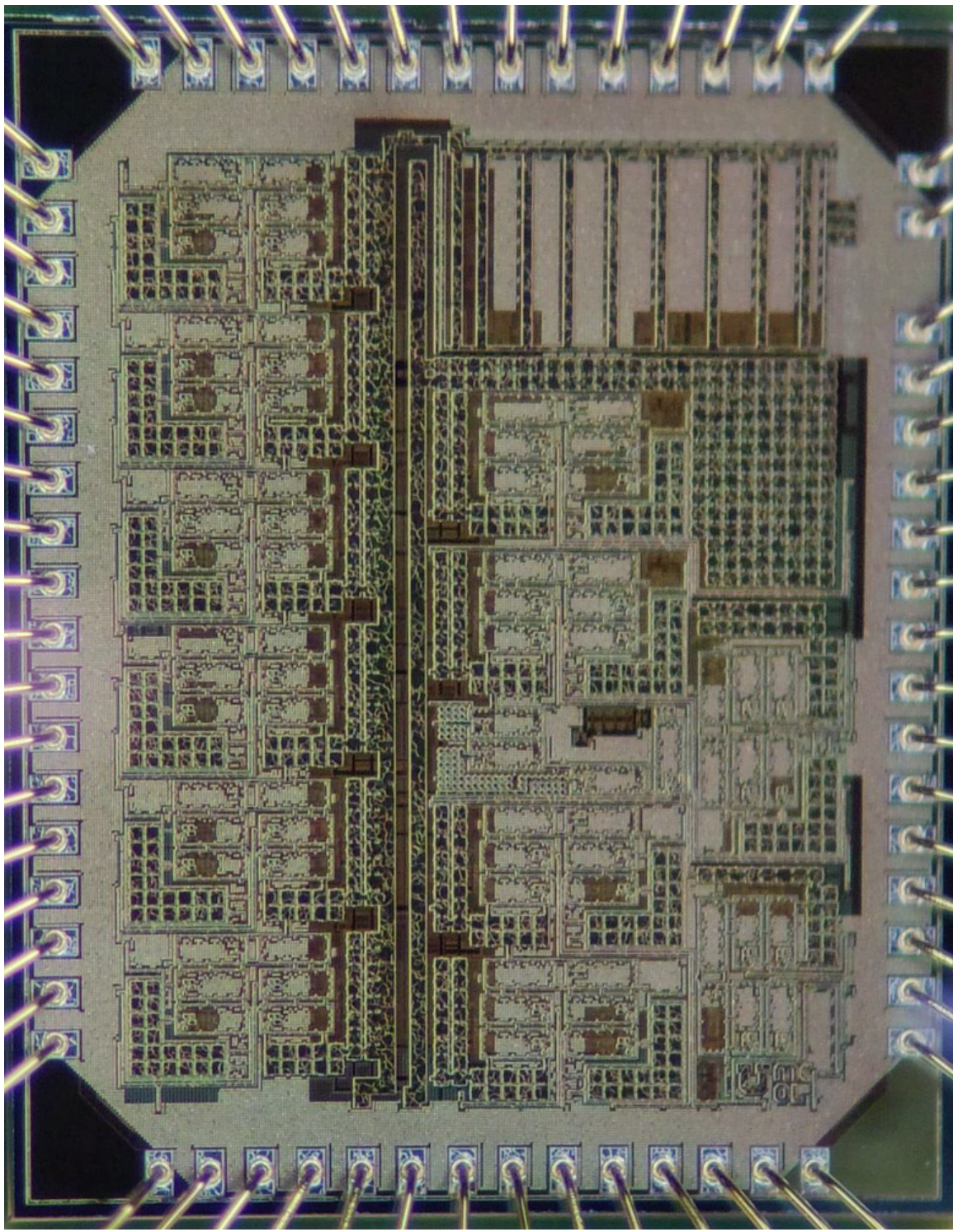


Figure 3.18: Macrophotography of the fabricated ASIC with the corresponding layout in Figure 3.17.

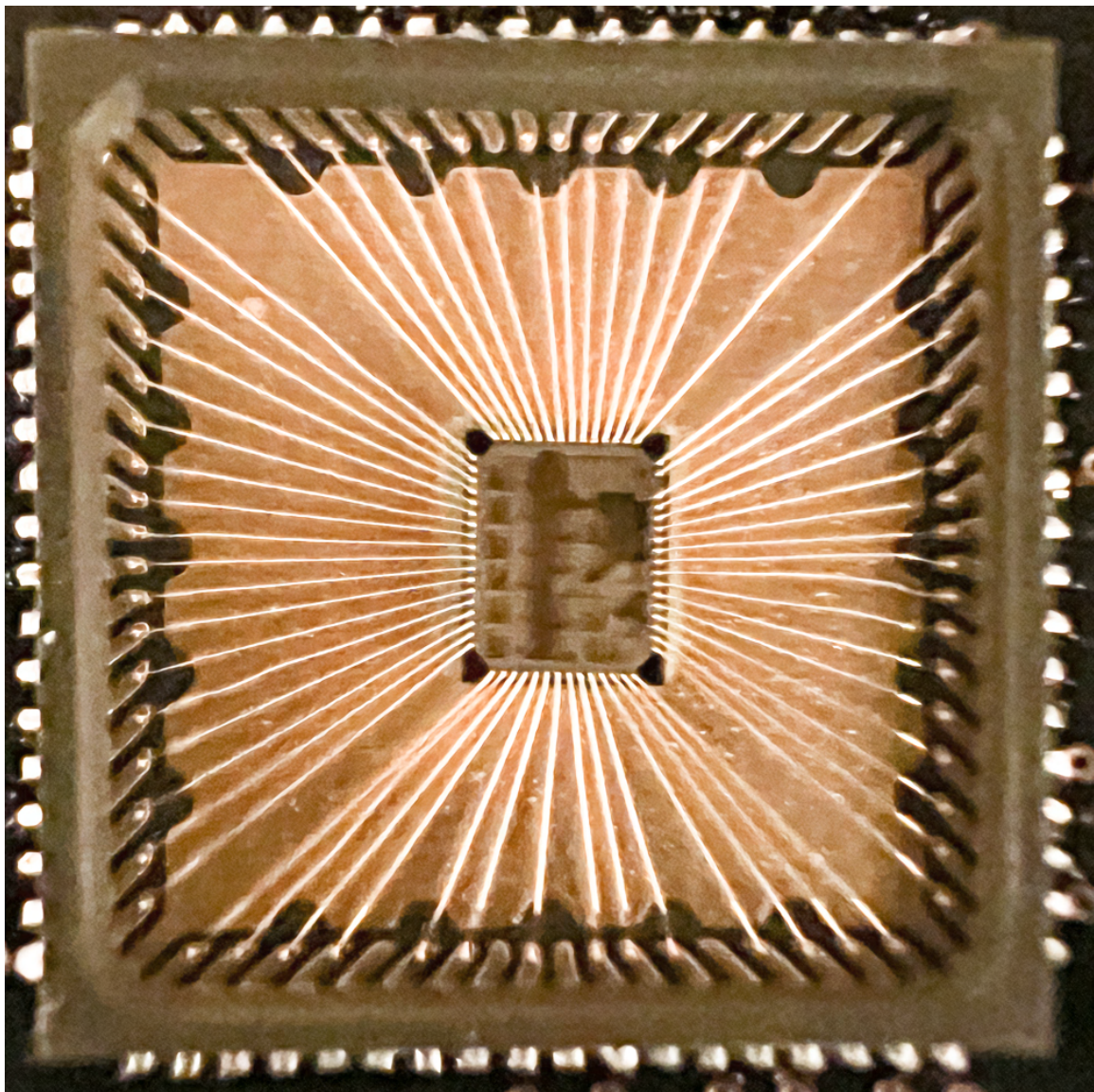


Figure 3.19: Macrophotography of the ASIC packaged in a 10x10 QFN-72.

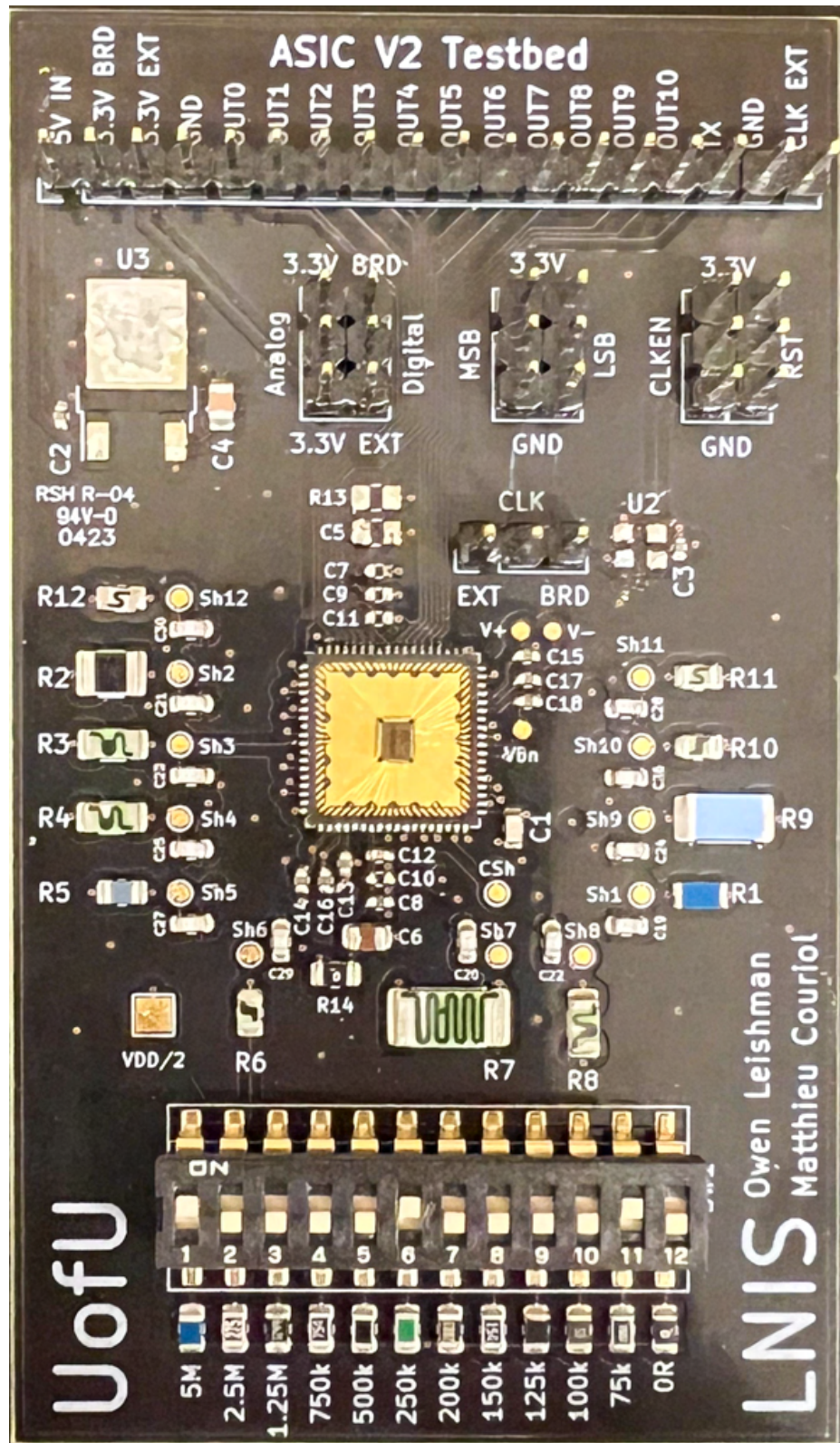


Figure 3.20: Photography of the PCB used to test the ASIC.

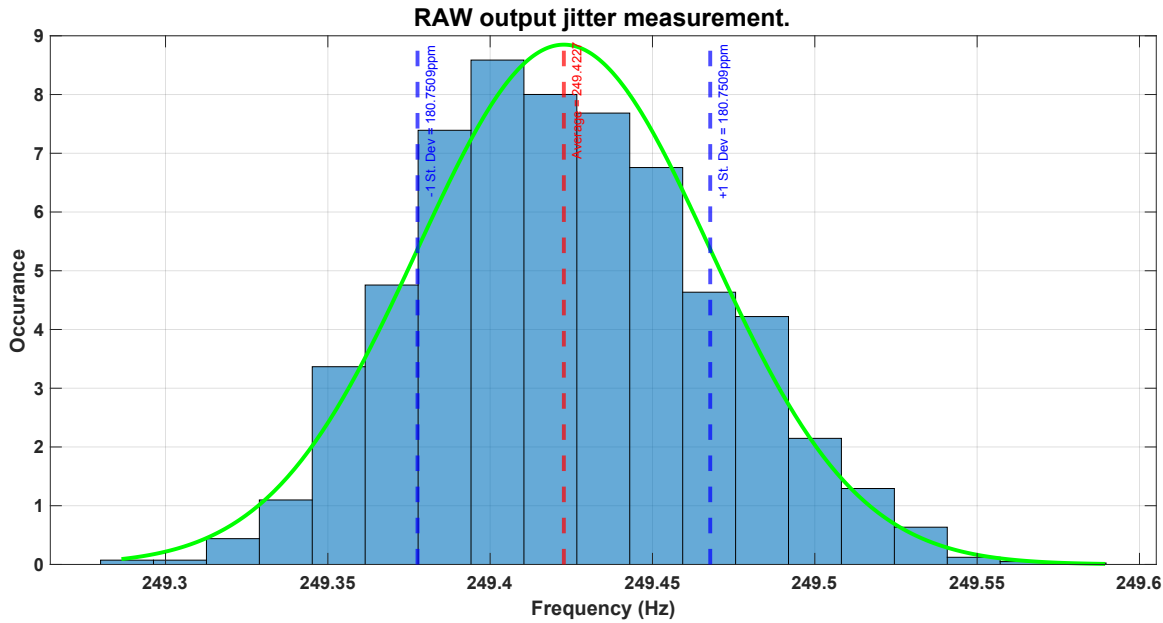


Figure 3.21: Raw histogram of the output measurements of the R2F when interfacing a $10\text{ M}\Omega$ resistor. The histogram is shaped like a gaussian curve due to thermal noise. The standard deviation is 180 ppm .

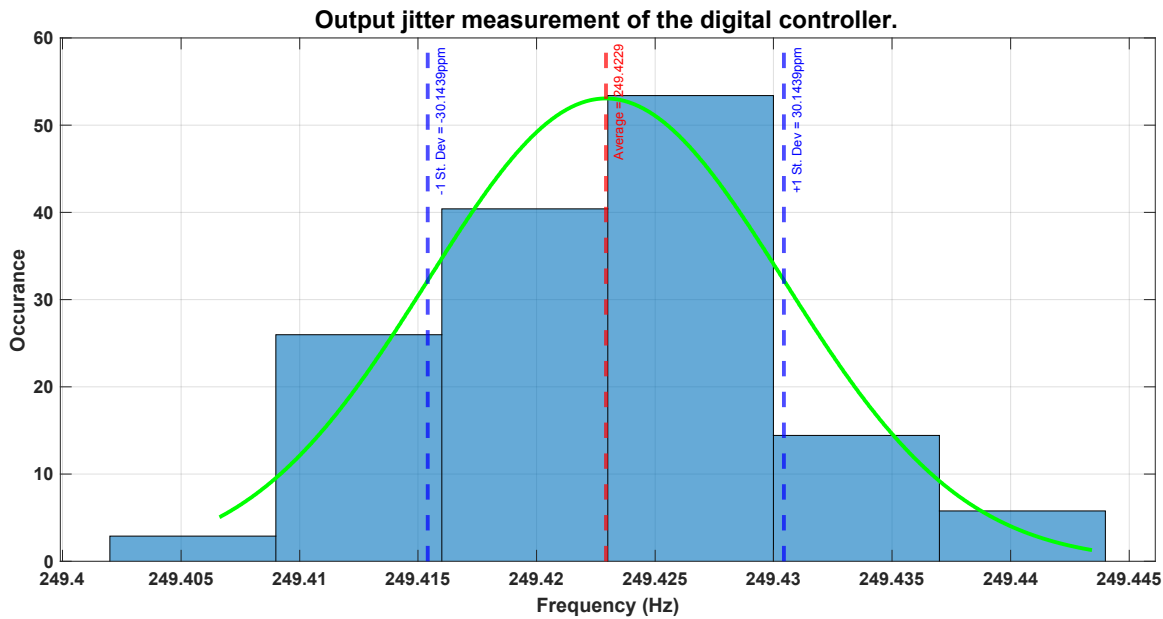


Figure 3.22: Histogram of the output measurements of the R2D (UART output, after averaging of the digital controller) when interfacing a $10\text{ M}\Omega$ resistor. The histogram is shaped like a gaussian curve due to thermal noise. The standard deviation is 30 ppm .

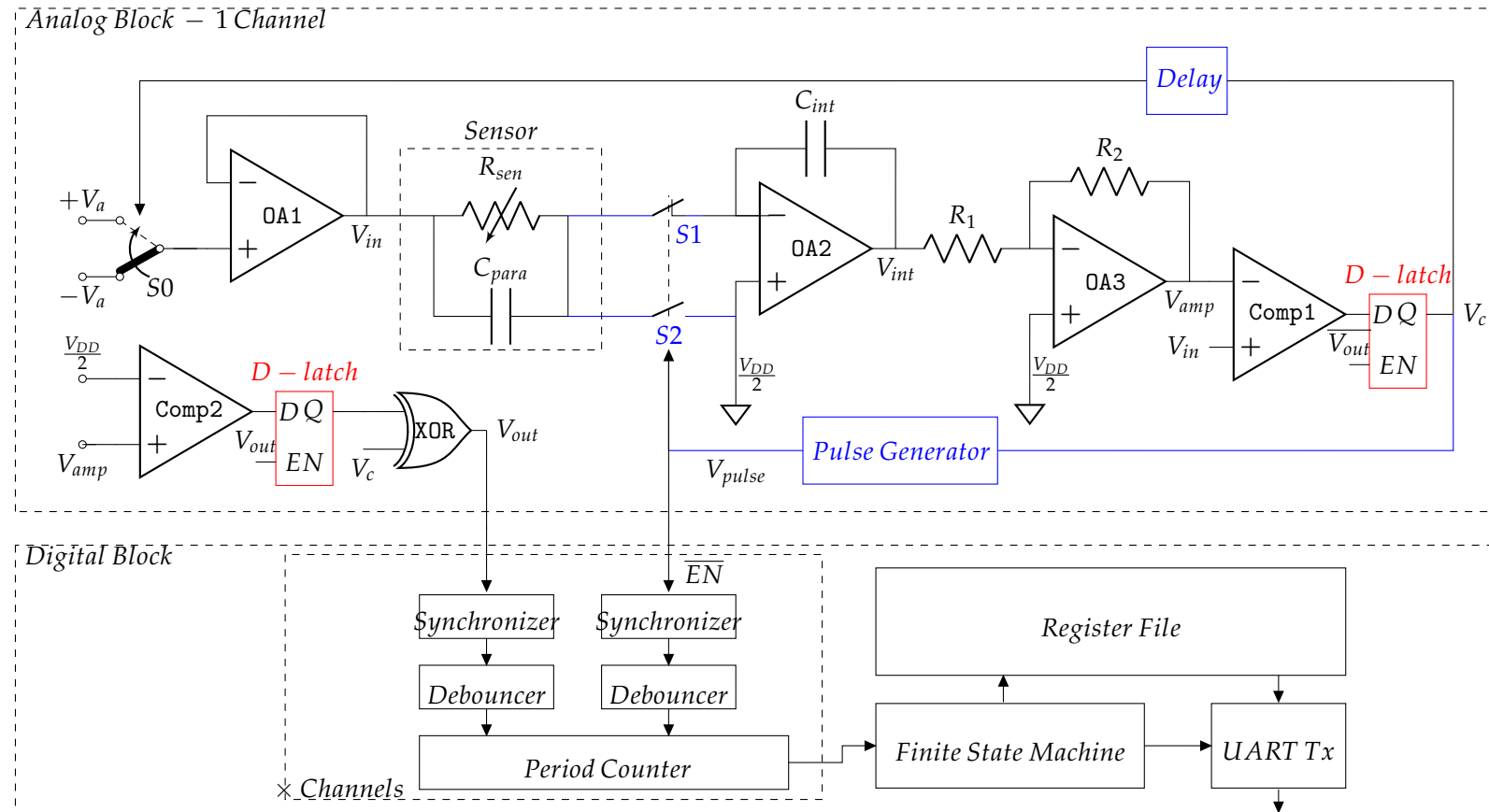


Figure 3.23: Schematic of the analog front-end and digital logic block.

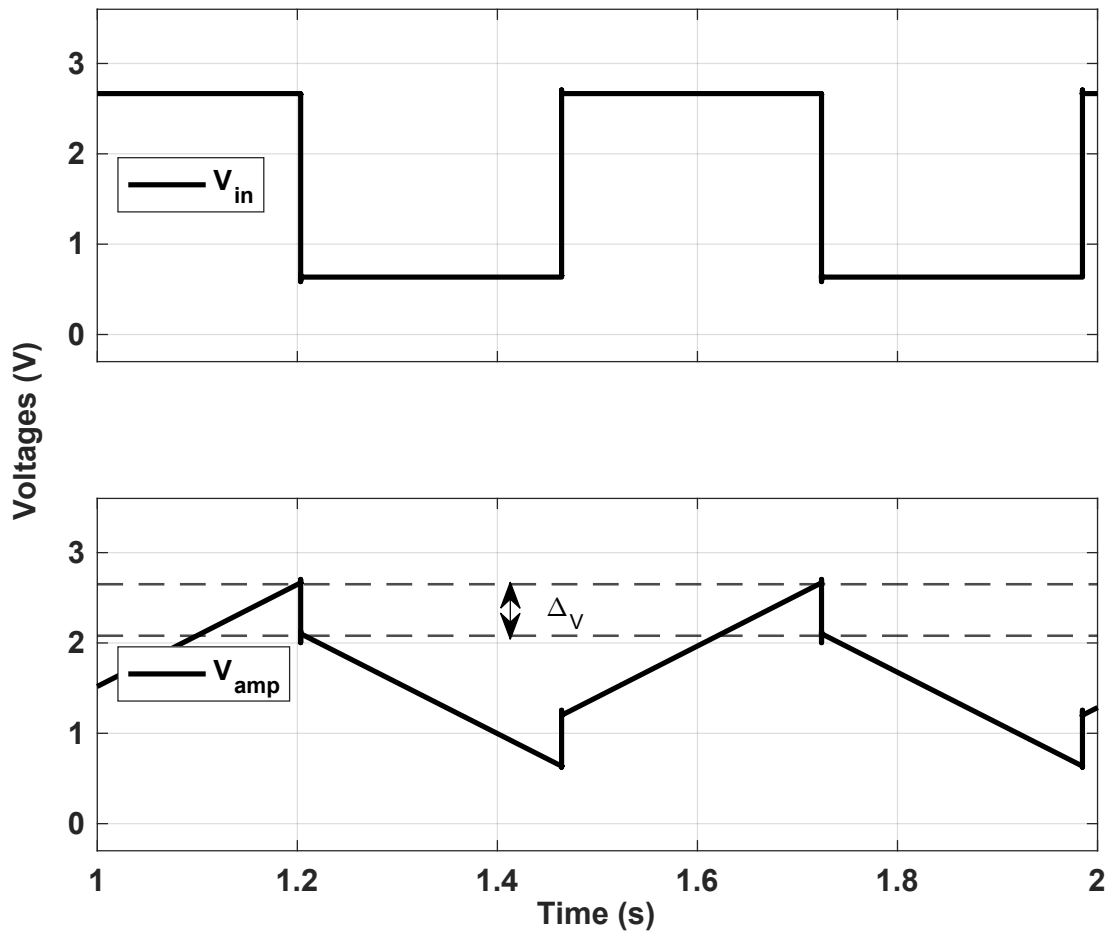


Figure 3.24: Post-pex transient simulation without parasitic mitigation circuitry.

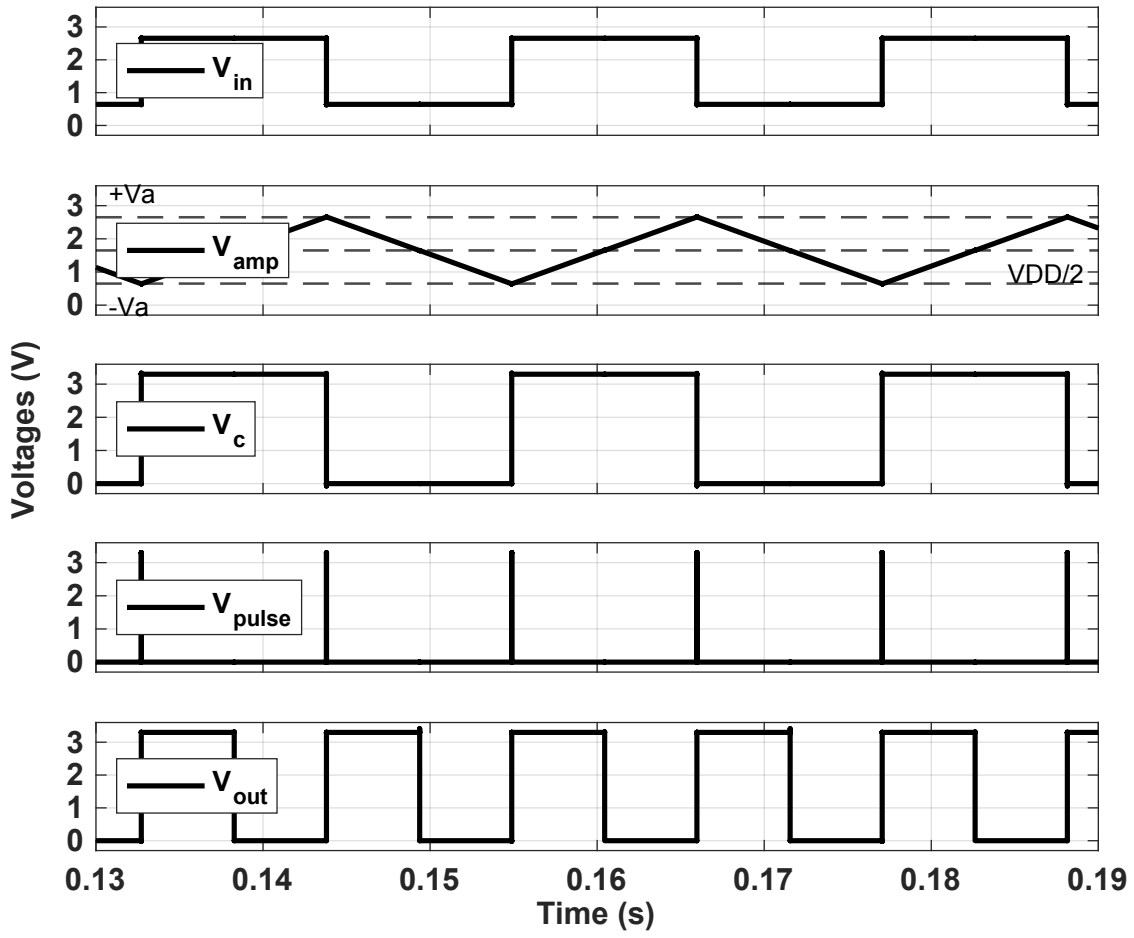


Figure 3.25: Post-pex transient simulation of $R_{sen} = 10G\Omega$ and $C_{para} = 5pF$ with parasitic mitigation circuitry.

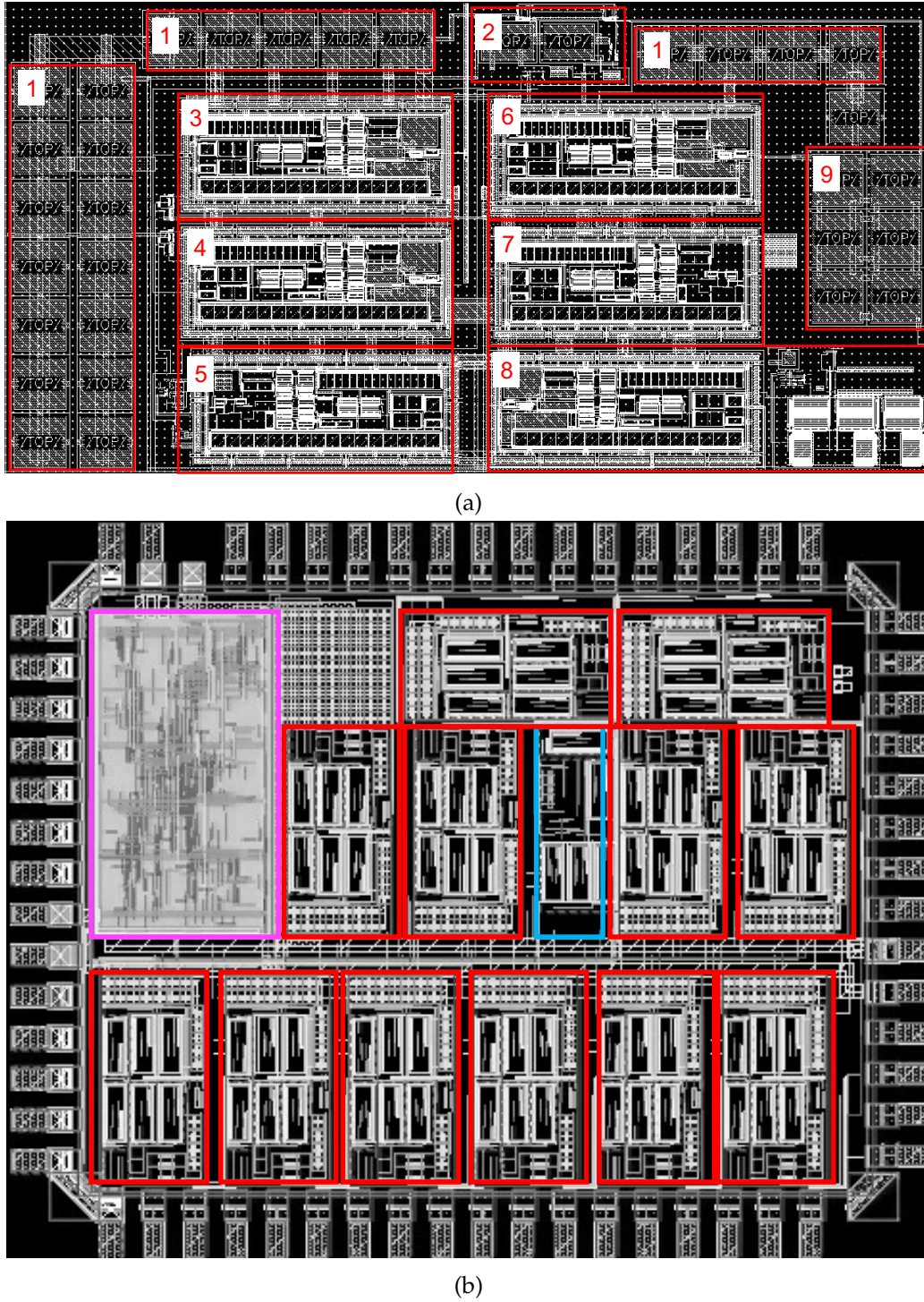


Figure 3.26: Layouts of the ASIC and analog front-end of the R2D with parasitic mitigation circuitry.

3.26a: Annotated layout of the analog front-end. 1: Decoupling capacitors; 2: Mitigation circuit; 3: OA1; 4: Buffer for shielding the sensor line; 5: Comp1; 6: OA2; 7: Comp2; 8: OA3; 9: Integration capacitor of 10pF.

3.26b: Annotated layout of the 12 channels ASIC. Magenta: digital controller; Red: analog front-ends; Blue: voltage reference generator.

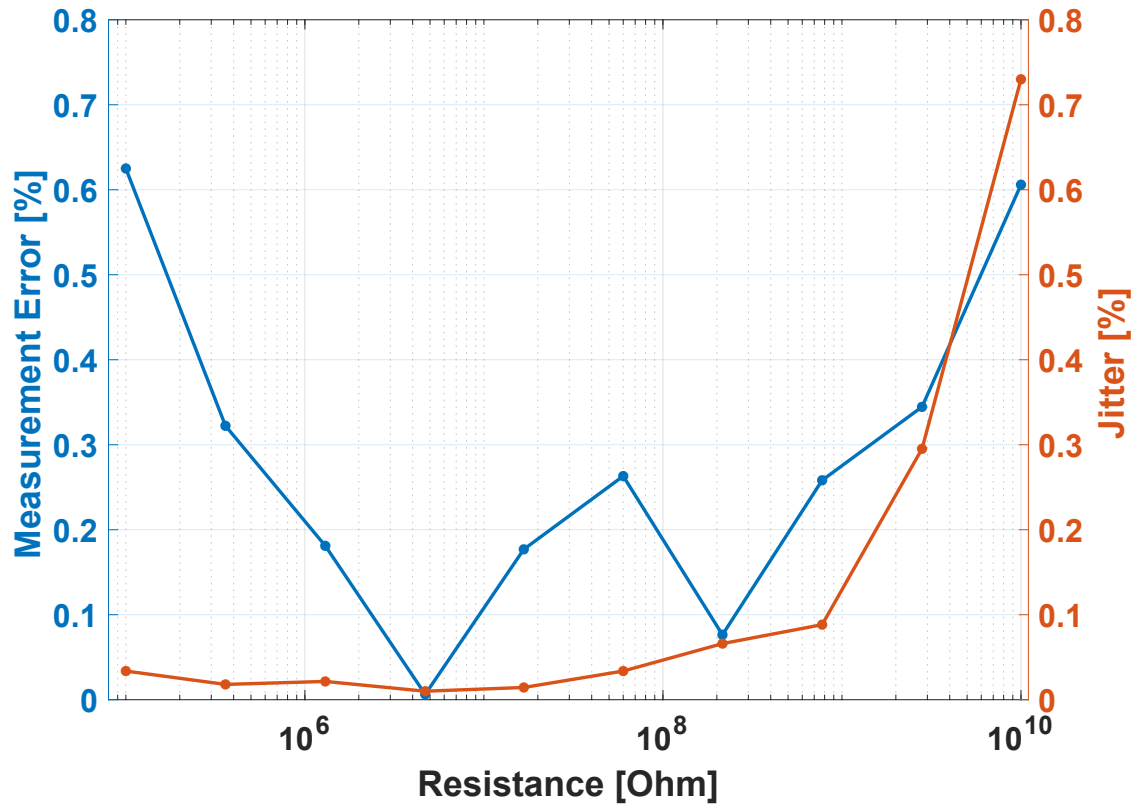


Figure 3.27: Simulated performance results in terms of measurement error and jitter.

CHAPTER 4

CHEMAIRU: A LOW LEVEL OF DETECTION CHEMICAL MONITORING NODE

In Chapter 3, we discussed three different contributions to improve sensor interfaces which can be used to monitor nanofiber sensors and thus monitor chemicals in the air. This chapter introduces two novel contributions about chemical monitoring systems using nanofiber sensors and our previously designed ASIC (Chapter 3). This chapter focuses on the system integration of the sensors and the ASIC within the same system. We first provide a quick background summary based on the materials from Chapter 2. This chapter discusses the system performance (size, weight, cost, and power) of the chemical monitoring platform that we manufactured with qualitative chemical detection capabilities. The chapter then provides quantitative chemical detection capabilities based on real-life scenarios using nanofiber sensors and our designed interface. This chapter is built around two novel contributions: A low SWaP and low-cost platform for multi-chemical sensing that can be connected to the AirU network in Section 4.2, and a low-level of detection platform for the detection of acetic acid in human breath in Section 4.3. Finally, Section 4.4 summarizes the contributions on chemical monitoring platforms designed during this dissertation.

4.1 Background on ChemAirU's Building Blocks

To create a new system to supplement existing ESNs, we first explored existing solutions, as well as the underlying principles of how the sensors we use work to determine how to effectively interface them.

4.1.1 Currently Largely Deployed ESN Limitations

Section 2.1 provides a deep comparision of ESN networks and different ESN node designs. This secton briefly summarizes the results in the context of deploying our chemical

monitoring ESN.

To integrate with and expand the capabilities of existing ESNs we need to understand their basic workings and capabilities. We explored some of the most recent widely deployed ESNs in an effort to determine how our system could be incorporated.

While BEACO2N and AoT systems consume watts, most stay within the milliwatt range. Effective chemical monitoring integration mandates low power demands, aligning with efficient ESNs without affecting energy sources. The AoT's 3-inch diameter limit sets the chemical system's size. Large ESNs employ central MCUs with industrial serial capabilities. Table 2.1 summarizes ESN network comparisons and their technical implementations.

4.1.2 Nanofiber Gas Sensor Requirements

The behavior of the nanofibers and their requirements in term of biasing are discussed in Section 2.2. This paragraph summarizes the main requirements of the sensors.

Nanofiber sensors outperform other sensing mechanisms in terms of factors like response and recovery time, power consumption, selectivity, and sensitivity [71–73]. Nanofibers can detect sub-ppb levels with only a 0.3% variation in sensor conductivity at room temperature, eliminating the need for an external heater [67]. To fully realize the benefits of these new sensor technologies, a specialized electrical interface is needed to measure them, and LED biasing is required to improve their chemical response. We therefore developed the interface discussed in Section 4.2.2.3 and the LED biasing in Section 4.2.2.4.

4.1.3 Sensor Interfaces Limitations

Prior wide-range resistive sensor interfaces based on relaxation oscillators have encountered several limitations. One notable constraint is the limited sampling frequency capability, typically restricted to around 1Hz in prior works [97, 98]. This limitation hampers the real-time responsiveness and the ability to capture rapid changes in the sensor's resistance accurately.

Additionally, the integrated circuit implementations of relaxation oscillators in prior works have predominantly featured the resistance to frequency conversion circuit only [83]. While this approach simplifies the circuit design, it introduces the need for an external PLD or FPGA to digitize the frequency output [83]. This reliance on external components

imposes significant drawbacks, including increased costs, elevated power consumption, and enhanced complexity of the overall system.

The necessity for an external PLD or FPGA not only escalates the expenses associated with the interface but also complicates the integration process. Such complexity may lead to challenges in system design and development, making it less accessible for applications with stringent cost and resource constraints such as ESN.

Moreover, the additional power consumption induced by the external digitization components can be detrimental for energy-efficient and battery-operated systems. The increased power requirements may adversely impact the overall power budget of the application, limiting its practicality and performance.

4.2 A Low SWaP, Low-Cost, Multi-Chemical Monitoring System

4.2.1 Designing a Low-SWaP ESN Node

This contribution presents a novel device to address the need for efficient and broad spectrum air quality monitoring [99]. We propose a proof-of-concept device tailored for chemical monitoring applications, characterized by its low SWaP requirements. This device not only functions autonomously but can also be seamlessly integrated into existing monitoring stations, enhancing their capabilities. While acknowledging the scope limitations of large-scale and long-term chemical recording, this study provides valuable insights through laboratory exposure experiments which yield chemical identification results.

The primary objective of this contribution is to introduce an economically viable solution to chemical monitoring that is affordable (chemical sensing front-end costing only \$15) with a compact form factor (less than 2 cubic inches) and lightweight design (15 grams). This device supports up to 12 nanofiber sensors while operating at a power consumption of only 52 mW. The demonstrated chemical identification accuracy of the system exceeds 90% showcasing the potential utility of this technology in real-world scenarios.

4.2.2 The Proposed ESN Node with Chemical Sensors

This section discusses the design and architecture of the proposed chemical monitoring system, called miniChemAirU. This system can perform chemical monitoring (with up to

12 sensors) as a standalone system with integrated fan and MCU with WiFi and it can also be part of an already deployed ESN node and act as an expansion module to increase chemical selectivity. In this configuration, the fan, the MCU, and WiFi capabilities from the existing node are used.

4.2.2.1 The Proposed Chemical Monitoring System

The proposed system is broken up into two main sub-systems, called the front-end sub-system and the standalone sub-system to give greater deployment flexibility. The front-end sub-system includes all of the basic circuitry needed to interface with the nanofiber sensors and output the readings to an external MCU as shown in Figure 4.1. This front-end sub-system can easily be integrated into existing ESNs due to its small form factor, cost, and power requirements. The standalone sub-system provides the remaining functionality needed for the system to be its own ESN, including a MCU for data processing and transmission as well as a fan to increase airflow to the sensors.

The front-end sub-system comprises of three integral blocks: nanofibers, LEDs, and a data acquisition ASIC. The nanofiber sensors function as resistive sensors, necessitating a resistance-to-digital interface (the ASIC) and LED biasing for proper functioning. To optimize efficiency and cost-effectiveness, we have independently developed our ASIC, capable of real-time interfacing with up to 12 sensors and incorporating a UART interface. LED biasing is pivotal to energize the sensor's organic layer and enhance conductivity. The system's output is the sensor array's value transmitted over UART. Each sensor generates a 40-bit output every 100 milliseconds. Each UART packet consists of 72 Bytes, achieving a transmission speed of 720 Bytes per second.

These three foundational blocks constitute the system's front-end and are individually detailed in Sections 4.2.2.3 and 4.2.2.4. These blocks can either integrate into an AirU node (explained in Section 4.2.2.2) or operate as standalone chemical monitoring devices when equipped with a built-in MCU and fan.

The standalone sub-system adds a low power ESP32-s2 Mini MCU which enables the system to transmit data using the UDP network protocol over WiFi as illustrated in Figure 4.1. The MCU also allows for finer control of the LEDs by controlling the LED driver, allowing for individual control of each LED. The standalone system additionally interfaces

with a temperature and humidity sensor that can optionally be placed on the front-end system, which is not required when being used with an ESN that already includes one.

4.2.2.2 AirU as a Test Bed for Our System

The AirU was selected as our test bed because of its ongoing development, and widespread deployment. The AirU ESN [77] has a solid base array of sensors including PM, CO, NO, temperature, and relative humidity, along with a battery-backed real-time clock (RTC) and GPS module. The AirU network also features all the cloud infrastructure, using MQTT requests and local SD card when cellular is down. Additionally the AirU cloud provides calibrations and Gaussian process regression [100, 101] at the network level. These features provide a solid foundation for our platform to build upon.

The included onboard storage enhances the stability of the AirU system and greatly simplifies data collection, as the local storage enables the device to autonomously record a full year's worth of data without any internet connection.

The AirU system has been deployed since 2018 throughout the United States and France. Its initial deployment from November 2018 to April 2019 consisted of 50 units which were maintained by community members throughout Salt Lake City, Utah, simplifying the deployment by reducing the need for staff to troubleshoot issues with the ESN deployment. This deployment saw good correlation ($R^2 = 0.88$) between the low-cost sensor nodes and the high accuracy air quality monitoring stations already in the city. After this deployment AirU version 2 was developed which changed the microcontroller to a ESP32 and added an onboard USB to UART chip for easy end-user programming making it simple to add new sensors to the device. This subsequent version has been deployed continually since its release in April 2018, and has been commercialized, at the time of publication this version has had 307 deployments. We believe that improving the AirU's with chemical capabilities showcases the potential of our system to integrate into various ESN systems.

4.2.2.3 The Proposed Low-Cost, Low-Power, Sensor Interface

Due to the price and complexity (area, cost) of deploying a discrete electronics resistance-to-digital interface, and the limitations of previous resistance-to-frequency (discussed in Section 4.1.3), we fabricated a fully-integrated relaxation oscillator circuit to accurately

measure variations in the sensor's resistance. The circuit relies on the correlation between the sensor's resistance and the frequency of the R2F circuit. As the resistive sensor experiences changes in its resistance due to environmental factors or external stimuli, it directly influences the frequency of the R2F. This inherent relationship allows us to precisely determine the resistance value by analyzing the corresponding oscillator frequency.

To achieve accurate resistance measurement, we compare the R2F output to a precisely calibrated reference clock. This reference clock acts as a highly reliable time-keeping mechanism, enabling us to measure the frequency of the relaxation oscillator with high precision using only two counters within the same ASIC, as part of the frequency-to-digital (F2D) circuit. Consequently, the frequency data, which directly reflects the sensor's resistance, is digitized to obtain a reliable digital representation.

The digitized frequency from the F2D data is transmitted to a dedicated microcontroller through UART communication protocol. UART's simplicity and dependable data transfer capabilities facilitate smooth and seamless transmission to most microcontrollers.

The fabricated ASIC efficiency relies on combining the R2F, F2D, and UART circuits on the same piece of silicon. Despite its advanced functionality, the interface draws a modest 29 mW of power, ensuring energy efficiency and prolonged system operation. Moreover, with an estimated cost of around \$0.30, the interface proves to be cost-effective, making it an ideal solution for interfacing resistive sensors in a wide range of applications. Overall, our interface can interface up to 12 different nanofibers in parallel in a 10 mm by 10 mm QFN-72 pins package with the analog schematic shown in Figure 4.2.

4.2.2.4 Power Optimization of the Sensor Photonic Biasing

In the context of employing nanofiber sensors, an essential aspect to consider is LED biasing. To optimize the sensor's biasing power requirement and achieve the best operating point, we conducted a comprehensive multi-variable analysis. The objective of this analysis was twofold: first, to maximize the sensor's response, ensuring its sensitivity to the target analytes, and second, to minimize both noise and power consumption for an efficient and reliable sensor system.

The LEDs are controlled using an LED1202 from ST MicroElectronics. The LED's average power consumption with PWM current-control is defined in Equation 4.1 and can

be adjusted with the inrush current I_{LED} and the PWM duty cycle PWM_{cycle} . We studied the effect of both variables by varying PWM_{cycle} from 10% to 50% and I_{LED} from 0.1 mA to 10 mA. We identified that varying the LED biasing power impacts four merits in the system: the signal response, the noise level, the sensor baseline, and of course, power. To identify the best operating point, we defined a figure of merit (FOM) shown in Equation 4.2 that represents the evolution of signal over noise ratio (SNR), baseline resistance and power compared to the original metric (defined at maximum LED intensity). More specifically, ΔSNR is equal to $SNR_{ref} - SNR_{new}$;

$$\Delta R_{baseline} = R_{baseline-ref} - R_{baseline-new};$$

$$\text{and } \Delta Power = Power_{ref} - Power_{new}.$$

$$LED_{pow} = V * I_{LED} * PWM_{cycle} \quad (4.1)$$

$$FOM = \frac{\Delta SNR \cdot \Delta R_{baseline}}{\Delta Power} \quad (4.2)$$

We identified the optimal operating point that produced the highest sensor response while mitigating noise and minimizing power consumption, as shown in red in Figure 4.3. This data-driven approach allowed us to fine-tune the LED bias current, ensuring that the nanofiber sensor operates at the best trade-offs, maintaining chemical detection capabilities ($SNR > 43$ dB for a 40 ppb chemical exposure @ 10 Hz sampling rate), while reducing power consumption to 1.6 mW per LED.

4.2.3 Fabricated Device Performance and Chemical Capabilities

4.2.3.1 Electrical Design and Mechanical Integration

The nanofiber-based chemical monitoring system requires specific electrical design and mechanical assembly to maximize airflow and detection capabilities.

4.2.3.1.1 PCB design. The front-end system is made up of two PCBs stacked on top of each other, the bottom PCB holds the nanofibers and ASIC (Figure 4.4a and 4.4b respectively) while the top PCB contains the LEDs and supporting circuitry (Figure 4.4c). The standalone system includes an optional PCB which connects to the top and bottom PCBs shown in Figure 4.4d with connectors circled in green in Figure 4.4b-4.4d.

The predominant design consideration for the nanofiber PCB was noise reduction. To accommodate this the ASIC (circled in yellow in Figure 4.4b) includes active shielding lines for each of the sensor lines. This significantly decreased the amount of electromagnetic

interference these sensors experienced but increased the complexity of routing the design. The power supply of the ASIC was also a large consideration in the design as embedded system often have very noisy power rails which are not suitable for precise analog circuits. To overcome this we will bypass the power regulation done onboard for the ASIC and use Texas Instruments low dropout voltage regulator (LDO) with 98 dB of ripple rejection (circled in purple in Figure 4.4b), meaning that it can accept a noisy power input and output a very stable and clean voltage. This is important because digital logic circuits such as microcontrollers can create large dips in power at the frequency which their clock runs, which in the case of the AirU is 80 MHz. These power dips can significantly reduce the accuracy of the ASIC because a slight change in voltage can cause a comparator to switch too early or late.

An important component of the mechanical integration of these PCBs is adding airflow guides. The LED PCB has large holes to accommodate an optional fan which blows directly onto the nanofibers as shown in Figure 4.4c. The LEDs on the LED board (circled in yellow in Figure 4.4c) are located directly above each nanofiber (circled in yellow in Figure 4.4a) to reduce the amount of light that spills on anything else, ensuring that it is as efficient as possible. The led controller and temperature/humidity sensor are included on the led PCB (circled in purple in Figure 4.4c). The nanofiber PCB has a hole in the center to allow air to flow out of the gas diffusion chamber shown in Figure 4.4b and 4.4a. The size of this hole was a trade off: it needs to be large enough so that air could flow easily and so a smaller fan could be used to achieve the same amount of airflow; and small enough to leave room to route all of the sensor and power lines around it.

The standalone system includes a power efficient switching power supply (circled in purple in Figure 4.4d) to power the ESP32-mini (circled in red in Figure 4.4d) and the led board from the 5 V input power provided by the USB-C port (circled in red in Figure 4.4b).

4.2.3.1.2 Mechanical assembly. The mechanical assembly was focused on compact size and air flow. The LED carrier PCB was designed to attach to a standard 40mm fan. The LEDs are held on spokes radiating from the center of the board, allowing ample airflow directed at the nano-fibers while the lights remain directly above the nanofibers as shown in Figure 4.4c. The circular section of the PCB covers the motor section of the fan which does not affect airflow, allowing room for the LED controller, and temperature/humidity

sensor.

The nanofiber carrier board has a central hole for the air to flow through after contacting the nanofibers. There is a short distance between the LED sub-assembly and the nanofiber sub-assembly to allow for the light to diffuse from the LEDs so that they cover the whole active area of the nanofibers (the circular section). This distance is also important as the nanofibers have delicate wire bonds which can be easily pulled, so extra tolerance is needed to prevent damage. It is important that this gap is not too large as an increased sensing volume decreases how fast the system can react to chemical exposures: indeed it takes more time for the fan to circulate the air in the system so the exposure gets averaged over a longer time, reducing temporal sensitivity.

4.2.3.2 Fabricated Device Performance

The design of this chemical monitoring platform is focused on portability and affordability, allowing for large deployments in the future.

4.2.3.2.1 Size weight and power. The standalone system only takes up 3 in³ and weighs 37 g as a full configuration. The fan takes up the most space in the system followed by the gas exchange chamber as shown in Figure 4.5d. The front-end system only takes up 2 in³ and weighs 15 g, without the fan or micro controller sub-assembly. This small size also allows the device to be deployed in a broad range of ways, it can be worn on personnel to monitor their chemical exposure levels, be tossed into an area to determine if it is safe, or be permanently set up similarly to existing ESNs.

The power consumption of the device also lends itself to these applications, using only 52 mW as an expansion system, and 253 mW as a standalone system including communication and a fan shown in Figure 4.6. As shown in Figure 4.5a the majority of the power consumption of the standalone system is taken up by the Fan and ESP32. This small power consumption makes it very flexible as it allows for easy integration into existing ESNs without the need for modifying the power systems to accommodate new sensors.

4.2.3.2.2 Cost. The standalone system costs \$95 per unit at an order quantity of 5,000 units, configured with seven chemical sensors. The sensors are the main cost of the standalone system as shown in Figure 4.5c, followed by the ESP32 MCU, enclosure, and fan. The base electronics of the standalone system only costs \$25, and the expansion unit

costs \$15 without any sensors. Without sensors the largest cost of the front-end system are the LEDs and LED driver as shown in Figure 4.5b. The system is compatible with any resistive sensor so other more affordable sensors could be used instead.

4.2.3.3 Chemical Exposures and Identifications

While the main goal of this contribution is to propose a low SWaP and low-cost electronics to record data, this subsection discusses promising chemical identification results. The proposed experiment aims to provide a first insight on the system capabilities to differentiate an exposure between two chemicals, using the response from an array of six sensors.

4.2.3.3.1 Properties of nanofiber response during exposure. Nanofibers demonstrate distinct waveform shapes when exposed to different chemicals at different concentrations. Because fibers are manufactured for chemical selectivity, they also demonstrate different exposure responses between fiber types. Our method involves identifying the chemical gases to which the sensors have been exposed by analyzing the distinct signature or fingerprint formed through the combined responses of these sensors for each specific target chemical. However, the nanofiber baseline drifts over time in controlled environment (fixed temperature, humidity, air composition). For this reason, the sensor responses are evaluated relative to the baseline and the signals require preprocessing before being evaluated.

4.2.3.3.2 Preprocessing. The fiber response (in ohms) is preprocessed to remove the baseline and establish relative magnitude of reponse. Baseline for the signal is established using a piecewise least-squares fitting. A typical exposure causes a variation from the baseline value as low as 1 to 5% (relative to baseline). The value is then normalized to the range -1 to 1 using a tanh sigmoid function, which is weighted to amplify responses in the expected percentage range and clip larger values. The derivative of the relative magnitude is also calculated. The derivative and magnitude of the fiber was found to be the most effective predictors for chemical exposure.

4.2.3.3.3 ML methodology. The machine learning model is trained to differentiate between two chemicals of interest, for instance, acetic acid and acetone. We generate one model per pair of chemicals. The model's inputs are the last 64 time-samples of

the normalized response of the six sensor to a particular chemical, as well as the last 64 time-samples of the normalized variance and first order derivative. This matrix is then passed through a convolution 1D layer which then goes through three stages of dense layers. Finally, the data are re-aggregated and the model outputs two values, representing the predicted level of each chemical in the model. We trained and tested the algorithm on different (and randomized) datasets. Figure 4.7 shows the normalized data of the sensor array (in red in Table 4.1) during 4 successive exposures to either acetic acid (in blue) or acetone (in red). The machine learning algorithm (the bottom plots) provides the two outputs during each chemical session (acetic acid on the left, acetone on the right). The largest output represent the predicted chemical. We can see the model tends to predict a higher presence of acetic acid during acetic acid exposures and respectively tends to predict acetone during acetone exposure. The model successfully identifies the correct exposed chemical 88.44% of the time.

4.2.3.4 Chemical Detection Results

We used a combination of six different chemicals (from Table 4.2) to provide a first estimate of the performance of the system. A distinct training was done for each pair of chemicals, yielding 15 models, one for each chemical pair.

Recognition results are presented in Table 4.2, identification was more accurate for chemicals with larger training data sets. Because the model identifies between two chemicals, the table is symmetrical. Nitrogen dioxide showed the best recognition rates when compared with any other chemical. Methyl-salicylate showed the worst recognition rates when compared against any other chemical. There are no specific fibers doped for methyl-salicylate. On average, using an array of six sensors, our proposed system can differentiate 2 chemicals at 86.69%.

4.2.4 Contribution Summary

Since current ESNs monitor a narrow spectrum of chemicals, our contribution addresses this gap with a new system featuring a broader range of chemical sensitivities to work alongside and integrate with existing ESNs. As part of this contribution, we manufactured a flexible system can interface with up to 12 chemical sensors, and can either be integrated into an existing ESN using only the front-end system, or can operate as its

own standalone system. This standalone system provides a 86.69% accuracy in detecting acetic acid, chlorine, and ammonia in lab trials. This standalone system boasts a low SWaP at 37 g, taking up only 3 in³, while using 253 mW and only costing \$25. Furthermore the front-end system used to expand existing ESN's capabilities only takes up 2 in³, while using 52 mW at 15 g, and costing \$15 with the same chemical detection accuracy. Moving forward, this system can be deployed to provide more data on chemical pollutants in cities.

4.3 Proof of Concept: A Low Level of Detection Platform for Monitoring Acetic Acid in Gases

The previous contribution focuses on the electrical and mechanical design and capabilities of the chemical monitoring system. Although it provided laboratory qualitative chemical detections, this contribution further explores the chemical detection capabilities of the system in a real environment.

Indeed, research has shown that monitoring part-per-billion levels of acetic acid can be useful for multiple applications such as health care or wine quality checks. Some studies have shown that the increase in acetic acid concentration in the exhaled breath of patients suffering from cystic fibrosis is significantly higher (180 ppb) than in the healthy population (50 ppb). Moreover, during fermentation of the wine, it is necessary to ensure the amount of generated acetic acid, responsible for increasing the sour taste of vinegar in wine, is detectable. For these reasons, this contribution proposes a portable electric nose capable of monitoring acetic acid in vapors. The detection of acetic acid has been tested under a variety of environmental conditions and this device successfully demonstrated the detection of acetic acid vapor within 1 s with a 5 s exposure of 40 ppb of analyte. Furthermore, we show a proof-of-concept for identifying a patient suffering from cystic fibrosis with a false positive rate of 2.5%.

This contribution discusses the detection of low-concentrations of acetic acid in vapors for both health applications [102] and wine making [103]. We propose to use a combination of emerging organic sensors based on nanofiber technology and an in-house customized interface to detect traces of acetic acid in the air. Section 4.3.1 discusses the sensors and the ASIC used to interface the sensors. Experimental setups and results are shown in Section

4.3.2.

4.3.1 System Implementation

This section discusses the proposed electronic nose for sensing acetic acid. It showcases the nanofiber-based sensor technology, the architecture of the system, as well as the ASIC that has been used for interfacing the sensor.

4.3.1.1 Nanofiber Sensors

The organic nanofibers used in this contribution are shown in Figure 2.4. They come in a tiny 0.025 in^2 package with gold pads that can be wirebonded on a PCB. The nanofibers are functionalized chemiresistive sensors and provide very high sensitivity (*ppb level* detection) and selectivity to many reactive chemicals of interest [64]. The nanofiber shown in Figure 2.4 is a self-assembled one-dimensional (line) *n*-type or *p*-type semiconductor. Due to the highly complex arrangement of the fibers, their ideal physical model is a complex network of capacitor and pn junctions randomly dispersed over the surface. However, at DC biasing, their behavior is similar to a variable resistor whose value depends on the concentration of chemicals. The conductivity of the nanofiber is dependent upon charge density. The analyte directly impacts the conductivity of the nanofiber by changing the electron density. A variation in the chemical concentration in the air changes the conductivity of the nanofiber and, thus, the resistor value. The nanofibers have been proven robust under ambient conditions with high-dark conductivity [64]. Compared to other types of sensors such as MOS gas sensors, acoustic gas sensors, or CNT gas sensors, [15] nanofibers have shown great detection limits at low power consumption. Indeed, while some sensors technologies like MOS sensors [15] require high temperature operations, nanofibers can operate at room temperature and only need green LED biasing for improving its conductivity and response. However, their intrinsic nature make them very resistive $> G\Omega$ and require a specific, high dynamic range readout circuitry for proper interfacing.

4.3.1.2 Resistance-to-Digital Interface

The electronics that we use to interface the sensors is based on a relaxation oscillator. The circuit successively charges and discharges a capacitor at a rate defined by the value

of the sensor's resistivity. The frequency at which the circuit oscillates linearly defines the sensor's resistance and we can monitor the sensor's response by monitoring the output frequency of the chip. This work employs the same type of circuitry as presented in [80, 82, 83] and in Chapter 3. The architecture of the circuit is presented in Figure 4.8 where the nanofiber sensor is represented as a variable resistor R_{sen} . The sensor is biased at 1 V or -1 V based on the input voltage V_{in} buffered at $+V_a$ or $-V_a$.

The voltages of interest are plotted in Figure 4.9, V_{in} is the biasing voltage of the sensor, V_{int} is the voltage of the integration stage, representing the charge of the integration capacitor. V_{amp} is the copy of V_{int} but amplified by a gain G , V_c is the output voltage of the circuit and its frequency monitors the sensor's response. Those four voltages are defined in Equation 4.3.

$$\begin{aligned} V_{in} &= \begin{cases} V_a & \text{if } V_c \text{ is high} \\ -V_a & \text{if } V_c \text{ is low} \end{cases} \\ V_{int} &= \frac{-1}{R_{sen} \cdot C_{int}} \int \left(\frac{V_{DD}}{2} - V_{in} \right) dt \\ V_{amp} &= -G \cdot V_{int} \\ V_c &= \begin{cases} \text{high} & \text{if } V_{amp} < V_{in} \\ \text{low} & \text{if } V_{amp} > V_{in} \end{cases} \end{aligned} \quad (4.3)$$

Between T_1 and T_2 (shown in Figure 4.9), $V_{in} = -V_a$ and the capacitor charges until V_{amp} reaches $+V_a$. At T_2 , the output comparator triggers and V_{in} is set at $+V_a$. The frequency of oscillation $F = \frac{1}{T_{comp}}$ is defined in 4.4 and depends on the integration capacitor $C_{int} = 36 \text{ pF}$, the gain $G = 20$ and the sensor's resistance. Based on the fixed values of the capacitor, the gain and the measured frequency, we can estimate R_{sen} at great resolutions using Equation 4.5.

$$F = \frac{1}{T_{comp}} = \frac{G}{4 \cdot \tau} = \frac{G}{4 \cdot R_{sen} C_{int}} \quad (4.4)$$

$$R_{sen} = \frac{G}{4 \cdot F C_{int}} \quad (4.5)$$

The capacity of the interface to monitor the sensor's response is defined by its noise performance. The circuit has been fabricated in a 180 nm node and assembled on a 6 layers PCB for testing. The noise performance has been measured by interfacing a low-noise thin film resistor. The output frequency has been measured using a low-jitter (1 ppm) reference clock over 10 seconds. This captures the noise effect down to 0.1 Hz for both the thermal

noise and flicker noise of the circuit. The output measured jitter in the frequency directly characterize the noise performance of the circuit and the histogram of the measurements is shown in Figure 4.10. We measured a noise performance of 156 ppm at room temperature. This corresponds to a 0.0156% level of noise relative to baseline. This value also sets the limitations of the smallest sensor's variation we can measure.

4.3.2 Experimental Methodology

Nanofiber sensors were tested under controlled laboratory conditions to characterize their behavior when challenged with acetic acid analyte. This section discusses the test setups and conditions. We provide results for testing the sensors and electronics under multiple conditions and we also discuss the limit of detection of the system.

4.3.2.1 Experimental Setup

Chemical challenges were generated with certified permeation tubes (KIN-TEK Analytical, La Marque, TX) containing acetic acid using a Sabio Model 2500 permeation oven (Sabio, Round Rock, TX). The permeation oven was connected to a four-way valve via stainless steel tubing. The valve could be switched between providing flush zero air or analyte-laden zero air to the acetic acid nanofiber device. The humidity line output of an Owlstone OHG-4 humidity generator (Owlstone, Westport, CT) was split and provided the same amount of humidity to both the flush air line and the analyte challenge line. The acetic acid sensor device was equipped with two individual acetic acid nanofiber sensors (acetic acid nanofiber A and B, respectively) for replication. The device was challenged with acetic acid vapor at 10, 40, 100 and 1100 ppb, respectively. Another set of experiments added 23 and 45 % relative humidity, respectively, to 40 ppb acetic acid challenge. The nanofiber sensor response was analyzed with Matlab version R2022a (MathWorks, Natick, MA).

4.3.2.2 Chemical Identification Results

The following paragraphs provide chemical identifications results in a controlled environment.

4.3.2.2.1 Nanofiber's response at 0% humidity and characterization of the Signal-over-Noise Ratio (SNR). At environmental conditions of room temperature (22 deg C),

ambient pressure and 0 % relative humidity the lowest detectable acetic acid concentration was 40 ppb (Figure 4.11). The concentration-response relationship and the challenge time-response curve were determined to be non-linear . The time to respond and standard deviation for acetic acid nanofiber A was 1.94 +- 0.35 s. The time to respond and standard deviation for acetic acid nanofiber B was 1.42 +- 0.50 s. The time to respond between acetic nanofiber A and B was significantly different with a p-value of 0.00001. The correlation of the response integral between the replicated acetic acid nanofibers A and B response was 0.89, indicating good tracking of challenges amongst individual acetic acid fibers. The standardized response integral to repeated 40 ppb acetic acid challenges at randomized times and challenge duration showed very good reproducibility in the sensor response (in blue in Figure 4.12). The average sensor's response at 40 ppb was about 0.7% with a standard deviation of 0.0169% across multiple measurements which corresponds to the noise level of the system. The signal over noise (SNR) ratio of the system is defined in Equation 4.6 using the smallest response of the sensor. The noise level of the system is measured during the first 10 seconds of all the recordings prior to the first exposure, for a noise bandwidth of 100mHz to 5Hz. The 33dB SNR provides great detection capabilities at 40ppb of acetic acid.

$$SNR = 20 \cdot \log_{10}\left(\frac{Response_{40ppb}}{Noise_{SystemRMS}}\right) = 20 \cdot \log_{10}\left(\frac{0.7\%}{0.0156\%}\right) = 33dB \quad (4.6)$$

4.3.2.2.2 Effect of humidity on the sensor's response. In order to investigate the nanofiber performance under extended environmental conditions we added humidity to the trial conditions. At 23% RH a distinct response was present, however, at the conclusion of the acetic acid challenge in 23% RH a large spike was consistently observed. The very distinct shape with humidity is presented in Figure 4.13 and the response is consistent across multiple exposures. The time to response at both levels of RH increased to 3 s. The same observation was made at 45% RH. The standardized response integral to repeated 40 ppb acetic acid challenges at randomized times and challenge duration in the presence of 45% RH showed very good reproducibility in the sensor response (in red in Figure 4.12). Furthermore, another group has been identified in yellow in Figure 4.12 with large response. These 9 trials corresponds to 9 exposures of analyte after a short interval. This group has seen a zero air flushing interval of below 10 seconds. The 0% humidity group has not been affected by the short intervals, we think the saturation in humidity increases

the release time of chemicals of the sensors. At higher humidity, the required flush time is about 10 seconds for the sensor to show good reproducibility in its response.

4.3.2.2.3 Classification capabilities of the system for higher and lower concentrations of acetic acid. This paragraph discusses some classification results to showcase the capabilities of the system for identifying a patient suffering from cystic fibrosis. [102] has shown that on average, patients suffering from cystic fibrosis were releasing much higher concentrations of acetic acid in their breath compared to healthy population (180 ppb vs. 50 ppb). We performed two different recordings at close acetic acid concentrations (40 ppb and 200 ppb) to emulate the different breath of these two populations. Each data set contains 80 exposures at random exposure timings and random time between exposures. To replicate human breath that contains high level of humidity [104], the vapors were both humidified at 45% and room temperature 25°C . We use a combination of primary component analysis (PCA) analysis and classifier algorithm to detect whether the exposure containing high levels of acetic acid or low level of acetic acid. For each exposure, we extract the first 6 seconds of the responses of the sensors and perform PCA over the extracted signal. We use 35 trials, picked randomly, for training and the remaining ones are used for testing the classifier. Based on our PCA, we identified that 99% of the signal information is contained within the first component, which is used for the classifier. When challenging the classifier with the remaining 45 exposures, we are able to identify an unhealthy individual with a false positive rate of 2.5% on average. Based on the very small amount of training data and the low false positive rate, we believe the system can be seen as a promising proof-of-concept for detecting cystic fibrosis.

4.3.3 Contribution Summary

The early detection of cystic fibrosis in the human population and in wine faults during fermentation require very sensitive and portable electronic noses. In this contribution, we proposed a 2 inch^2 wireless electronic nose for detecting acetic acid in gases. This contribution's system uses a relaxation oscillator to directly interface the nanofiber sensor and converts its intrinsic resistance value to a frequency which is measured and sent over bluetooth using the integrated digital controller. This work demonstrated great limit of detection using nanofiber sensors down to 40 ppb . This work also includes sensor

responses for different humidities to accommodate for the presence of water vapor in human breath and wine. Additionally, this work has successfully shown the detection of acetic acid within 1 s with a 5 s exposure at 40 *ppb*.

4.4 Chapter Summary

In this chapter, we investigated and discussed the capabilities of our sensor interface contribution from Chapter 3 to monitor nanofiber sensors. Although multiple version of ChemAirU's were manufactured during this dissertation (Appendix A), and multiple data sets support the chemical monitoring capabilities of ChemAirU for relevant applications (Appendix B) this chapter discussed the two following major contributions:

- To improve the limited range of chemicals currently monitored by existing ESNs, the first contribution introduces **a novel system that exhibits a broader spectrum of chemical sensitivities**. This system is designed to complement and integrate seamlessly with established ESNs. As a significant part of this contribution, we have developed a flexible system capable of interfacing up to 12 chemical sensors. This system can be seamlessly integrated into an existing ESN using its front-end module or can function independently as a standalone system. In the context of standalone operation, this system showcases an impressive **86.69%** accuracy in detecting acetic acid, chlorine, and ammonia, as demonstrated in laboratory trials. Despite its robust performance, this standalone setup maintains a low Size, Weight, and Power (SWaP) profile, weighing in at only **37 g** and occupying a mere **3 in³** of space. It operates efficiently, consuming just **253 mW** and comes at a reasonable cost of **\$25**. Likewise, the front-end module designed to enhance the capabilities of existing ESNs occupies a compact **2 in³** space, weighs **15 g**, and consumes **52 mW** of power. This module also offers the same high level of chemical detection accuracy.
- The second contribution of this chapter delves into the practical chemical detection capabilities of the system. Notably, the system's ability to identify cystic fibrosis in the human population and detect faults in wine during fermentation necessitates electronic noses that are both highly sensitive and portable. **In this study, we put forth a low SWaP wireless electronic nose to detect acetic acid in gases**. Its purpose is to detect acetic acid present in gases. This section of our contribution employs

the sensor interface to directly connect with the nanofiber sensor. Our research showcases very low limit of detection using nanofiber sensors, capable of reaching concentrations as low as 40 parts per billion. Furthermore, this study encompasses sensor reactions under varying humidity levels, accommodating the influence of water vapor in both human breath and wine samples. Another accomplishment of this work lies in successfully identifying acetic acid within a mere **1 s** timeframe, even when exposed to concentrations as low as **40 ppb** for **5 s**. Finally, we are able to identify an unhealthy individual with a false positive rate of **2.5%**.

Table 4.1: Sensor configuration of the fabricated device. In red: The sensors used to train the machine algorithm from Section 4.2.3.4. The reference channel is a thin film low-noise fixed resistance to measure the noise floor of the electronics.

Row \ Col	1	2	3	4
1	<i>HNO₃</i>	<i>REF</i>	<i>SO₂</i>	<i>NH₃</i>
2	<i>CH₃COOH</i>	<i>NO₂</i>	<i>CH₃COOH</i>	<i>SARIN</i>
3	<i>CH₃COOH</i>	<i>CH₂O</i>	<i>SO₂</i>	<i>CH₃COOH</i>

Table 4.2: Percentage identification results when exposing the sensor suite to chemicals pairs (row versus columns).

versus	acetic	acetone	ammonia	chlorine	MES	NO2
acetic	-	88.44%	86.26%	88.40%	80.61%	93.99%
acetone	88.44%	-	87.29%	90.08%	77.73%	88.74%
ammonia	86.26%	87.29%	-	89.70%	82.70%	87.11%
chlorine	88.40%	90.08%	89.70%	-	82.16%	93.72%
MES	80.61%	77.73%	82.70%	82.16%	-	83.39%
NO2	93.99%	88.74%	87.11%	93.72%	83.39%	-

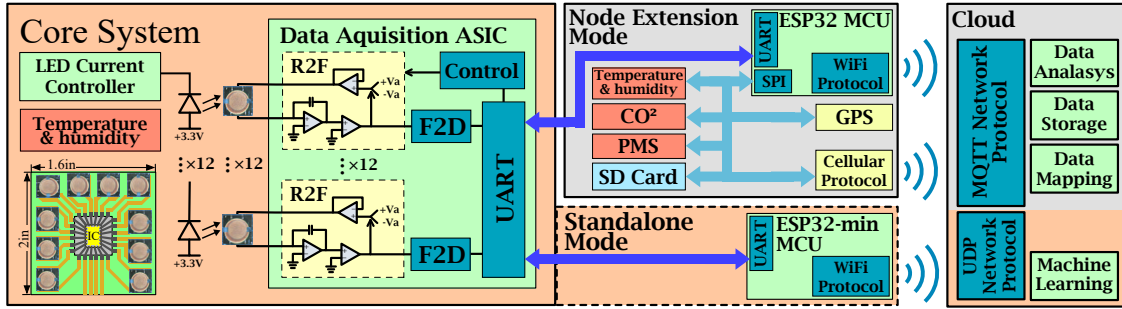


Figure 4.1: Top-level detailed block diagram of the chemical monitoring system. Our proposed circuit is composed of the front-end system (also shown in Figure 4.4a-4.4c) featuring the sensing elements and the interface and an optional circuit with an MCU. The front-end system can act as an ESN node extension when interfaced with an already deployed AirU (detailed in Section 4.2.2.2) through UART. It can also behave as a node in itself (called standalone mode) when interfaced to the optional PCB shown in Figure 4.4d. It can broadcast data to the AirU network through MQTT or to a server through UDP.

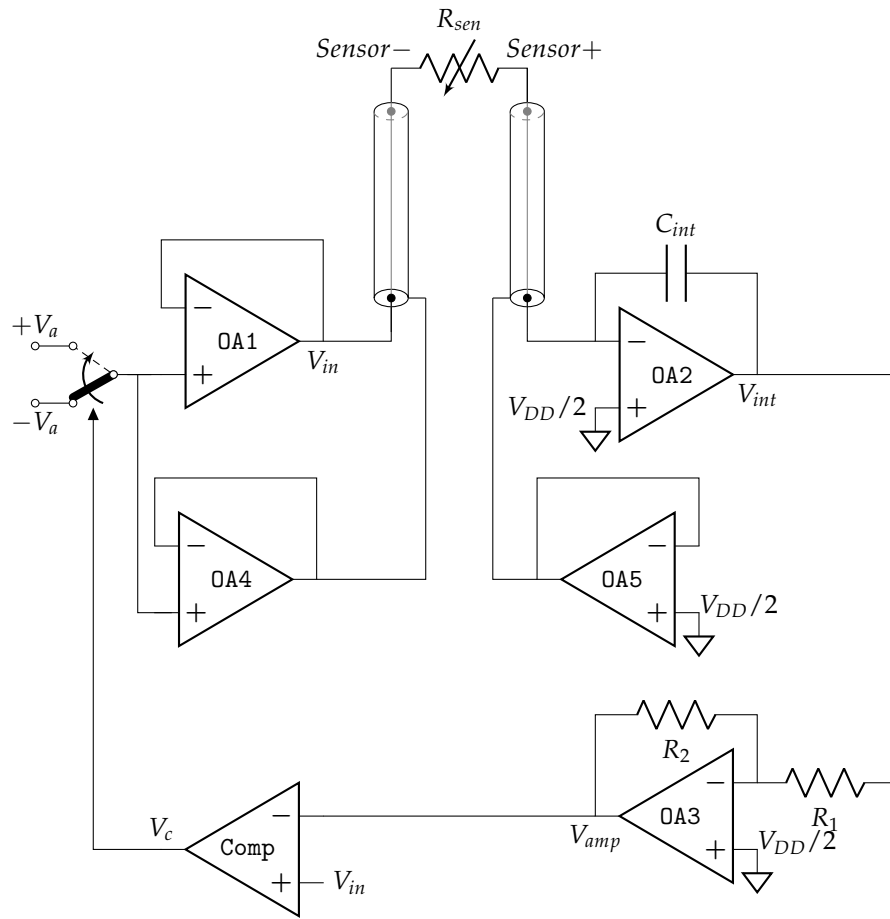


Figure 4.2: Schematic of the resistance-to-frequency circuit used in the ChemAirU system. The sensor lines are shielded with lines driven by the ASIC.

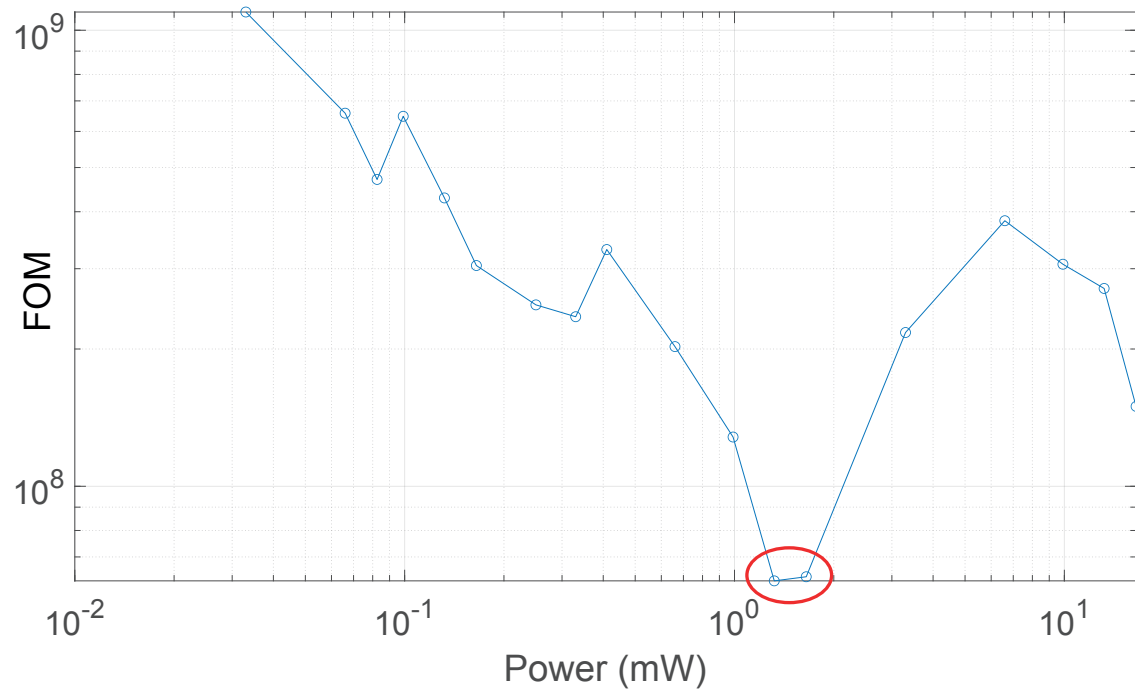


Figure 4.3: FOM (Equation 4.2) versus sensor biasing light power. In the red circle are two optimum operating points, representing the best trade-off between LED power, sensor SNR, and sensor's conductivity.

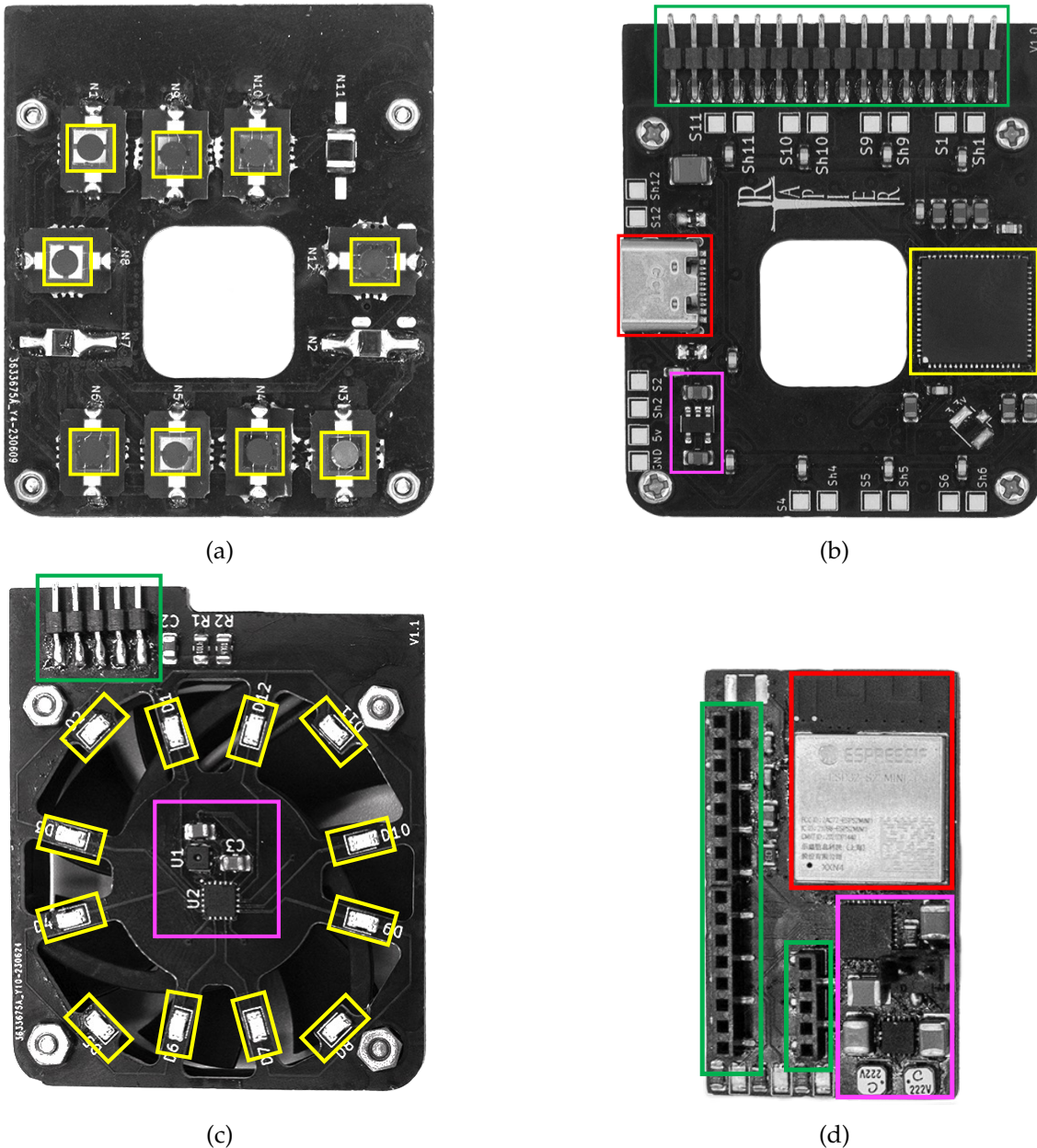


Figure 4.4: Pictures of the assembled PCB of ChemAirU.

- 4.4a: Top-layer of the first PCB of the front-end system. In yellow: the nanofiber sensors.
- 4.4b: Bottom-layer of the first PCB of the front-end system. In yellow: the ASIC, interfacing the nanofibers from Figure 4.4a to the MCU in Figure 4.4d; in red: USB-C power connector; in purple: power circuit; in green: connector to the MCU.
- 4.4c: Bottom-layer of the second PCB of the front-end system. In yellow: the LEDs, biasing the nanofibers from Figure 4.4a; in purple: LED driver, temperature and humidity sensors; in green: connector to the MCU. The top layer of this PCB is for the 40 mm fan.
- 4.4d: Optional PCB to convert the system to a standalone module. It interfaces to the front-end system using the green connectors. In purple: power modules; in red: ESP32-Mini.

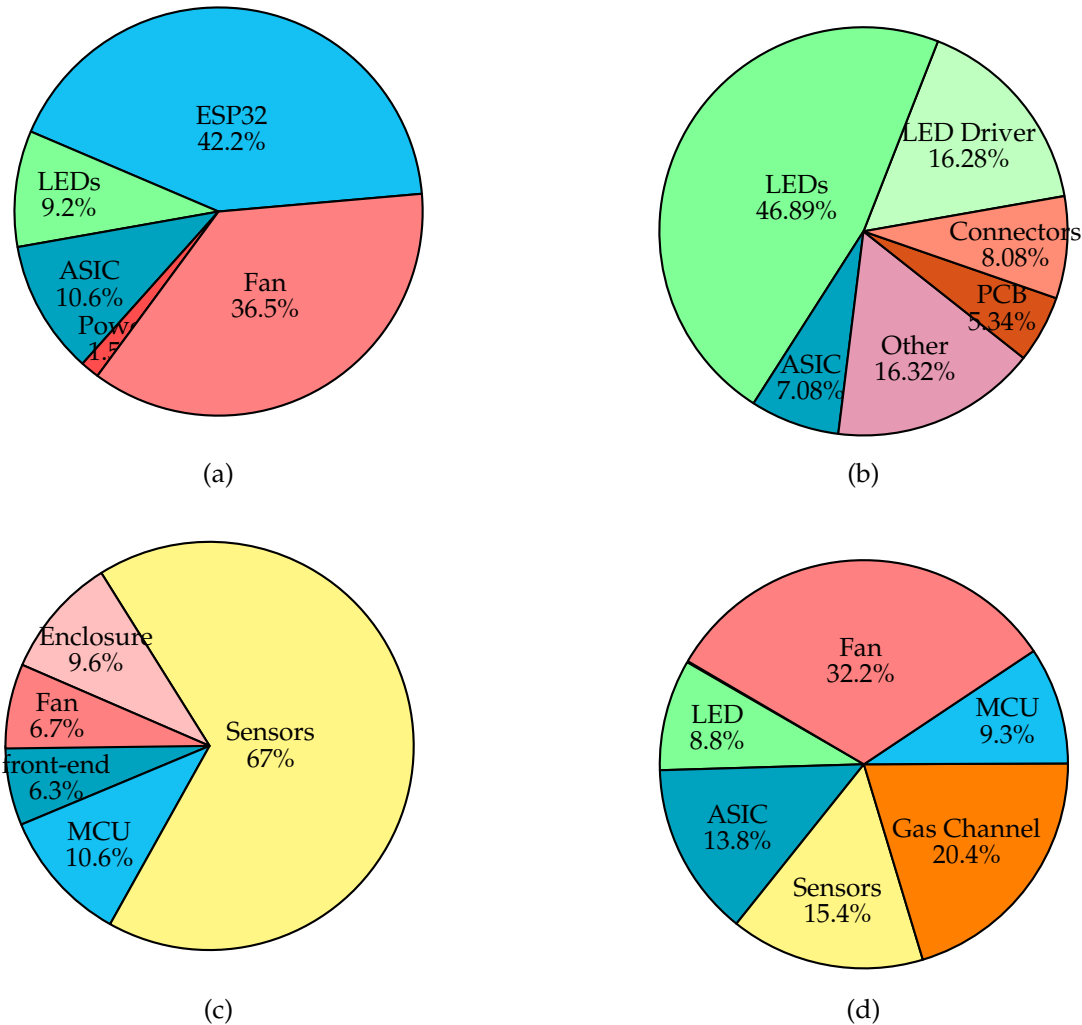


Figure 4.5: Pie charts of the different characteristics (power, costs, size) of the system.

4.5a: Power consumption pie chart of the chemical monitoring extension board.

4.5b: Cost pie chart of the chemical monitoring extension board (5,000 units).

4.5c: Full system cost of the extension board (5,000 units).

4.5d: Volume pie chart of the chemical monitoring extension board.

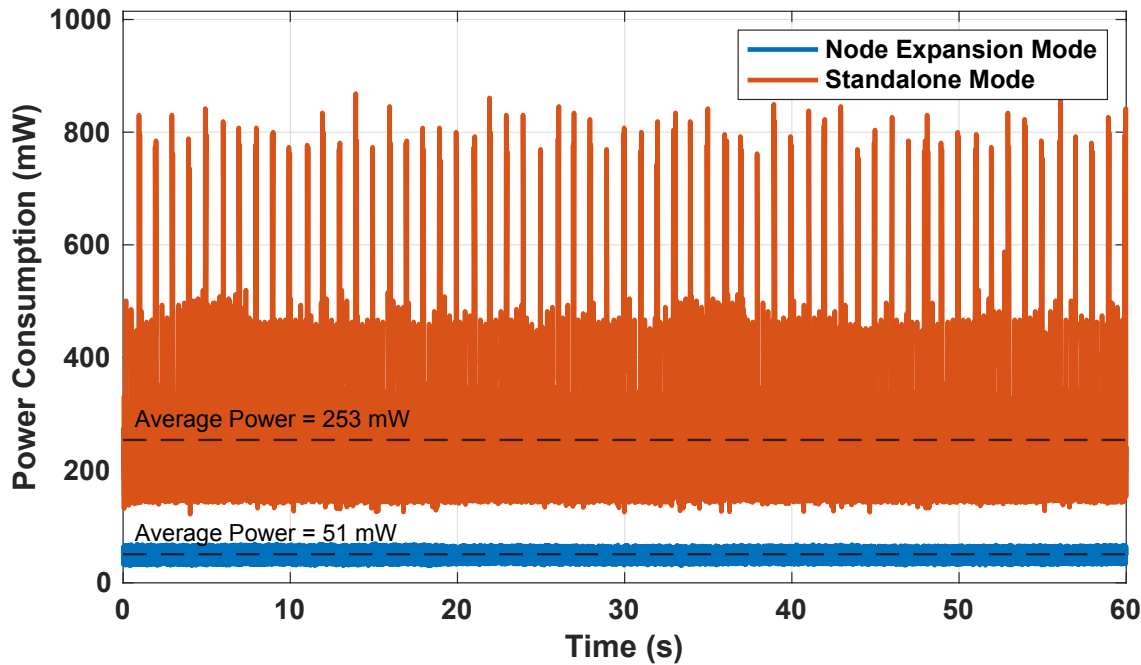


Figure 4.6: Power consumption of the system over time measured at a sample rate of 100 kHz using a NRF-PPK2 power profiler. In blue: power consumption of the system when interfaced with AirU averaging 51 mW; in orange: power consumption of the standalone version (with MCU, wireless streaming @10Hz and fan) averaging 253 mW. The spikes represent WiFi transmissions.

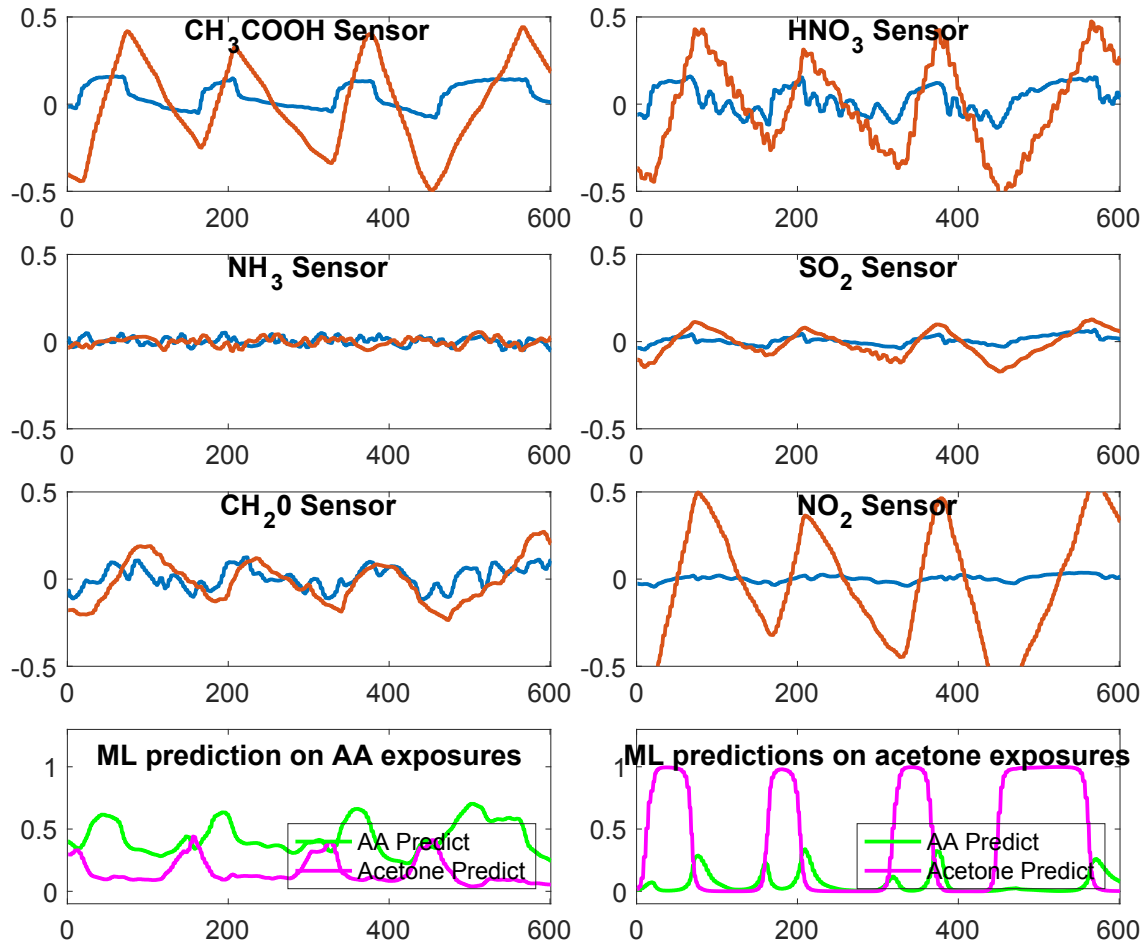


Figure 4.7: Normalized sensor responses to acetic acid (in blue) and acetone (in red) exposures. Bottom plots show the output of the machine learning model over time, bottom-left plot is the ML output for acetic acid exposures while the right one is for acetone. In green the predict for acetic acid; in magenta, the prediction of Acetone.

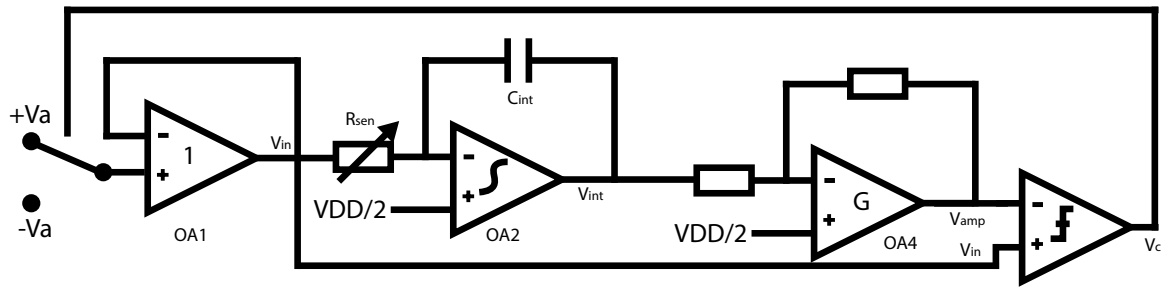


Figure 4.8: Schematic of the analog front-end.

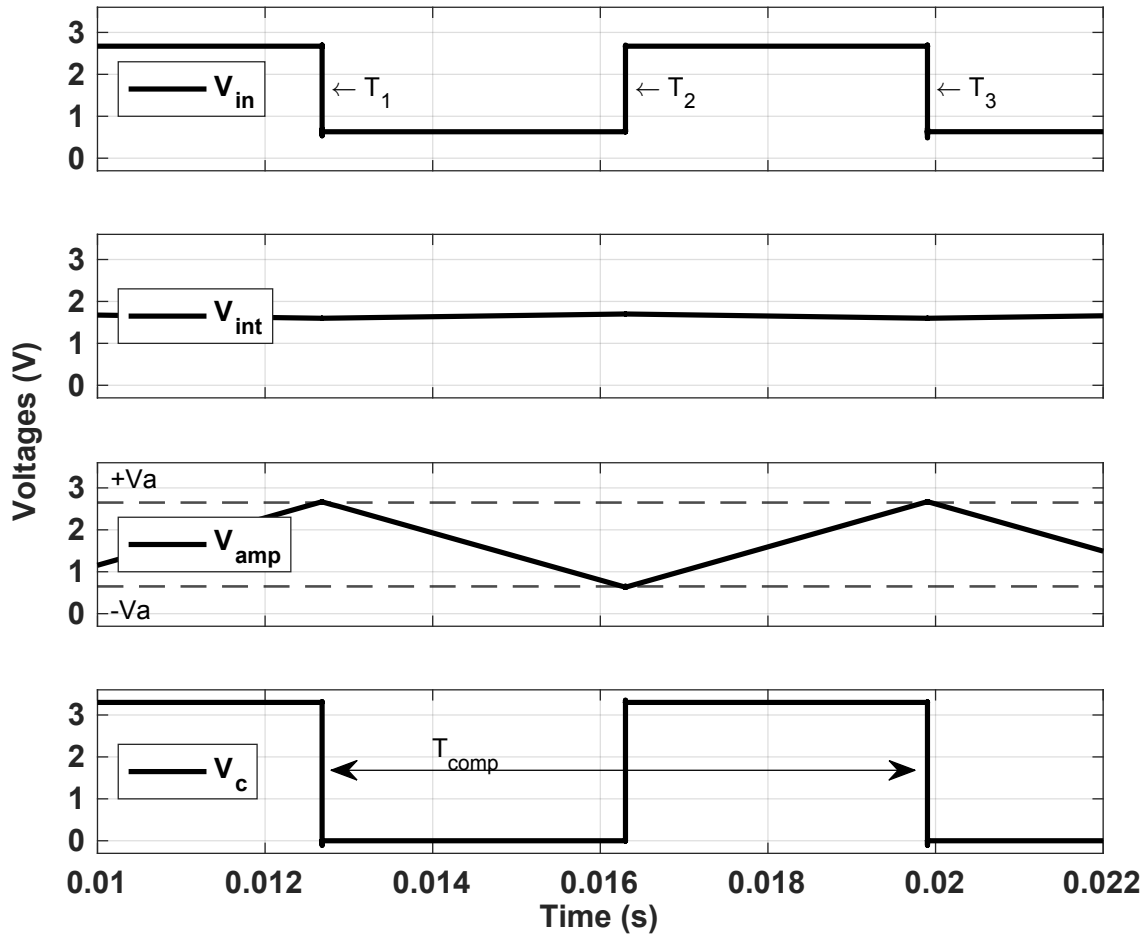


Figure 4.9: Post-pex simulation results of the different voltages.

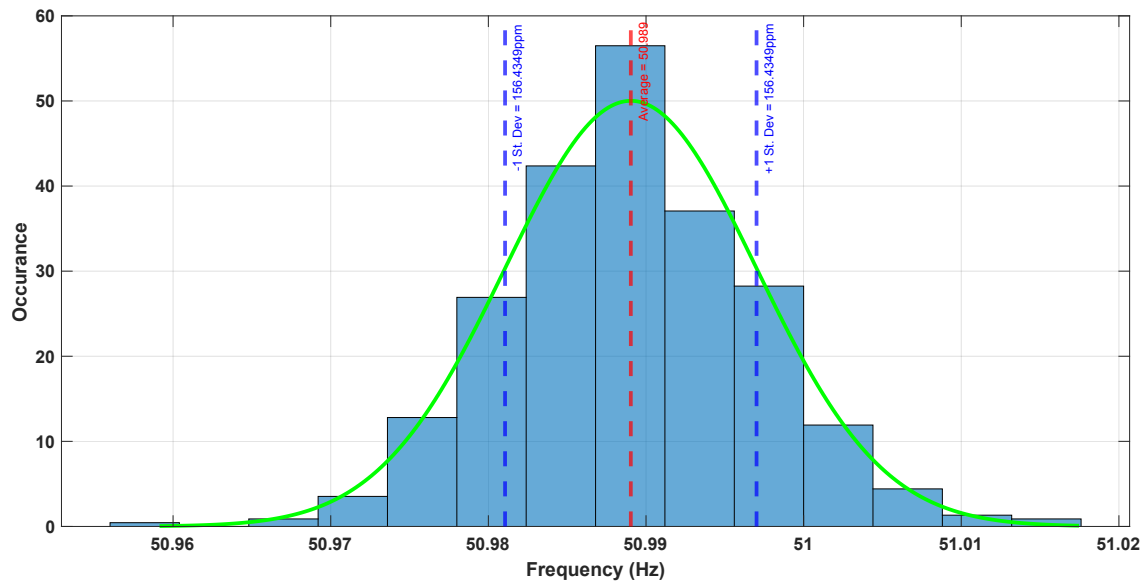


Figure 4.10: Histogram of the output frequency of the ASIC when interfacing a low-noise thin-film resistor.

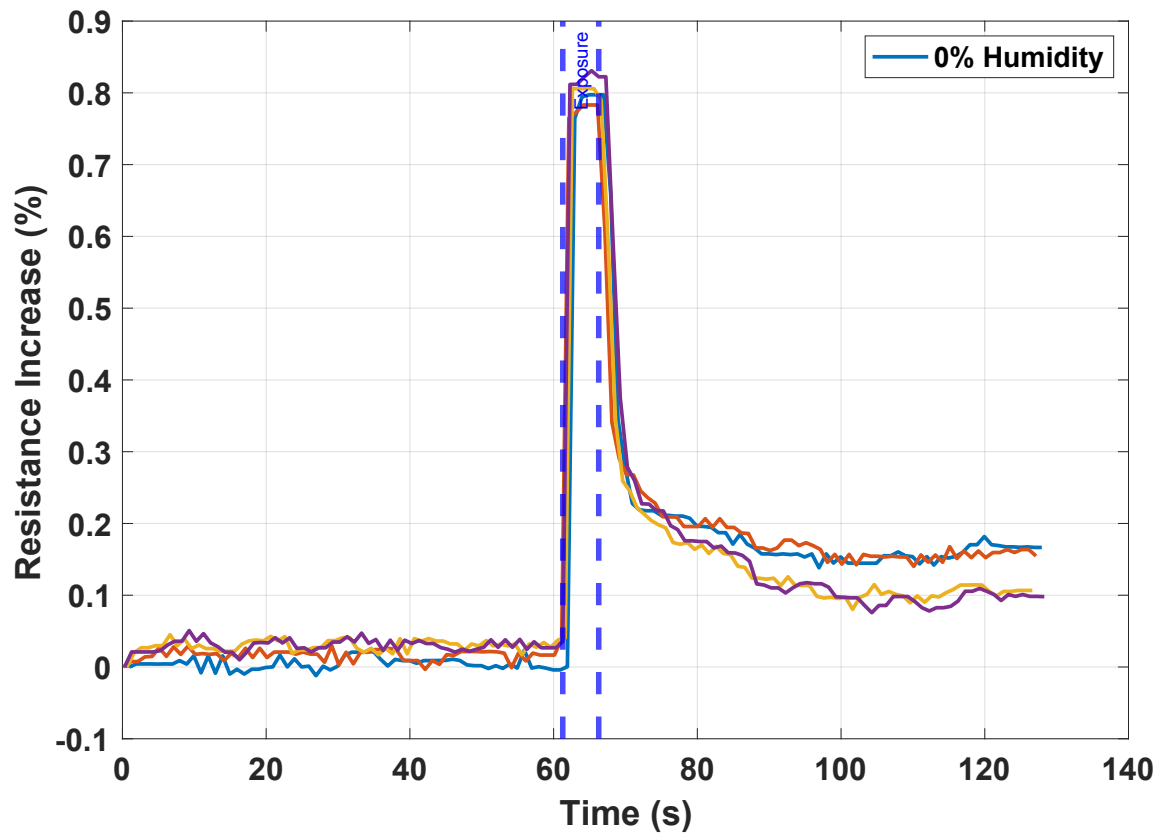


Figure 4.11: Response of an acetic acid nanofiber sensor to a 5 s exposure of acetic acid at 40 ppb.

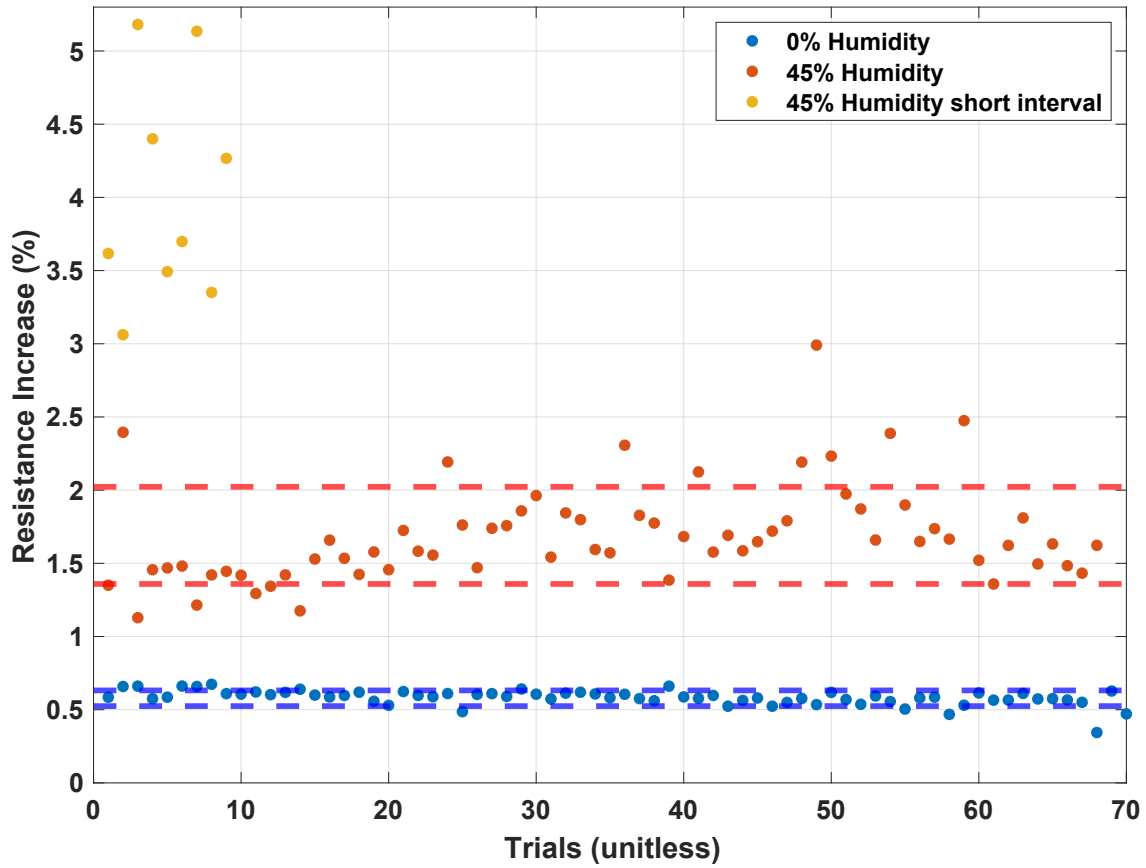


Figure 4.12: Response of the acetic acid sensor to multiple exposure of acetic acid. In blue, the response without humidity, in red: 45% humidity. In yellow: the response with short intervals.

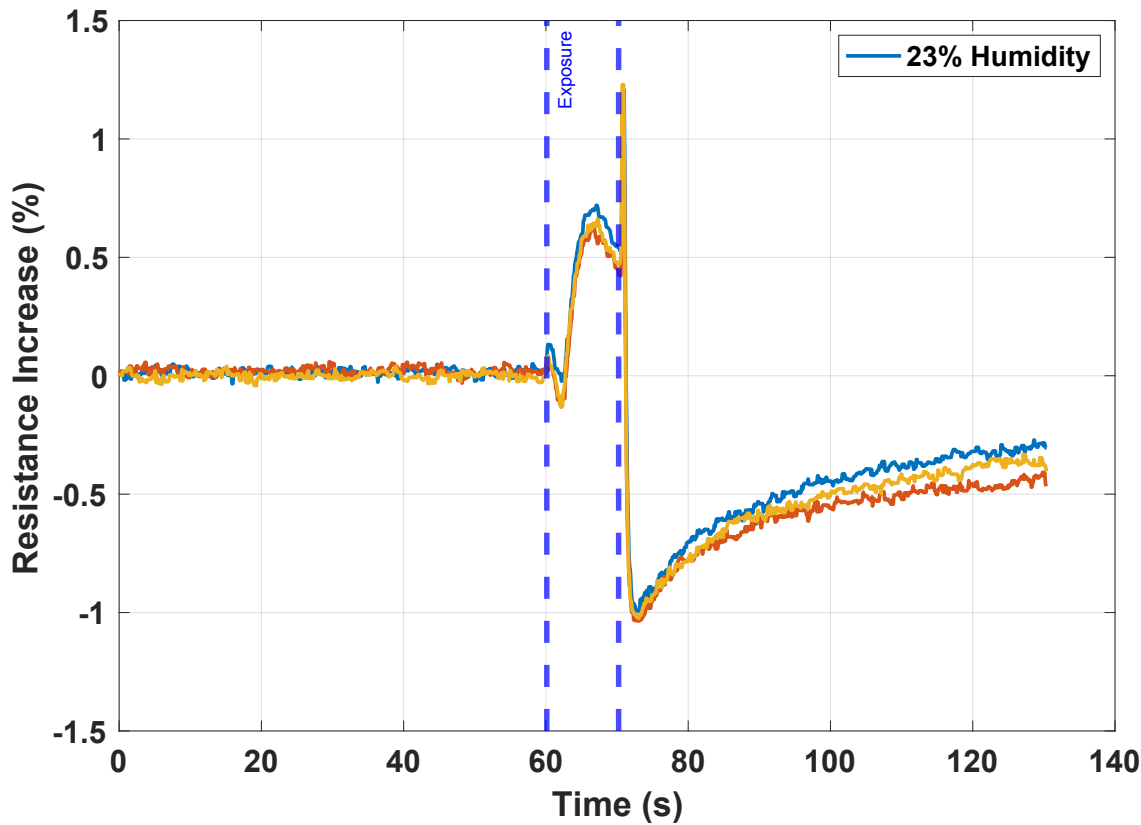


Figure 4.13: Response of an acetic acid nanofiber sensor to a 10 s exposure of acetic acid at 40 ppb and 23% humidity.

CHAPTER 5

CONCLUSION

Maintaining good air quality is now becoming a daily challenge around the world. Our ability to keep air clean will directly impact economical, environmental, and health conditions. For this reason, authorities are performing extensive analysis to estimate long term trends in air quality and measure short term exposures of chemicals in order to better understand the impact of air pollution on our society. Air monitoring is the first crucial step in defining whether political decisions are efficient in improving air quality and, most importantly, the only way to ensure that our society is evolving in the right direction. In this context, the World Health Organization has provided air quality standards in order to ensure a safe amount of pollutants in the air, and cities have been equipped with high spatiotemporal networks of sensors to measure air quality. These low-cost networks of sensors have revolutionized the way air quality data are reported but rely on the quality and quantity of available data for quantifying air quality. In this context, this dissertation explored solutions for enhancing environmental sensor networks with a larger portfolio of chemicals in order to better characterize air composition and the amount of pollutants in the air.

In Chapter 2, we discussed current ESNs state of the art and introduced the AirU pollutant monitoring network as our reference ESN and testbed for our system. We discussed the current limits and lines of research for improving ESN, and showcased that ESNs need to report a multitude of different chemicals in order to fully characterize ambient air composition. We propose an off-the-shelf system that can easily be interfaced with any type of ESN node to improve the chemical portfolio of the network, and we define the system specifications using AirU nodes as a testbed. The proposed system needs to be low-power and low form-factor for mechanical and power integration and also needs to report user-friendly data, which means that some computationnal work needs to be

handled automatically by the system. For this reason, we propose to use a combination of nanofiber-based sensors and in-house ASIC to fulfill this task. The sensors act as a variable resistor, and the ASIC must be capable of interfacing 12 sensors at 100 Hz. Power consumption must be kept negligible compared to the 500 mW of AirU and power consumption limit for the chemical monitoring system is set to be 50 mW for a total power increase of less than 10% for 12 sensors. The ASIC must feature autonomous calibration and computational methods for reporting user-friendly data.

In Chapter 3, we addressed the design of the ASIC. We provided different studies for different requirements on the ASIC, and we provide post-pex or post-silicon results for each approach. We propose three versions of the ASIC, with each individual version aiming at enhancing a specific design requirement:

- The first version of the ASIC aims to **improve the resistance range and measurement error** by using a novel architecture of relaxation oscillator with programmable gain and integration capacitor. The on-board digital controller is in charge of the autonomous calibration for enhancing measurement error and selects the operational range by configuring the gain and the integration capacitor.
- The second version of the ASIC aims at **reducing the power consumption and area** with an improved redesign, optimized for nanofiber-based sensors. The reduction in area allows for up to 12 channels at the same time and data is transmitted by the digital controller through UART.
- The final version of the ASIC is based on the second version and **aims to improve area and sampling rate at very low trade-off by using a novel parasitics mitigation circuitry**. The performance of this ASIC is shown through post-pex simulations and we successfully show that the sampling rate is no longer limited by the sensor's manufacturing process but by the interface itself.

In Chapter 4, we addressed the system integration of the sensors and the ASIC on the same PCB. We integrated 12 nanofiber-based sensors on a tiny 2 in² PCB; the sensors are connected to the ASIC which is placed of the other side of the PCB to minimize the size and sensor's traces length. The LED board is placed on top of the nanofiber PCB and provides light biasing; it is composed of large holes to guide the airflow on top of the sensors. We leveraged the efforts made on the characterization of the sensors to optimize the airflow,

power consumption, and area in order to achieve extremely low SWaP. The chemical monitoring system is connected to an ESP32 mini microcontroller with integrated wifi antenna, and all the data from the ASIC are pushed through WiFi using UDP protocol for real-time data plotting on a laptop PC with MATLAB. The system showed great integrability and serves as a proof of concept for improving ESN with chemical monitoring at low cost, low power, and low form factor. This version of ChemAirU is the final contribution of this dissertation and implements all the contributions of this dissertation in a single system for complete system validation. We have successfully demonstrated the capabilities of the system with the following performance metrics:

- **Cost:** The system costs about \$15 per channel (+\$10 for the sensor)
- **Power:** The system draws about 4.3 mW per channel (including LED), and 2.15 mW per channel without LED (4.8 mW if using the parasitics mitigation circuitry).
- **Weight:** The system weights about 15 g per channel
- **Size:** The system requires about 2 in²
- **Portfolio:** The system can monitor up to 48 different chemical sensors per UART line Appendices A and B provide annotated pictures of the different version of ChemAirU and showcase the size benefits that comes with using our ASIC. Chemical responses for relevant applications are also provided as preliminary chemical monitoring results.

The contributions of this dissertation are described below.

5.1 Summary of Contributions

- **Improving the range of relaxation oscillators through the use of reconfigurable gain stage and integration stage:** We used a novel relaxation oscillator that features a programmable gain stage and a programmable integration capacitance. This allows for reconfigurability of the loop oscillating frequency and we successfully showed a 20dB increase in range compared to state-of-the-art relaxation oscillators. The on-board digital controller handles the configurable stages on the go for transparent stability of the system for the user, and also features an autonomous calibration system for improving measurement error by 3x compared to state of the art. Moreover, the digital controller features a UART controller for direct interfacing to a microcontroller and allows for standalone use of the ASIC without the need of an external expensive off-the-shelf system for converting the frequency to digital.

- **Enhancing power consumption and area of relaxation oscillators for highly resistive sensors:** We designed a relaxation oscillator with a programmable gain stage at reduced range for optimizing area and power when interfacing highly resistive sensors. This design is based on the same topology as the first design but at reduced bandwidth, and therefore, reduced power and area. The interface showed a 4x improvement in area compared to the previous version and 5x improvement in power consumption. Additionally, the ASIC features drivers for shielding the sensor lines and post-silicon results have shown a 20% improvement in noise compared to no shielding. Finally, the ASIC is integrating 12 channels for interfacing 12 nanofibers at the same time.
- **Decorrelating the sampling frequency limitations of relaxation oscillators from the sensor's technology:** We proposed a novel circuitry for mitigating the effect of the sensor's parasitics. We derived that the parasitic capacitance of the sensors limits the sampling rate of relaxation oscillators when interfacing highly resistive sensors. We propose a low trade-off additional circuitry that decorrelates the effects of the parasitic capacitance of the sensor on the sampling frequency of the electronics. We have shown through post-pex simulations that the relaxation oscillator with parasitics mitigation circuitry improves sampling frequency by 30x and area by 13% against our previous interface. Area has been reduced by 13% thanks to the reduced integrating capacitor, and power has been increased by 14% with the added comparator. This interface allows for up to 100 Hz sampling frequency at 50 GΩ, drawing 2.65 mW per sensor.
- **A low SWaP 12 chemical wearable ESN node for smart cities:** We co-integrated 12 sensors on a PCB and interface them to an ESP32mini through UART using our ASIC. The system is named ChemAirU and serves as a proof of concept for improving ESN nodes for smart cities applications. The system monitors 12 different chemicals in real time and we have achieved very low SWaP thanks to the optimized LED biasing and sensor interface. The system draws about 4.3 mW per sensor without the MCU; this figure serves as reference in case the system is to be added to an ESN node. The equivalent total size for 12 sensors is about 2 in^2 with a height of 0.25 in. The weight of the system is about 15 grams and includes the two PCBs used for both the sensors

and the LEDs. And total cost including the sensors is around \$25 per channel. Finally, we showed that the system can be very easily integrated into an existing ESN simply using UART and directly reporting the data from the sensors, at low cost.

- **A low level of detection platform for monitoring acetic acid in gases:** We validated the nanofiber-based proof of concept with the detection of acetic acid. Indeed, early detection of cystic fibrosis in human population and wine faults during fermentation require very sensitive and portable electronic noses. We proposed a 2 inch² wireless electronic nose for detection acetic acid in gases. This work demonstrated great limit of detection using nanofiber sensors down to 40 ppb. This work also includes sensor responses for different humidity to accommodate the presence of water vapor in human breath and wine. Additionally, this work has successfully shown the detection of acetic acid within 1 s with a 5 s exposure at 40 ppb.

Looking ahead, our contributions create a chemical monitoring system that holds the potential for large-field deployment, effectively contributing to the collection of comprehensive data on chemical pollutants in urban environments.

5.2 Future Work

This section briefly discusses and proposes future research directions that are of interest to extend the work presented in this dissertation. This dissertation work has provided preliminary results on the nanofiber sensors and their potential use for air quality monitoring stations. The electronics have been completely validated at post-silicon stage, and we propose to leverage the design of the electronics for future work. Continuing the effort of chemical monitoring in urban environments, future efforts can work with the proof-of-concept system we introduced in this dissertation work and focus on sensor characterization/calibration and data processing/analysis techniques for quantitatively monitoring chemicals.

5.2.1 Deploy ChemAirU Within the AirU Network

The short-term line of research will be to deploy the ChemAirU system within the AirU network, at a large scale. This first step is crucial and will allow for large amount of data collection, required for machine learning training, data analysis, performance estimations, and investigating calibration techniques. This will require the fabrication of the final

version of the ASIC with mitigation circuitry which has been layouted and validated and is ready for tapeout in a 180nm CMOS node. Given the amount of AirU nodes currently deployed worldwide, the fabrication of all the sensors and the ASIC at a large scale is the first step before integration of the system. During this dissertation, the AirU nodes have been upgraded with the nanofibers and the ASIC in low quantity, and we have shown straightforward integration of the sensors thanks to the low SWaP and the UART transmission line.

5.2.2 Pursue the Effort on Sensor Characterization

Although this dissertation has provided preliminary results regarding nanofiber sensors characterization, further data analysis can be done. Further characterization will improve the sensors sensitivity and selectivity, especially when exposed to outdoor environments with large background noise. One future project could investigate how to use the data collected at the same time from each of the 12 sensors to improve selectivity using sensors' cross reactivity. It will be of great interest to provide more quantitative analysis in order to estimate the amount of chemicals in the air. This will be the first step in defining new Air Quality Indexes based on a complete chemical characterization of the air.

5.2.3 Implement a Classifier Algorithm to Generate Alerts During Chemical Spikes

As mentioned previously, the main goal of our research is to provide quantitative chemical measurements, using cross reactivity, and define new AQI and FOMs to estimate unhealthy air. It will be of great interest to design a machine learning model that analyses the response of an array of sensors, calibrates their response based on reference systems and close ESN nodes, and triggers alerts when a chemical spike. This work would allow for complex chemical monitoring on a block-to-block basis in urban environments in real time.

APPENDIX A

FABRICATED DEVICES

In this appendix, we show all the major versions of ChemAirU that were manufactured throughout this Ph.D.

A.1 ChemAirU - Version 1

The first version of ChemAirU does not feature the chemical sensors. This version showcases the capabilities of the tiny-time-series transformer designed for estimating Ozone levels, at the edge. The integrated tensor processing unit in the Google Dev Board allows for low-power and complex machine learning model use in real-time, at the ESN node level.

A.2 ChemAirU - Version 2

The second version of ChemAirU leverages the design of the first ChemAirU using in-house sensor hats for the Google Dev Board. This version includes a multi-stack sensor hat approach to add the nanofiber sensors. This design leverages the airflow channel created by the PCB stacks to guide the outside air onto the nanofibers for optimal air-flow. In 2022, 10 ChemAirU's were deployed in the UK as part of an integration exercise with DARPA and the Defence Science and Technology Laboratory (DSTL).

A.3 ChemAirU - Version 3

The version 3 of ChemAirU is based on the new commercially available AirU Pro. This version improves ChemAirU-V2 in multiple ways. First, this version features swage locks inlets and outlets for airflow. Compared to the version 2, this version can be connected to an environmental chamber for complete characterization and calibration, and can also be directly connected to an FEM equipment such as a TQMS for calibrations against gold-standard measurements. This version also provides better control of the air flow with

the use of a mini-pump, provides cellular connectivity, and features a smaller nanofiber exposition chamber to improve sensitivity.

This version is no longer sitting outside the MIT LL van but inside and connected to the TQMS airlines for better calibrations.

A.4 ChemAirU - Version 4

The final version of ChemAirU improves footprint and power consumption thanks to the use of the ASIC. Version 4 can either operate as a standalone module thanks to its low power and WiFi capable MCU, or can be connected to an already deployed AirU node using UART.

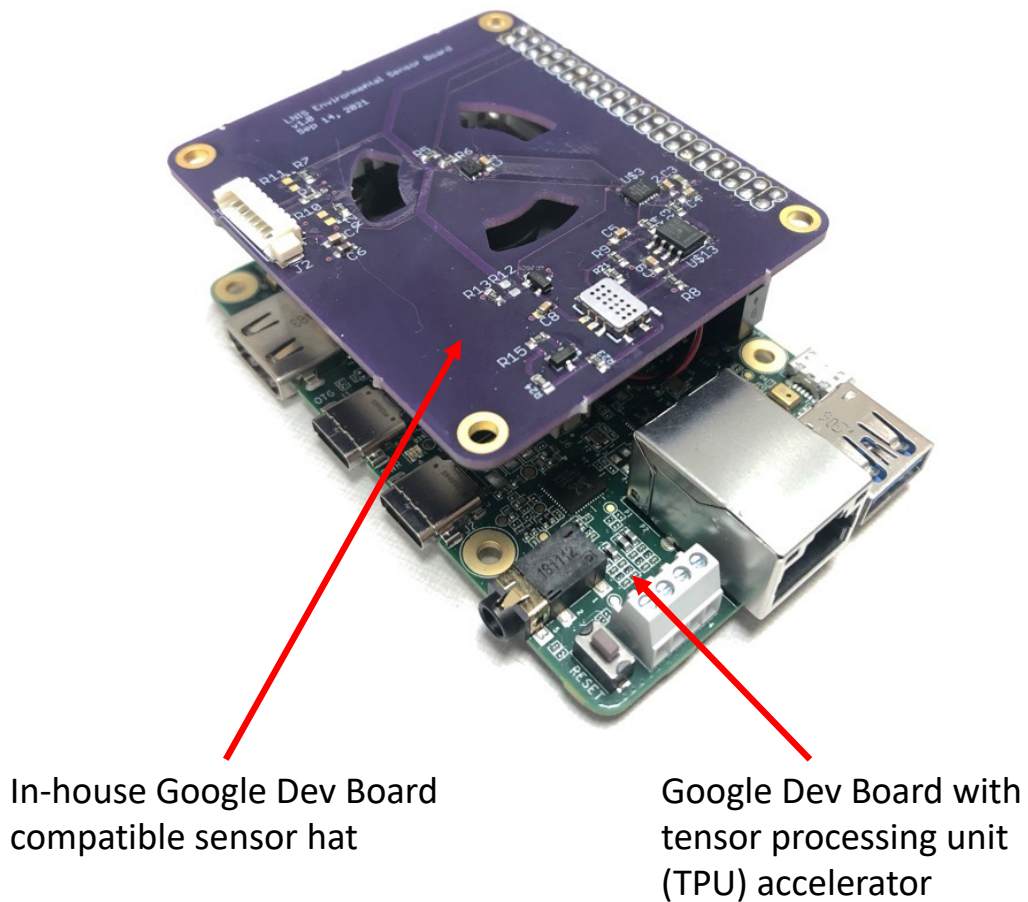


Figure A.1: Photography of the first manufactured ChemAirU. The device is composed of a machine learning accelerated Google Dev Board and a sensor hat.

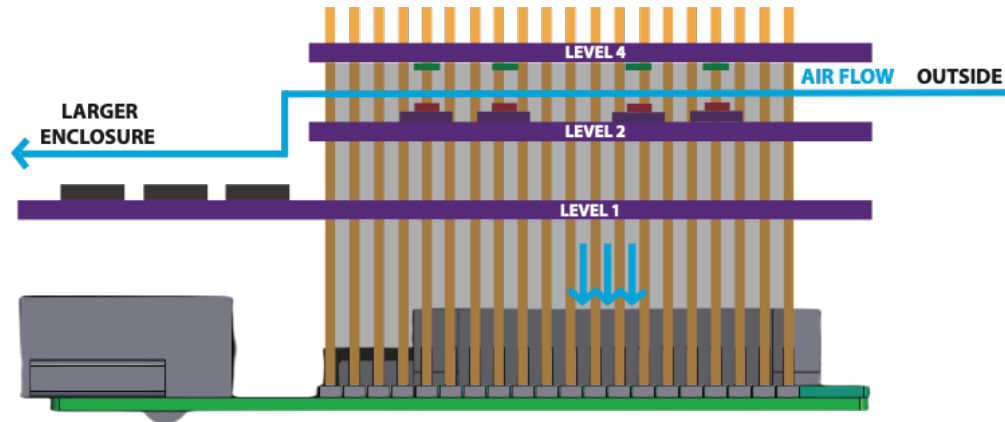


Figure A.2: Side view of the 3D model of the ChemAirU-V2. The system features 4 stacks of PCBs, depicted in the next figure. The nanofibers (level 3) are enclosed between the level 2 PCB and the level 4 PCB. The air flows on top of the sensors for chemical sensing.

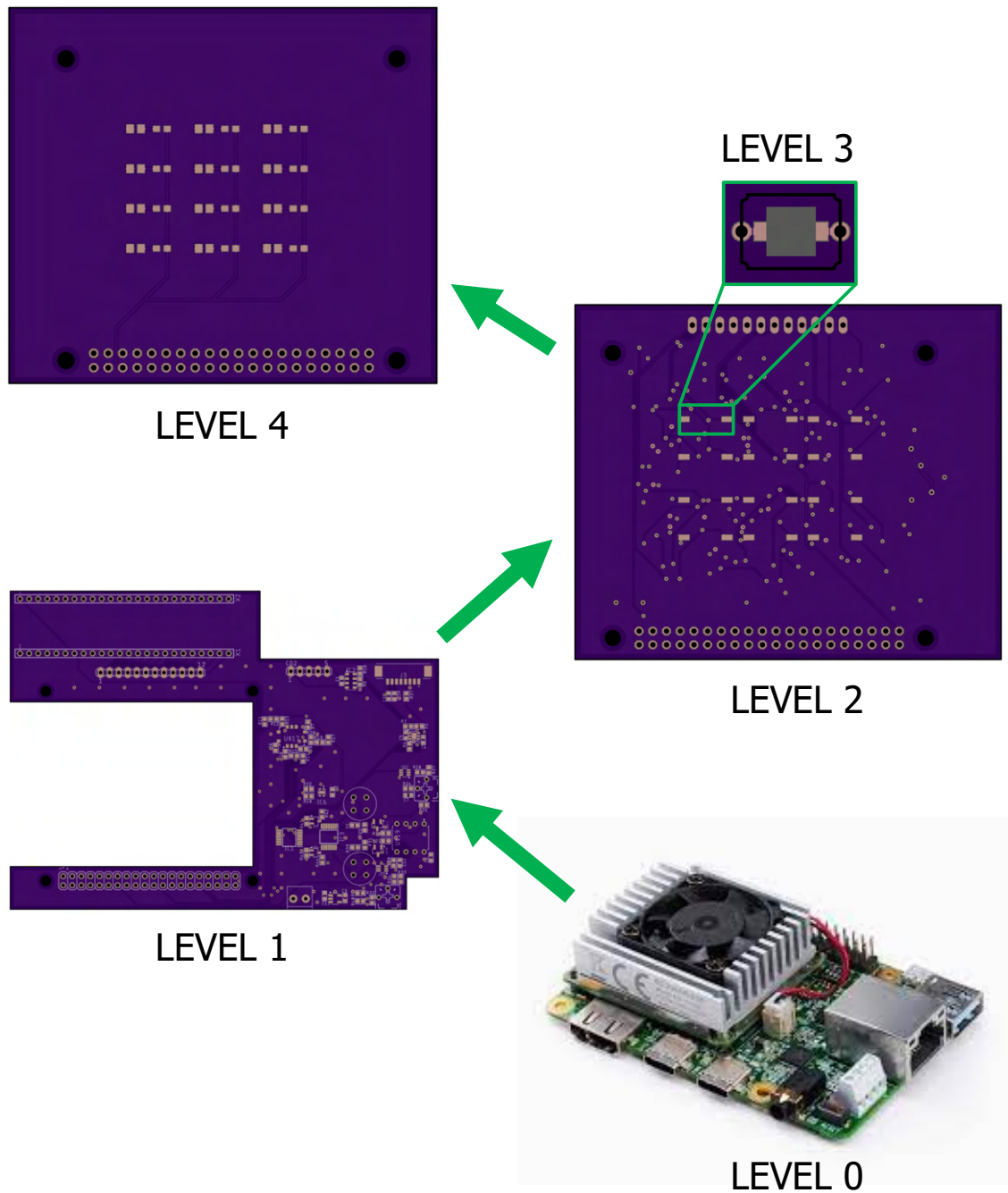


Figure A.3: Photography of the 4 sensor hats for ChemAirU-V2. Level 1: Sensor hat containing off the shelf sensors, already used in AirU, and an FPGA. Level 2: The PCB featuring the discrete electronic version of the sensor interface. Level 3: Nanofiber-receptacle PCBs. Level 4: LEDs.



- LEVEL 4** = LEDs board
- LEVEL 3** = Single nanofiber board
- LEVEL 2** = Nanofiber integration board
- LEVEL 1** = Sensors board
- LEVEL 0** = Coral dev board

Figure A.4: Annotated picture of the manufactured ChemAirU-V2. The sensor hats directly plug into the dual columns 40 pins header of the Google Dev Board to provide power, and serial connection.

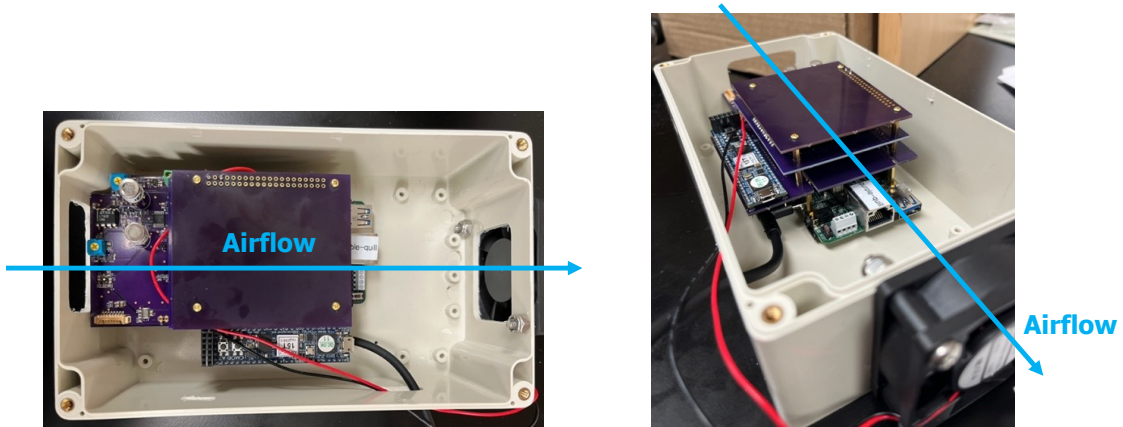


Figure A.5: Annotated picture of the ChemAirU-V2 in its water-proof case. A fan is attached on the bottom of the case to provide airflow. The air is forced onto the nanofiber sensors thanks to the channel created by the PCB stacking.



Figure A.6: Picture of the ChemAirU mounted on the Massachusetts Institute of Technology Lincoln Lab (MIT LL) van. The MIT LL van is equipped with a TQMS for reference measurements and calibrations.

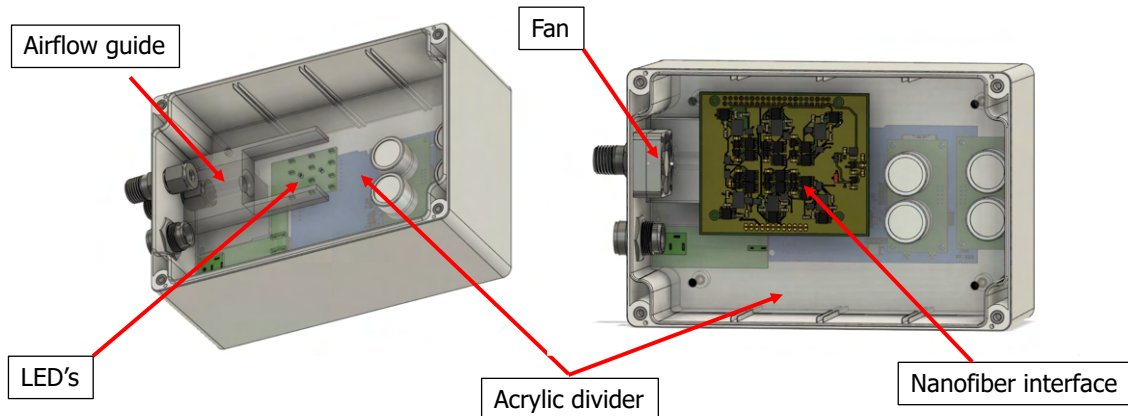


Figure A.7: Annotated 3D model of ChemAirU-V3, this version uses the same waterproof enclosure than version 2. The swage lock inlet is directly connected to an airflow guide, leading to the nanofiber exposition chamber which size has been reduced by half compared to the previous version.

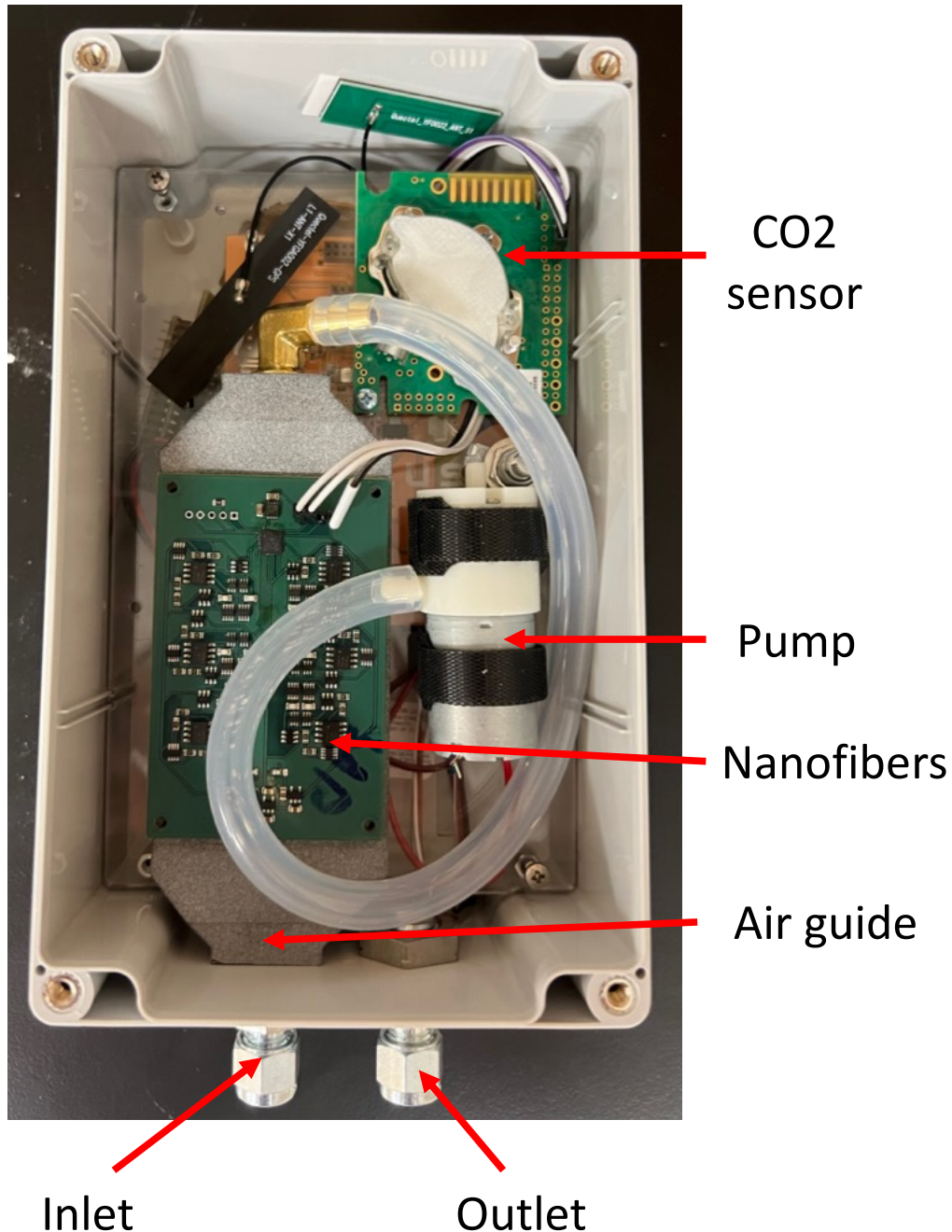


Figure A.8: Annotated picture of the manufactured ChemAirU-V3. The device is populated with a swagelock inlet which can connect the device to 1/4" PTFE tubbings in an environmental chamber. PTFE does not react with chemicals and allows for sensor calibration. The airflow guide exposes the sensors to chemicals. The minipump is calibrated at 1L/min to maximize sensor responses.

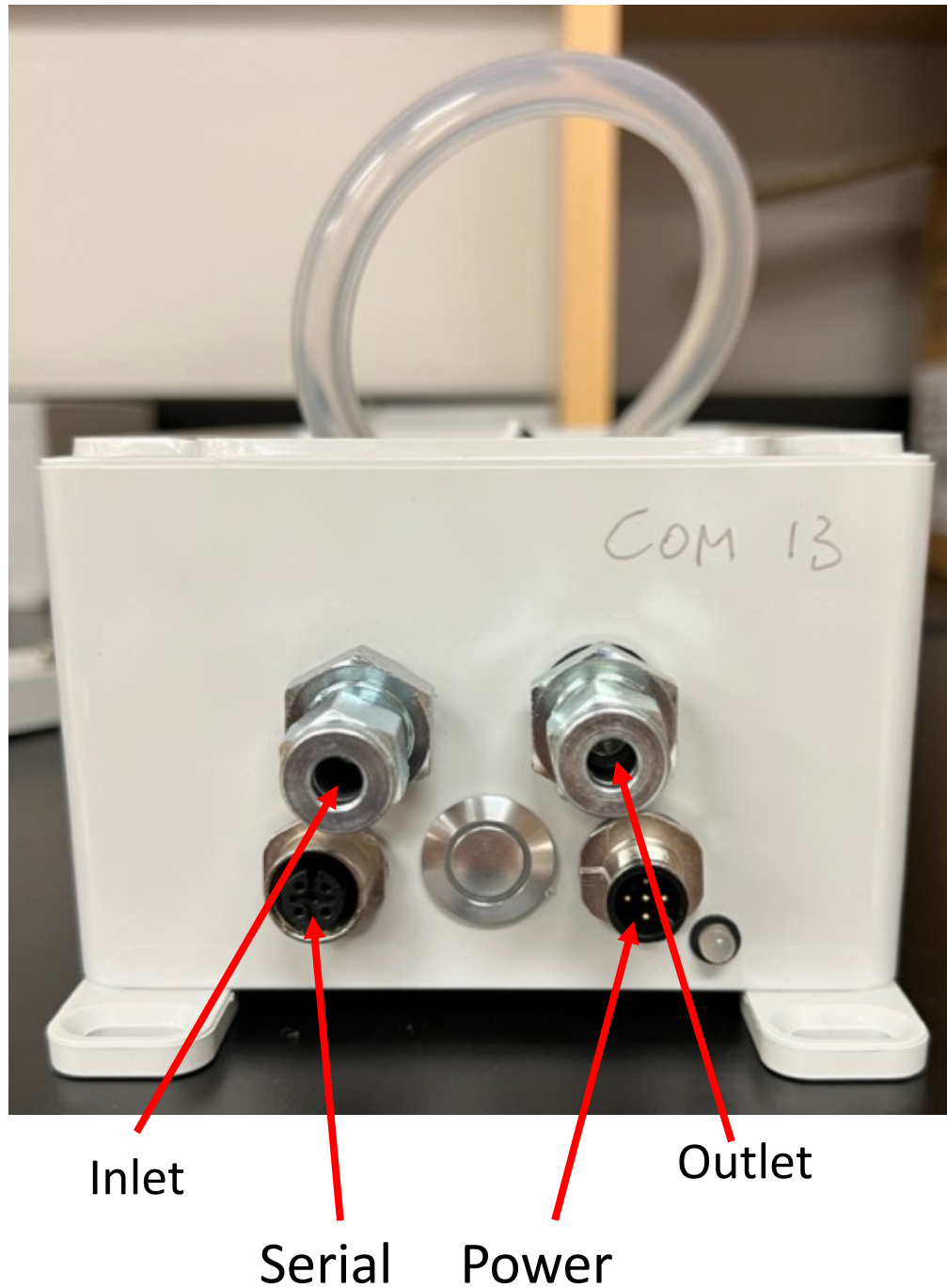


Figure A.9: Annotated picture of the manufactured ChemAirU-V3. The device has the 1/4" inlet and outlet for airflow. The device has one serial port that can be used for configuring the device, updating firmware, or streaming out data. The power port accepts 5 Volts.



Figure A.10: Two ChemAirU-V3 deployed in Indianapolis as part of the SIGMA+ program.

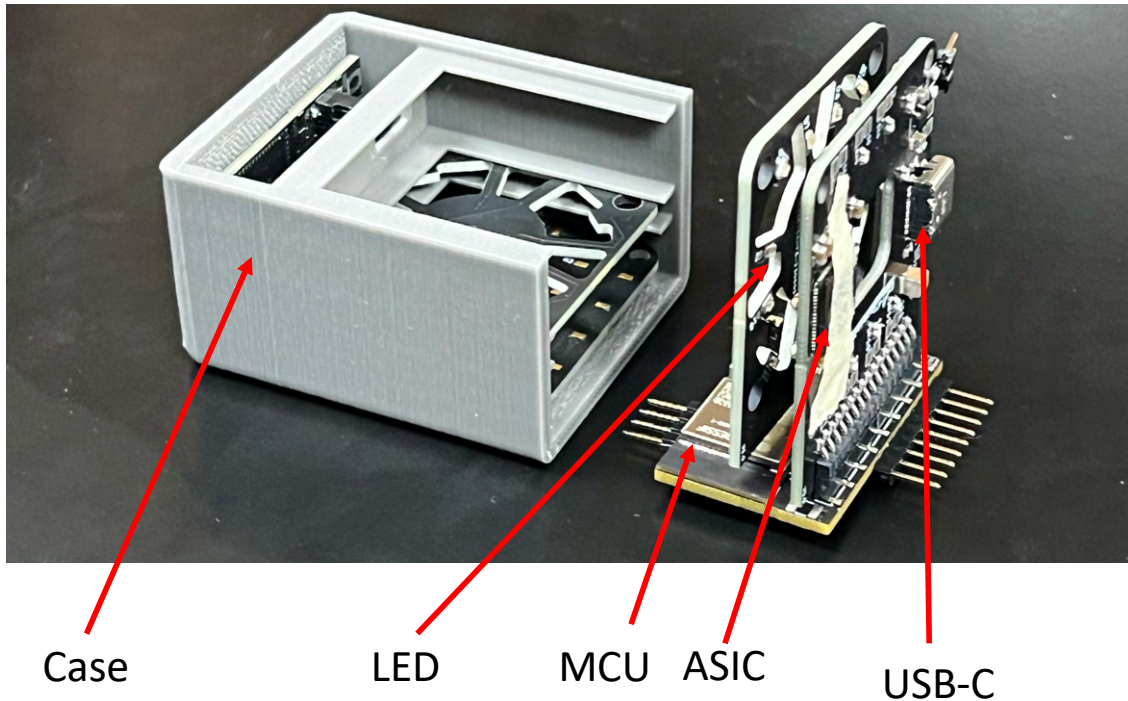


Figure A.11: Annotated picture of ChemAirU-V4 with its case. Compared to the previous versions, this system uses the ASIC to interface the nanofiber sensors and allows for reduced power consumption, minimal sized exposition chamber, and very lightweight form factor.

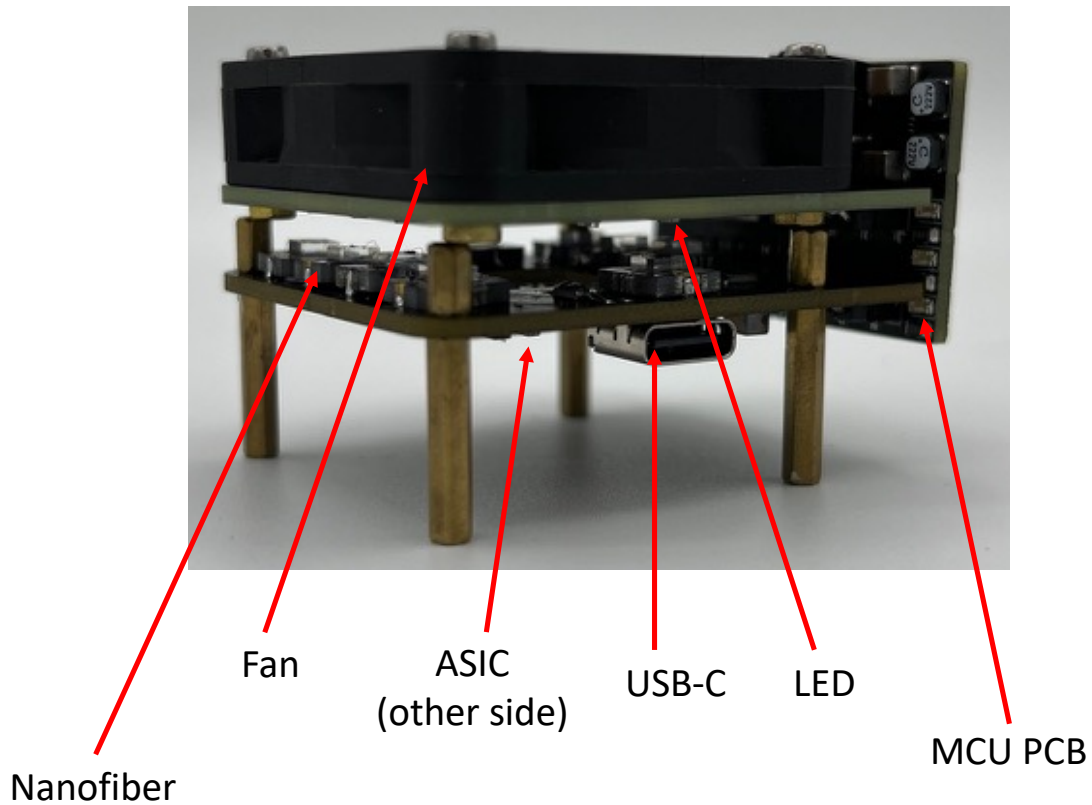


Figure A.12: Annotated picture of ChemAirU-V4 without its case. The core system of ChemAirU-V4 is composed of two PCB. One single-side PCB for the LEDs and the fan. One double-sides PCB featuring the sensors on the upper side and the ASIC on the bottom.

APPENDIX B

CHEMAIRU RECORDING DATASETS

In this appendix, we provide a few examples of datasets from the sensors that are relevant to different applications discussed during this dissertation work, in particular for smart-city, health, and defense applications.

B.1 Smart-City Application

Nitrogen dioxyde is of particular interest in urban environment. Indeed, as discussed throughout this dissertation work, and shown in Table 1.1. The recommended (first interim target) amount of NO_2 reported in AQG is $40 \mu\text{g}/\text{m}^3$, which represents a concentration of 21 ppb of NO_2 . Figure B.1 shows the response of ChemAirU, and more specifically, an NO_2 nanofiber from ChemAirU, to 6 successive exposures of 90 ppb of NO_2 .

Although the peak response from the sensor is not constant during this trial (because of random short exposure and recovery timings), the shape of the sensor is very consistent. The very low noise level in the signal allow for clear response compared to baseline, especially at very low concentrations (90 ppb) that are within range of AQG.

B.2 Human Health Application

Section 4.3.2 discusses the case of cystic fibrosis identification in human health. This section shows sensor responses to different exposures of human breath with extra acetic acid.

B.3 Defense Application

During this dissertation work, one ChemAirUs populated with sensors manufactured for the detection of Sarin (GB), Sulfur Mustard (HD), VX, and Phosgene (CG) was sent to the U.S. Army Combat Capabilities Development Command Chemical Biological Center (DEVCOM CBC) laboratory. DEVCOM CBC is a surety laboratory, licensed to performed

chemical warfare agents studies. During this dissertation work, the ChemAirU was exposed to the four previously mentionned chemical warfare agents: GB, HD, VX, and CG.

The following figures provide sample responses to GB, HD, VX and CG. Due to the very small amount of exposures available to us, these following figures are not statistically significant, and only provide preliminary results for defense applications.

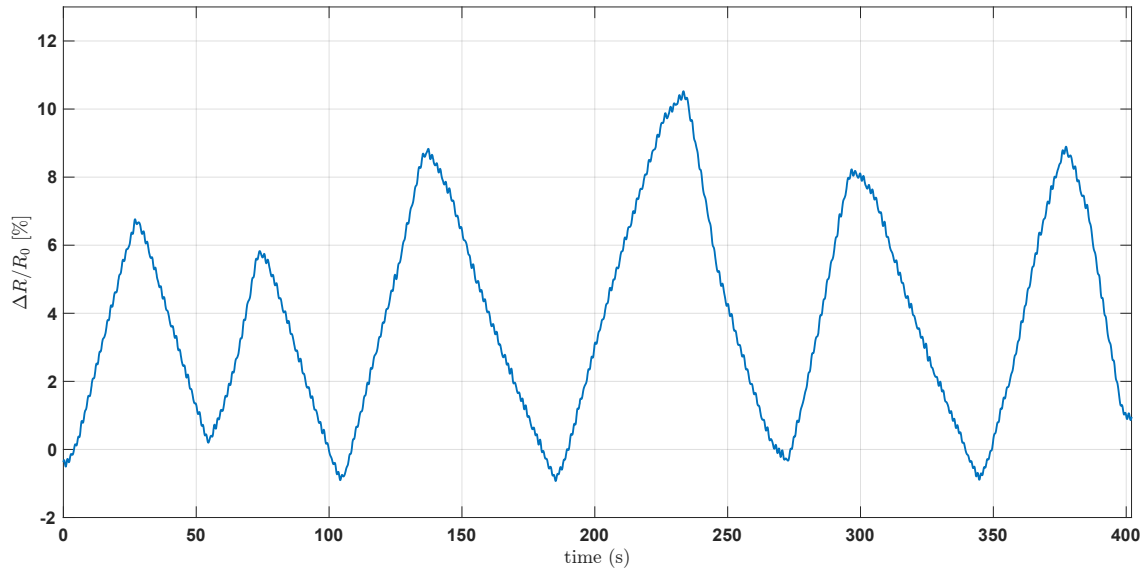


Figure B.1: Response of an NO_2 nanofiber to 6 successive exposures of 90 ppb of NO_2 . The response is shown as relative variation to baseline in term of sensor's resistance.

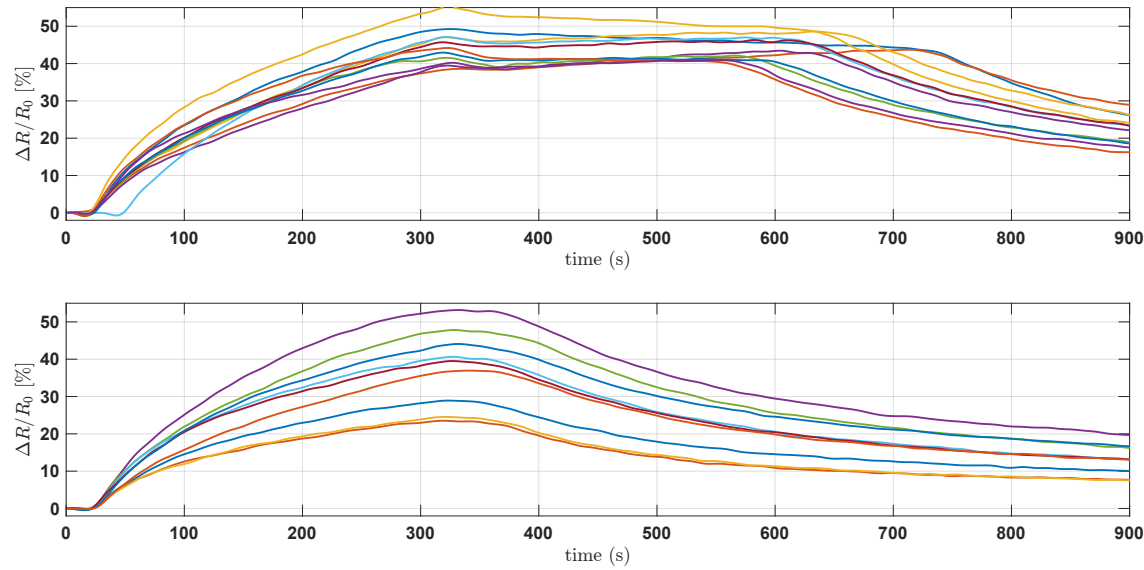


Figure B.2: Response of an acetic acid nanofiber to multiple exposures of human breath. The top plot shows responses to breath only. The bottom plot shows responses to breath with added 200 *ppb* of acetic acid. The response is shown as relative variation to baseline in term of sensor's resistance.

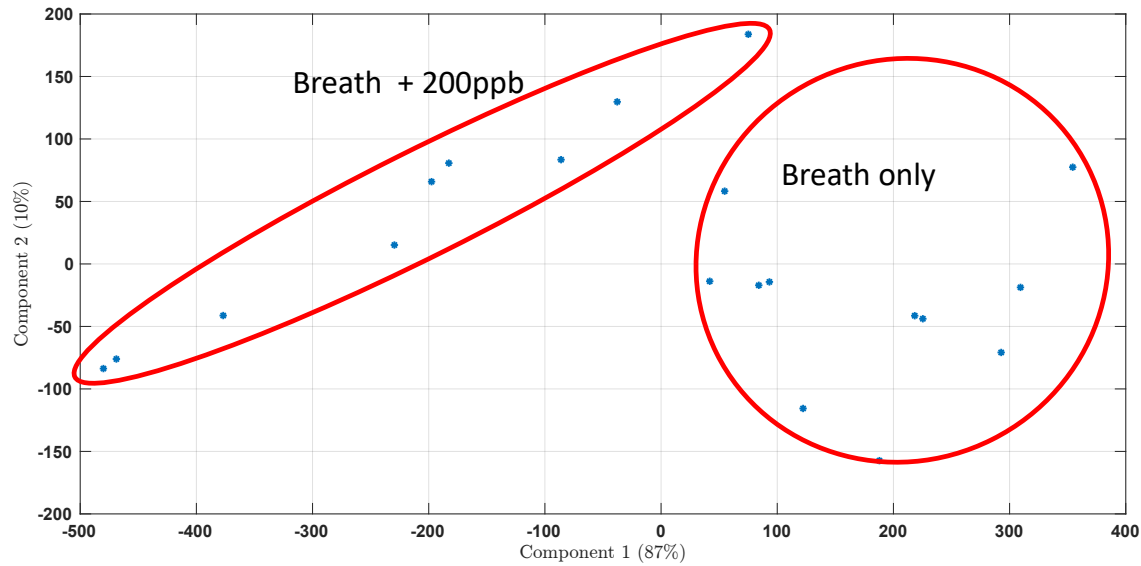


Figure B.3: PCA analysis plots of the previous sensor responses from Figure B.2. The plot shows the first PCA component versus the second component. Two distinct groups are annotated, representing the breath only responses and breaths with extra acetic acid responses.

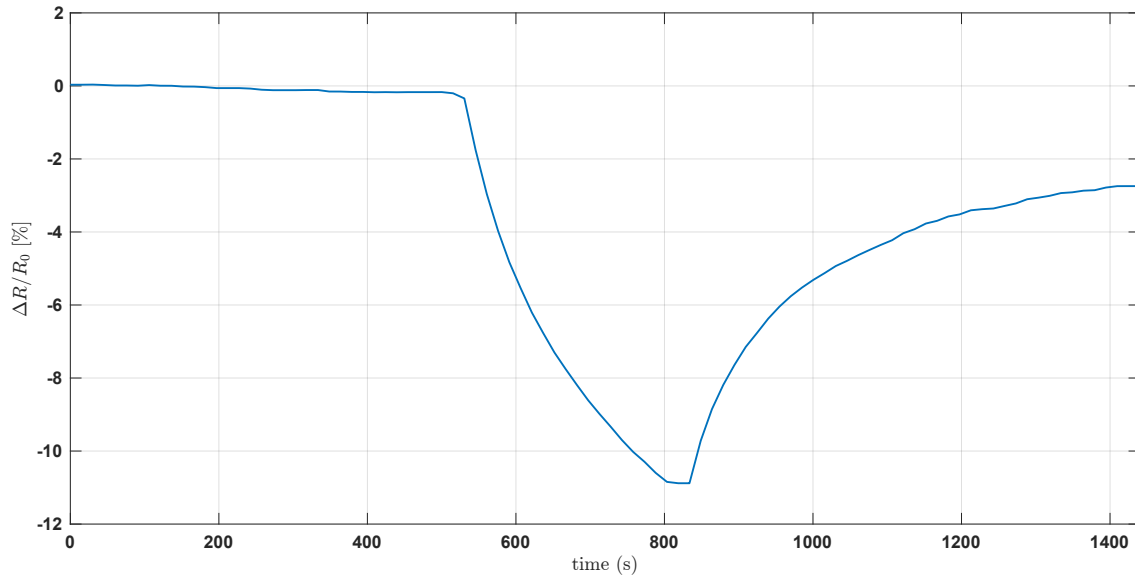


Figure B.4: A sample response of a single GB nanofiber to GB. The GB nanofiber was exposed to 1 *ppb* of GB during 5 minutes. The peak response of the GB nanofiber was around 11% compared to baseline.

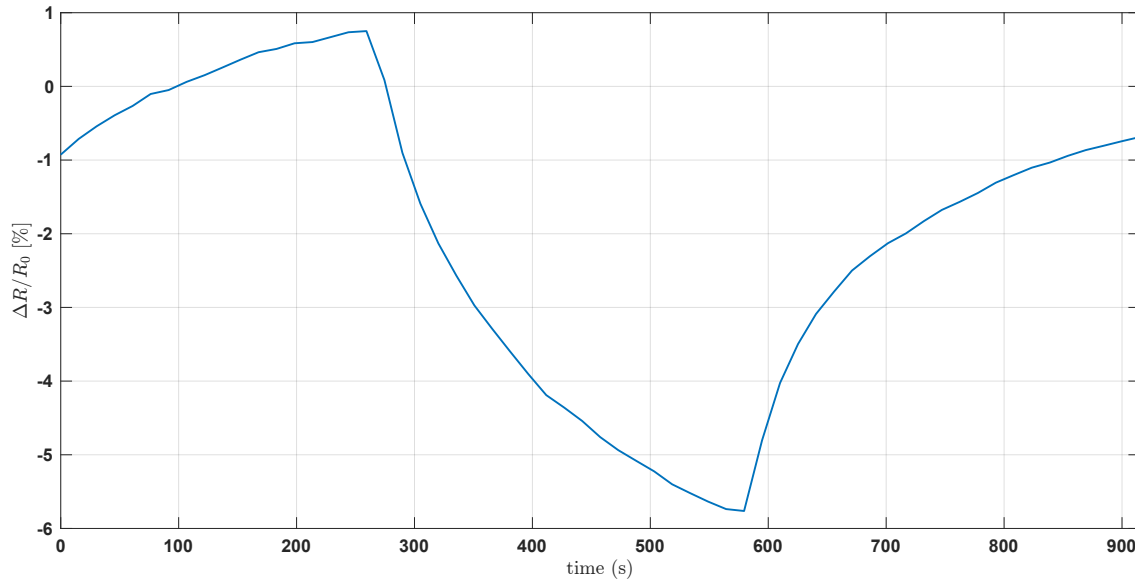


Figure B.5: A sample response of a single HD nanofiber to HD. The HD nanofiber was exposed to 1 *ppb* of HD during 5 minutes. The peak response of the HD nanofiber was around 6% compared to baseline.

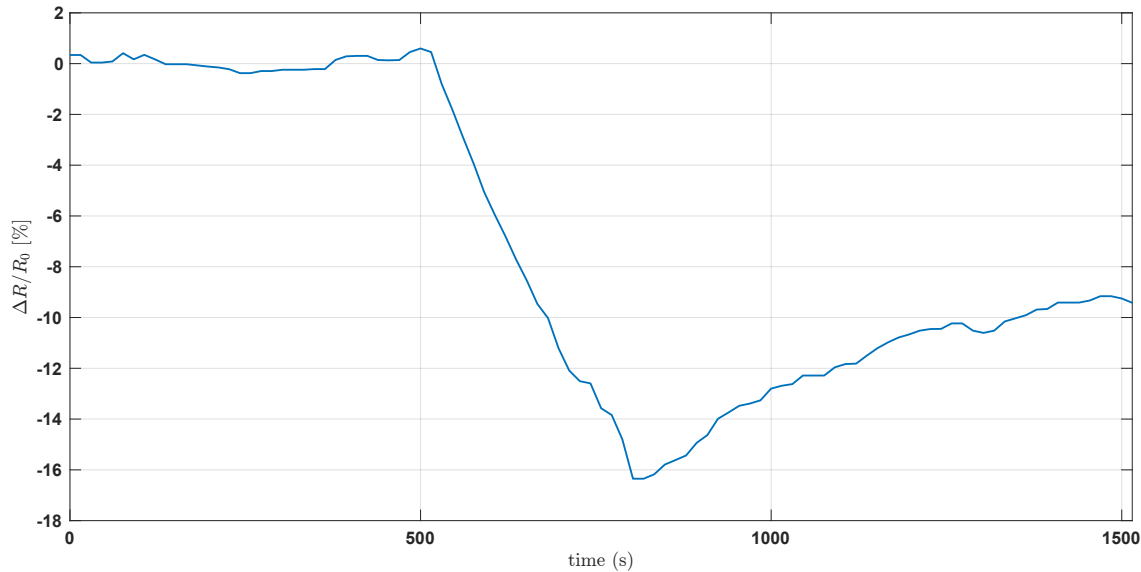


Figure B.6: A sample response of a single VX nanofiber to VX. The VX nanofiber was exposed to 1 *ppb* of VX during 5 minutes. The peak response of the VX nanofiber was around 16% compared to baseline.

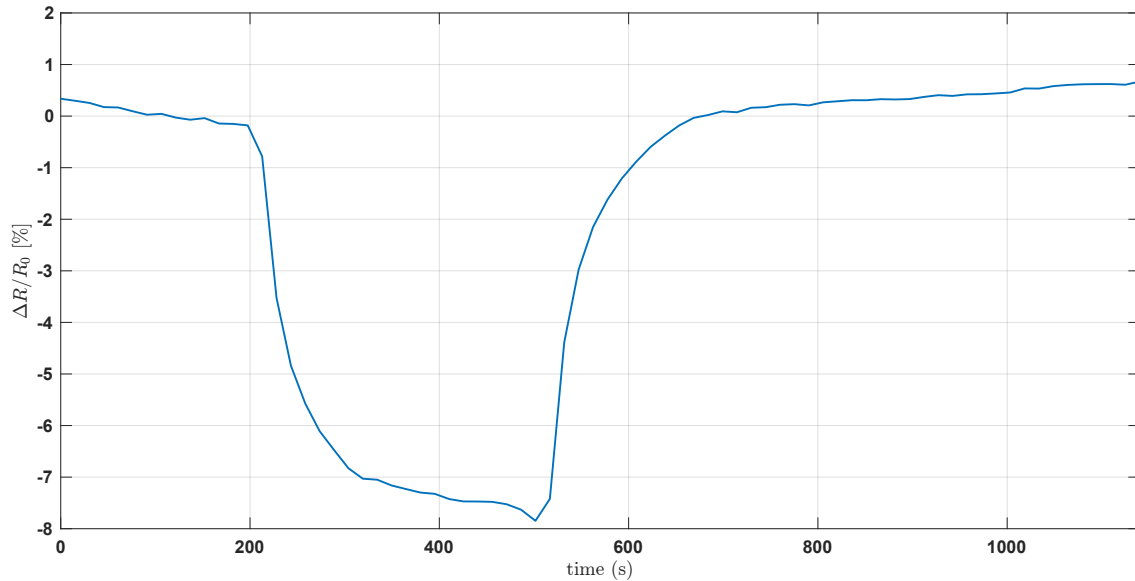


Figure B.7: A sample response of a single CG nanofiber to CG. The CG nanofiber was exposed to 1 *ppb* of CG during 5 minutes. The peak response of the CG nanofiber was around 8% compared to baseline.

REFERENCES

- [1] World Health Organization, "Health and climate change." <https://www.who.int/news-room/facts-in-pictures/detail/health-and-climate-change> (accessed Jun. 9, 2023).
- [2] World Health Organization, "Air quality and health." <https://www.who.int/teams/environment-climate-change-and-health/air-quality-and-health/health-impacts/types-of-pollutants> (accessed Jun. 9, 2023).
- [3] A. Markandya *et al.*, "Health co-benefits from air pollution and mitigation costs of the Paris Agreement: A modelling study," *Lancet Planet. Health*, vol. 2, no. 3, pp. e126–e133, Mar. 2018.
- [4] World Health Organization, "COP26 special report on climate change and health: The health argument for climate action," Meeting Rep., World Health Organization, Geneva, Switzerland, 2021. [Online]. Available: <https://iris.who.int/bitstream/handle/10665/346168/9789240036727-eng.pdf?sequence=1>.
- [5] World Health Organization, "2021 WHO health and climate change global survey report," Tech. Rep., World Health Organization, Geneva, Switzerland, 2021. [Online]. Available: <https://iris.who.int/bitstream/handle/10665/348068/9789240038509-eng.pdf?sequence=1>.
- [6] World Health Organization, "Ambient (outdoor) air pollution." [https://www.who.int/news-room/fact-sheets/detail/ambient-\(outdoor\)-air-quality-and-health](https://www.who.int/news-room/fact-sheets/detail/ambient-(outdoor)-air-quality-and-health) (accessed Jun. 12, 2023).
- [7] P. Wiederkehr and S.-J. Yoon, "Air quality indicators," in *Urban Air Pollution — European Aspects*, J. Fenger, O. Hertel, and F. Palmgren, Eds., Dordrecht, Netherlands: Springer, 1998, pp. 403–418.
- [8] K. Cromar and N. Lazrak, "Risk communication of ambient air pollution in the WHO European Region: Review of air quality indexes and lessons learned," Tech. Rep. 2023-6885-46651-67825, World Health Organization, Geneva, Switzerland, 2023. [Online]. Available: <https://iris.who.int/bitstream/handle/10665/365787/WHO-EURO-2023-6885-46651-67825-eng.pdf?sequence=1>.
- [9] G. Di Virgilio, M. A. Hart, A. M. Maharaj, and N. Jiang, "Air quality impacts of the 2019–2020 Black Summer wildfires on Australian schools," *Atmos. Environ.*, vol. 261, Art. no. 118450, Sep. 2021.
- [10] J. Rovira, J. L. Domingo, and M. Schuhmacher, "Air quality, health impacts and burden of disease due to air pollution (PM_{10} , $PM_{2.5}$, NO_2 and O_3): Application of AirQ+ model to the Camp de Tarragona County (Catalonia, Spain)," *Sci. Tot. Environ.*, vol. 703, Art. no. 135538, Feb. 2020.

- [11] Z. Yang and J. Wang, "A new air quality monitoring and early warning system: Air quality assessment and air pollutant concentration prediction," *Environ. Res.*, vol. 158, pp. 105–117, Oct. 2017.
- [12] F. Karagulian *et al.*, "Review of the performance of low-cost sensors for air quality monitoring," *Atmosphere*, vol. 10, no. 9, Art. no. 506, Aug. 2019.
- [13] E. G. Snyder *et al.*, "The changing paradigm of air pollution monitoring," *Environ. Sci. Technol.*, vol. 47, no. 20, pp. 11369–11377, Aug. 2013.
- [14] A. Abelsohn and D. M. Stieb, "Health effects of outdoor air pollution," *Can. Fam. Physician*, vol. 57, no. 8, pp. 881–887, Aug. 2011.
- [15] H. Nazemi, A. Joseph, J. Park, and A. Emadi, "Advanced micro- and nano-gas sensor technology: A review," *Sensors*, vol. 19, no. 6, Art. no. 1285, Mar. 2019.
- [16] H. Lux *et al.*, "Outdoor air pollution from industrial chemicals causing new onset of asthma or COPD: A systematic review protocol," *J. Occup. Med. Toxicol.*, vol. 15, Art. no. 38, Dec. 2020.
- [17] T. Veber, U. Dahal, K. Lang, K. Orru, and H. Orru, "Industrial air pollution leads to adverse birth outcomes: A systematized review of different exposure metrics and health effects in newborns," *Public Health Rev.*, vol. 43, Art. no. 1604775, Aug. 2022.
- [18] Z. Huang, Q. Yu, W. Ma, and L. Chen, "Surveillance efficiency evaluation of air quality monitoring networks for air pollution episodes in industrial parks: Pollution detection and source identification," *Atmos. Environ.*, vol. 215, Art. no. 116874, Oct. 2019.
- [19] L. Tang, M. Jia, J. Yang, L. Li, X. Bo, and Z. Mi, "Chinese industrial air pollution emissions based on the continuous emission monitoring systems network," *Sci. Data*, vol. 10, no. 1, Art. no. 153, Mar. 2023.
- [20] O. A. M. Popoola *et al.*, "Use of networks of low cost air quality sensors to quantify air quality in urban settings," *Atmos. Environ.*, vol. 194, pp. 58–70, Dec. 2018.
- [21] P. Asghari, A. M. Rahmani, and H. H. S. Javadi, "Internet of Things applications: A systematic review," *Comput. Netw.*, vol. 148, pp. 241–261, Jan. 2019.
- [22] J.-H. Liu *et al.*, "Developed urban air quality monitoring system based on wireless sensor networks," in *2011 5th Int. Conf. Sens. Technol.*, Nov. 28–Dec. 1, 2011, pp. 549–554.
- [23] S. A. Montzka, E. J. Dlugokencky, and J. H. Butler, "Non-CO₂ greenhouse gases and climate change," *Nature*, vol. 476, no. 7358, pp. 43–50, Aug. 2011.
- [24] S. Manabe, "Role of greenhouse gas in climate change," *Tellus A Dyn. Meteorol. Oceanogr.*, vol. 71, no. 1, Art. no. 1620078, Jun. 2019.
- [25] World Health Organization, "Climate change and health: Fact sheet on Sustainable Development Goals (SDGs): Health targets," Tech. Doc., World Health Organization, Geneva, Switzerland, 2018. [Online]. Available: <https://iris.who.int/bitstream/handle/10665/340820/WHO-EURO-2018-2374-42129-58024-eng.pdf?sequence=1>.

- [26] World Health Organization, "Climate change: An opportunity for public health." <https://www.who.int/news-room/commentaries/detail/climate-change-an-opportunity-for-public-health> (accessed Jun. 9, 2023).
- [27] LondonAir. <https://www.londonair.org.uk/LondonAir/Default.aspx> (accessed Jun. 9, 2023).
- [28] United States Environmental Protection Agency, "Interactive map of air quality monitors." <https://www.epa.gov/outdoor-air-quality-data/interactive-map-air-quality-monitors> (accessed Jun. 9, 2023).
- [29] P. Brimblecombe, *Air Composition and Chemistry*. Cambridge, UK: Cambridge University Press, 1986.
- [30] Centers for Disease Control and Prevention, "Air pollutants." <https://www.cdc.gov/air/pollutants.htm> (accessed Jun. 9, 2023).
- [31] LondonAir, "Air pollution now." <https://www.londonair.org.uk/LondonAir/nowcast.aspx> (accessed Jun. 9, 2023).
- [32] K. P. Messier *et al.*, "Indoor versus outdoor air quality during wildfires," *Env. Sci. Technol. Lett.*, vol. 6, no. 12, pp. 696–701, Dec. 2019.
- [33] W. H. Organization, *WHO Global Air Quality Guidelines: Particulate Matter (PM_{2.5} and PM₁₀), Ozone, Nitrogen Dioxide, Sulfur Dioxide and Carbon Monoxide*. Geneva, Switzerland: World Health Organization, 2021.
- [34] F. Röck, N. Barsan, and U. Weimar, "Electronic nose: Current status and future trends," *Chem. Rev.*, vol. 108, no. 2, pp. 705–725, Jan. 2008.
- [35] Tellus AirView, "Deployment map of AirU ESN." <https://airview.tellusensors.com> (accessed Jun. 12, 2023).
- [36] A. Clements, R. Duvall, D. Greene, and T. Dye, *The Enhanced Air Sensor Guidebook*. Washington, DC, USA: U.S. Environmental Protection Agency, 2022.
- [37] United States Environmental Protection Agency, "NAAQS table." <https://www.epa.gov/criteria-air-pollutants/naaqs-table> (accessed Jul. 17, 2023).
- [38] National Archives eCFR, "National primary and secondary ambient air quality standards." <https://www.ecfr.gov/current/title-40/chapter-I/subchapter-C/part-50?toc=1> (accessed Jul. 17, 2023).
- [39] C. A. Noble, R. W. Vanderpool, T. M. Peters, F. F. McElroy, D. B. Gemmill, and R. W. Wiener, "Federal reference and equivalent methods for measuring fine particulate matter," *Aerosol Sci. Tech.*, vol. 34, no. 5, pp. 457–464, Nov. 2001.
- [40] B. Paas, T. Schmidt, S. Markova, I. Maras, M. Ziefle, and C. Schneider, "Small-scale variability of particulate matter and perception of air quality in an inner-city recreational area in Aachen, Germany," *Meteorol. Z.*, vol. 25, no. 3, pp. 305–317, Jun. 2016.
- [41] D. Hertwig *et al.*, "Variability of physical meteorology in urban areas at different scales: Implications for air quality," *Faraday Discuss.*, vol. 226, pp. 149–172, Aug. 2021.

- [42] N. Zimmerman *et al.*, "A machine learning calibration model using random forests to improve sensor performance for lower-cost air quality monitoring," *Atmos. Meas. Tech.*, vol. 11, no. 1, pp. 291–313, Jan. 2018.
- [43] C. Malings *et al.*, "Development of a general calibration model and long-term performance evaluation of low-cost sensors for air pollutant gas monitoring," *Atmos. Meas. Tech.*, vol. 12, no. 2, pp. 903–920, Feb. 2019.
- [44] R. Tanzer, C. Malings, A. Hauryliuk, R. Subramanian, and A. A. Presto, "Demonstration of a low-cost multi-pollutant network to quantify intra-urban spatial variations in air pollutant source impacts and to evaluate environmental justice," *Int. J. Environ. Res. Public Health*, vol. 16, no. 14, Art. no. 2523, Jul. 2019.
- [45] A. A. Shusterman, V. E. Teige, A. J. Turner, C. Newman, J. Kim, and R. C. Cohen, "The BErkeley Atmospheric CO₂ Observation Network: Initial evaluation," *Atmos. Chem. Phys.*, vol. 16, no. 21, pp. 13449–13463, Oct. 2016.
- [46] Berkeley Environmental Air-Quality & CO₂ Network, "BEACO₂N overview." <http://beacon.berkeley.edu/overview/> (accessed Jul. 20, 2023).
- [47] C. Catlett, P. H. Beckman, R. Sankaran, and K. K. Galvin, "Array of things: A scientific research instrument in the public way: Platform design and early lessons learned," in *Proc. 2nd Int. Workshop Sci. Smart City Oper. Platforms Eng.*, pp. 26–33, Apr. 18–21, 2017.
- [48] P. Beckman, R. Sankaran, C. Catlett, N. Ferrier, R. Jacob, and M. Papka, "Waggle: An open sensor platform for edge computing," in *IEEE SENSORS*, Oct. 30–Nov. 3, 2016, pp. 1–3.
- [49] L.-J. Chen *et al.*, "An open framework for participatory PM2.5 monitoring in smart cities," *IEEE Access*, vol. 5, pp. 14441–14454, Jul. 2017.
- [50] M. I. G. Daeppe *et al.*, "Eclipse: An end-to-end platform for low-cost, hyperlocal environmental sensing in cities," in *21st ACM/IEEE Int. Conf. Inf. Process. Sensor Netw.*, May 4–6, 2022, pp. 28–40.
- [51] X. Liu, S. Cheng, H. Liu, S. Hu, D. Zhang, and H. Ning, "A survey on gas sensing technology," *Sensors*, vol. 12, no. 7, pp. 9635–9665, Jul. 2012.
- [52] N. Yamazoe and K. Shimanoe, "New perspectives of gas sensor technology," *Sensors Actuators B Chem.*, vol. 138, no. 1, pp. 100–107, Apr. 2009.
- [53] Y. Cheng *et al.*, "AirCloud: A cloud-based air-quality monitoring system for everyone," in *Proc. 12th ACM Conf. Embed. Netw. Sensor Syst.*, Nov. 3–6, 2014, pp. 251–265.
- [54] K. K. Khedo, R. Perseedoss, and A. Mungur, "A wireless sensor network air pollution monitoring system," *Int. J. Wirel. Mob. Netw.*, vol. 2, no. 2, pp. 31–45, May 2010.
- [55] B. Szulczyński and J. Gębicki, "Currently commercially available chemical sensors employed for detection of volatile organic compounds in outdoor and indoor air," *Environments*, vol. 4, no. 1, Art. no. 21, Mar. 2017.

- [56] F. Temel and M. Tabakci, "Calix[4]arene coated QCM sensors for detection of VOC emissions: Methylene chloride sensing studies," *Talanta*, vol. 153, pp. 221–227, Jun. 2016.
- [57] A. Mujahid and F. L. Dickert, "Surface acoustic wave (SAW) for chemical sensing applications of recognition layers," *Sensors*, vol. 17, no. 12, 2716, Nov. 2017.
- [58] K. K. Park *et al.*, "Capacitive micromachined ultrasonic transducer (CMUT) as a chemical sensor for DMMP detection," *Sensors Actuators B Chem.*, vol. 160, no. 1, pp. 1120–1127, Dec. 2011.
- [59] M. Kumar, C. Seok, M. M. Mahmud, X. Zhang, and O. Oralkan, "A low-power integrated circuit for interfacing a capacitive micromachined ultrasonic transducer (CMUT) based resonant gas sensor," in *IEEE SENSORS*, Nov. 1–4, 2015, pp. 1–4.
- [60] M. R. R. Khan and S.-W. Kang, "A high sensitivity and wide dynamic range fiber-optic sensor for low-concentration VOC gas detection," *Sensors*, vol. 14, no. 12, pp. 23321–23336, Dec. 2014.
- [61] Y.-n. Zhang, Z. Yong, and L. Ri-qing, "A review for optical sensors based on photonic crystal cavities," *Sensors Actuators A Phys.*, vol. 233, pp. 374–389, Sep. 2015.
- [62] M. Donarelli and L. Ottaviano, "2D materials for gas sensing applications: A review on graphene oxide, MoS₂, WS₂ and phosphorene," *Sensors*, vol. 18, no. 11, Art. no. 3638, Nov. 2018.
- [63] C. Wang, L. Yin, L. Zhang, D. Xiang, and R. Gao, "Metal oxide gas sensors: Sensitivity and influencing factors," *Sensors*, vol. 10, no. 3, pp. 2088–2106, Mar. 2010.
- [64] H. Huang, D. E. Gross, X. Yang, J. S. Moore, and L. Zang, "One-step surface doping of organic nanofibers to achieve high dark conductivity and chemiresistor sensing of amines," *ACS Appl. Mater. Interfaces*, vol. 5, no. 16, pp. 7704–7708, Aug. 2013.
- [65] H. Bai and G. Shi, "Gas sensors based on conducting polymers," *Sensors*, vol. 7, no. 3, pp. 267–307, Mar. 2007.
- [66] L. Zang, Y. Che, and J. S. Moore, "One-dimensional self-assembly of planar pi-conjugated molecules: Adaptable building blocks for organic nanodevices," *Accounts of Chem. Research*, vol. 41, no. 12, pp. 1596–1608, Dec. 2008.
- [67] Y. Zhang *et al.*, "Oligomer-coated carbon nanotube chemiresistive sensors for selective detection of nitroaromatic explosives," *ACS Appl. Mater. Interfaces*, vol. 7, no. 14, pp. 7471–7475, Apr. 2015.
- [68] C. Wang *et al.*, "Interfacial donor-acceptor nanofibril composites for selective alkane vapor detection," *ACS Sensors*, vol. 1, no. 5, pp. 552–559, Mar. 2016.
- [69] Y. Zhang, B. R. Bunes, N. Wu, A. Ansari, S. Rajabali, and L. Zang, "Sensing methamphetamine with chemiresistive sensors based on polythiophene-blended single-walled carbon nanotubes," *Sensors Actuators B Chem.*, vol. 255, no. 2, pp. 1814–1818, Feb. 2018.

- [70] Gentex Corporation, "Vaporsens' nanofiber chemical library." <https://vaporsens-inc.squarespace.com/chemical-library> (accessed Jul. 4, 2023).
- [71] Y. Che, A. Datar, X. Yang, T. Naddo, J. Zhao, and L. Zang, "Enhancing one-dimensional charge transport through intermolecular π -electron delocalization: Conductivity improvement for organic nanobelts," *J. Am. Chem. Soc.*, vol. 129, no. 20, pp. 6354–6355, Apr. 2007.
- [72] Y. Huang, L. Fu, W. Zou, F. Zhang, and Z. Wei, "Ammonia sensory properties based on single-crystalline micro/nanostructures of perylenediimide derivatives: Core-substituted effect," *J. Phys. Chem. C*, vol. 115, no. 21, pp. 10399–10404, May 2011.
- [73] Y. Che, X. Yang, S. Loser, and L. Zang, "Expedient vapor probing of organic amines using fluorescent nanofibers fabricated from an n-type organic semiconductor," *Nano Lett.*, vol. 8, no. 8, pp. 2219–2223, Aug. 2008.
- [74] U. Yaqoob and M. I. Younis, "Chemical gas sensors: Recent developments, challenges, and the potential of machine learning—A review," *Sensors*, vol. 21, no. 8, Art. no. 2877, Apr. 2021.
- [75] Gentex Corporation, "Nanofiber sensor technology." <https://vaporsens-inc.squarespace.com/nanofiber-sensor-technology> (accessed Jul. 6, 2023).
- [76] Keysight Technologies, *Reliable High-Resistance Measurements Using the B2985A/87A*, 2014. [Online]. Available: <https://www.keysight.com/us/en/assets/7018-04500/application-notes/5991-4951.pdf>.
- [77] T. Becnel *et al.*, "A distributed low-cost pollution monitoring platform," *IEEE Internet Things J.*, vol. 6, no. 6, pp. 10738–10748, Sep. 2019.
- [78] A. Flammini, D. Marioli, and A. Taroni, "A low-cost interface to high-value resistive sensors varying over a wide range," *IEEE Trans. Instrum. Meas.*, vol. 53, no. 4, pp. 1052–1056, Aug. 2004.
- [79] A. Depari *et al.*, "A new low-cost electronic system to manage resistive sensors for gas detection," *IEEE Sensors J.*, vol. 7, no. 7, pp. 1073–1077, Jul. 2007.
- [80] M. Grassi, P. Malcovati, and A. Baschirotto, "A 141-dB dynamic range CMOS gas-sensor interface circuit without calibration with 16-bit digital output word," *IEEE J. Solid State Circuits*, vol. 42, no. 7, pp. 1543–1554, Jul. 2007.
- [81] M. Grassi, P. Malcovati, and A. Baschirotto, "Wide-range integrated gas sensor interface based on a resistance-to-number converter technique with the oscillator decoupled from the input device," in *2006 IEEE Int. Symp. Circuits Syst.*, May 21–24, 2006, pp. 4398–5001.
- [82] M. Chen, S. Peng, N. Wang, L. Xu, F. Lin, and F. Wu, "A wide-range and high-resolution detection circuit for MEMS gas sensor," *IEEE Sensors J.*, vol. 19, no. 8, pp. 3130–3137, Apr. 2019.
- [83] G. Ferri *et al.*, "A single-chip integrated interfacing circuit for wide-range resistive gas sensor arrays," *Sensors Actuators B Chem.*, vol. 143, no. 1, pp. 218–225, Dec. 2009.

- [84] Mouser Electronics, “FPGA – Field Programmable Gate Array.” <https://www.mouser.com/c/semiconductors/programmable-logic-ics/fpga-field-programmable-gate-array/?q=fpgaactive=ynormallystocked=ysort=pricing> (accessed Jun. 22, 2023).
- [85] A. De Marcellis, G. Ferri, A. Depari, and A. Flammini, “A novel time-controlled interface circuit for resistive sensors,” in *IEEE SENSORS*, Oct. 28–31, 2011, pp. 1137–1140.
- [86] A. Depari, A. Flammini, E. Sisinni, A. De Marcellis, G. Ferri, and P. Mantenuto, “Fast, versatile, and low-cost interface circuit for electrochemical and resistive gas sensor,” *IEEE Sensors J.*, vol. 14, no. 2, pp. 315–323, Feb. 2014.
- [87] E. K. and A. C. Sreekantan, “Evaluation of new digital signal conditioning techniques for resistive sensors in some practically relevant scenarios,” *IEEE Trans. Instrum. and Meas.*, vol. 70, pp. 1–9, May 2021.
- [88] E. K., V. B. Sukumaran, and A. C. Sreekantan, “Geometric programming assisted conversion time reduction technique applied to a multiregime-based digitizer for wide span resistive sensors,” *IEEE Trans. Instrum. Meas.*, vol. 72, pp. 1–4, Feb. 2023.
- [89] G. Gonzalez, *Foundations of Oscillator Circuit Design*. Boston, MA, USA: Artech House Microwave Library, 2006.
- [90] A. A. Abidi and R. G. Meyer, “Noise in relaxation oscillators,” *IEEE J. Solid State Circuits*, vol. 18, no. 6, pp. 794–802, Dec. 1983.
- [91] R. Hogervorst, J. P. Tero, R. G. H. Eschauzier, and J. H. Huijsing, “A compact power-efficient 3 V CMOS rail-to-rail input/output operational amplifier for VLSI cell libraries,” *IEEE J. Solid State Circuits*, vol. 29, no. 12, pp. 1505–1513, Dec. 1994.
- [92] T. Sepke, P. Holloway, C. G. Sodini, and H.-S. Lee, “Noise analysis for comparator-based circuits,” *IEEE Trans. Circuits Syst.*, vol. 56, no. 3, pp. 541–553, Mar. 2009.
- [93] W. Tian, P. Steinmann, E. Beach, I. Khan, and P. Madhani, “Mismatch characterization of a high precision resistor array test structure,” in *2008 IEEE Int. Conf. Microelectr. Test Struct.*, Mar. 24–27, 2008, pp. 11–16.
- [94] A. Hastings, *The Art of Analog Layout*. Hoboken, NJ, USA: Prentice Hall, 2001.
- [95] A. Depari *et al.*, “A new CMOS integrable oscillating circuit for high-value wide-range resistive sensors,” in *2007 IEEE Instrum. Meas. Technol. Conf.*, May 1–3, 2007, pp. 1–4.
- [96] A. Depari, A. Flammini, D. Marioli, and E. Sisinni, “A fast-readout interface circuit for high-value and wide-range resistive chemical sensors,” in *2010 IEEE Instrum. Meas. Technol. Conf. Proc.*, May 3–6, 2010, pp. 116–120.
- [97] F. Conso, M. Grassi, P. Malcovati, and A. Baschirotto, “Reconfigurable integrated wide-dynamic-range read-out circuit for mox gas-sensor grids providing local temperature regulation,” in *IEEE SENSORS*, Oct. 28–31, 2012, pp. 1–4.

- [98] J. W. Gardner, P. K. Guha, F. Udrea, and J. A. Covington, "CMOS interfacing for integrated gas sensors: A review," *IEEE Sensors J.*, vol. 10, no. 12, pp. 1833–1848, Jun. 2010.
- [99] N. H. Motlagh *et al.*, "Toward massive scale air quality monitoring," *IEEE Commun. Mag.*, vol. 58, no. 2, pp. 54–59, Feb. 2020.
- [100] T. Becnel and P.-E. Gaillardon, "A deep learning approach to sensor fusion inference at the edge," in *2021 Des. Autom. Test Eur. Conf. Exhib.*, Feb. 1–5, 2021, pp. 1420–1425.
- [101] K. E. Kelly *et al.*, "Community-based measurements reveal unseen differences during air pollution episodes," *Env. Sci. Technol.*, vol. 55, no. 1, pp. 120–128, Jan. 2021.
- [102] D. Smith, K. Sovová, K. Dryahina, T. Doušová, P. Dřevínek, and P. Španěl, "Breath concentration of acetic acid vapour is elevated in patients with cystic fibrosis," *J. Breath Res.*, vol. 10, no. 2, Art. no. 021002, May 2016.
- [103] M. M. Macías, A. G. Manso, C. J. G. Orellana, H. M. G. Velasco, R. G. Caballero, and J. C. P. Chamizo, "Acetic acid detection threshold in synthetic wine samples of a portable electronic nose," *Sensors*, vol. 13, no. 1, pp. 208–220, Dec. 2013.
- [104] S. Das and M. Pal, "Review—Non-invasive monitoring of human health by exhaled breath analysis: A comprehensive review," *J. Electrochem. Soc.*, vol. 167, no. 3, Art. no. 037562, Feb. 2020.